INTRA-SEGMENT VARIATIONS IN SUBDUCTION INFLUENCE ALONG THE EASTERN LAU SPREADING CENTER AND VALU FA RIDGE, LAU BACKARC BASIN, SW PACIFIC

A THESIS SUBMITTED TO THE GRADUATE DIVISION OF THE UNIVERSITY OF HAWAIʻI AT MĀNOA IN PARTIAL FULFILLMENT OF THE REQUIREMENTS FOR THE DEGREE OF

MASTER OF SCIENCE

IN

MARINE GEOPHYSICS

MAY 2011

By

Jonathan D. Sleeper

Thesis Committee:

Fernando Martinez, Chairperson

Greg Moore

Margo Edwards

Keywords: *Lau basin, backarc, spreading center, subduction zone*

ABSTRACT

This manuscript presents results of geologic mapping along the Eastern Lau Spreading Center and Valu Fa Ridge, Lau backarc basin, southwest Pacific. The study documents geologic variations within six second-order spreading segments, expressed primarily in the morphology and depth of the spreading axis that depart from normal mid-ocean ridge (MOR) trends and are superimposed on the first order variations correlated with proximity to the arc volcanic front. These along-axis variations show a positive correlation with $^{206}Pb/^{204}Pb$ ratios from axial lavas, a commonly used indicator of relative subduction input. This suggests that local variations in subduction influence, mostly due to effects on magmatism, may be expressed as local variations in the geologic characteristics of the ridge. The nature and distribution of these variations, along with the observation of similar patterns in other backarc environments, suggests that the processes which control backarc spreading share a deep connection with arc processes.

TABLE OF CONTENTS

LIST OF FIGURES

1. Introduction

The term “backarc basin” is used to denote extensional basins associated with subduction zones where relative convergence occurs between tectonic plates. Daniel Karig, in 1970, was the first to recognize these structures behind subduction zones in the western Pacific and suggest that they had a common extensional origin [*Karig,* 1970]. Extension in these settings may be caused by the subducting slab sinking faster than the convergence rate leading to “roll-back” of the trench or by the upper plate moving away from the trench, or both of these mechanisms. The extensional forces create basins which typically initiate by rifting within ~50 km of the arc volcanic front [*Martinez and Taylor, 2006*]. If extension continues, the basins develop seafloor spreading systems and a new volcanic arc forms in front (trenchward) of the basins. Thus backarc basins are typically located behind the active volcanic arcs characteristic of subduction. The subducting plate or “slab” recycles lithospheric material back into the mantle, introducing water, sediments, altered crust, and slab lithosphere into the mantle wedge, the triangular region of mantle located between the slab and the overriding plate. The materials introduced into the mantle wedge by subduction are a primary source of chemical heterogeneity in the Earth’s upper mantle. Because backarc basins are formed by extension they develop seafloor spreading centers like those at mid-ocean ridges (MOR’s), although backarc spreading centers display quite different characteristics. The chemical heterogeneities introduced into the mantle wedge by the subducting slab are the primary control on the geologic and geophysical characteristics of backarc spreading centers, unlike MOR’s where first-order characteristics are primarily governed by spreading rate [*Macdonald, 1982*]. The slab-derived component that most significantly affects the melting characteristics and rheology of the mantle is water. As the slab descends into the mantle, sediment compaction and the breakdown of hydrous minerals release water continuously beginning at the trench to depths of 150-200 km [*Schmidt and Poli, 1998*]. Water lowers the mantle solidus temperature and increases melt productivity in backarc spreading centers in proportion to water content [*Stolper and Newman, 1994*]. It also

strongly influences mantle rheology by decreasing the viscosity of olivine aggregates by orders of magnitude relative to anhydrous olivine [*Karato et al., 1986, Hirth and Kohlstedt,* 2003]. The subducting slab also acts as a physical barrier in the mantle, altering mantle convection and inducing corner flow in the mantle wedge which may re-circulate depleted mantle material to backarc spreading centers and actually suppress melt generation along portions of the spreading system [*Garfunkel et al., 1986, Martinez and Taylor,* 2002]. These effects, particularly the addition of water to the mantle, are thought to be important controls on the geologic and geophysical characteristics of backarc spreading centers, especially along those situated in close proximity to the arc volcanic front where subduction effects are strongest.

Studies in the Lau basin and other backarc basins around the world have documented the first-order along-axis variations in axial morphology, crustal thickness, melt production, faulting, and other characteristics, which correlate with proximity to the arc volcanic front. In general, as the axis approaches the arc the system becomes much more magmatically robust, ridge relief becomes higher, axial depth becomes shallower, the lavas become more porous and more andesitic in composition, faulting and hydrothermal activity decrease, and crustal thickness increases [*Jenner et al., 1987, Vallier et al., 1991, Pearce et al., 1994, Taylor and Martinez, 2003, Baker et al., 2006, Martinez et al., 2006*]. However, while the overall trends and large-scale changes have been generally well documented, local variations at the intra-segment scale and the processes which control them are still poorly understood, especially in the context of a well-developed backarc spreading system. The main finding of this study is that variations in morphology and volcanism at the intra-segment scale show a correlation with local variations in subduction influence along the axis, as indicated by geochemical and geophysical data [*Jenner et al., 1987, Vallier et al., 1991, Loock et al., 1992, Harding et al., 2000, Peate et al., 2001, Jacobs et al., 2007, Dunn et al., 2009, Escrig et al., 2009, Dunn and Martinez, 2011*]. This correlation suggests that small-scale variations in subduction influence exert at least some control on the small-scale geologic variations of the spreading

system, in a similar manner to how the large-scale systematic variation in subduction influence controls the large-scale geologic variations along the entire axis. Other geologic characteristics such as faulting and hydrothermal activity appear to be largely insensitive to variations in subduction input at the intra-segment scale, instead following the first-order trends associated with arc proximity [*Baker et al., 2006, Martinez et al., 2006, Baker et al., 2010*]. Understanding how local variations in subduction influence within the mantle wedge are expressed on the seafloor provides important insights into how these processes are connected, and sheds some light on the mechanisms which control the spatial and temporal distribution of slab-derived components in the mantle wedge. These variations also provide insights into controls on backarc segmentation and how mantle chemical heterogeneities affect seafloor spreading in general, even outside of the backarc setting.

The Lau backarc basin, located in the southwest Pacific and associated with the Tonga subduction zone, is a favorable location to study the various scales of subduction effects on seafloor spreading systems (*Fig. 1*). The basin began opening from north to south approximately 6 Ma [*Zellmer and Taylor, 2001*]. This opening geometry created a triangular basin that narrows toward the south. Thus, the spreading systems in the central and southern basin progressively approach the active Tofua volcanic arc from north to south. This geometry is relatively uncommon amongst backarc basins, which often have an arcuate shape where the spreading system approaches the arc towards the ends, but does not necessarily get far enough from the arc to be completely free of its influence along the central portion. The spreading centers of the central and southern Lau basin encompass a wide spectrum of morphologies from a peaked, inflated ridge with abundant magma supply along Valu Fa Ridge (VFR) in the south, ~40 km from the arc, to a flat axis with reduced magmatism and abundant faulting along the Northern Eastern Lau Spreading Center (NELSC), ~80-100 km from the arc, and finally to the MOR-like Central Lau Spreading Center (CLSC), ~175-200 km from the arc in the north-central portion of the basin, where arc influence is negligible [*Martinez et al., 2006*]. Also, crustal

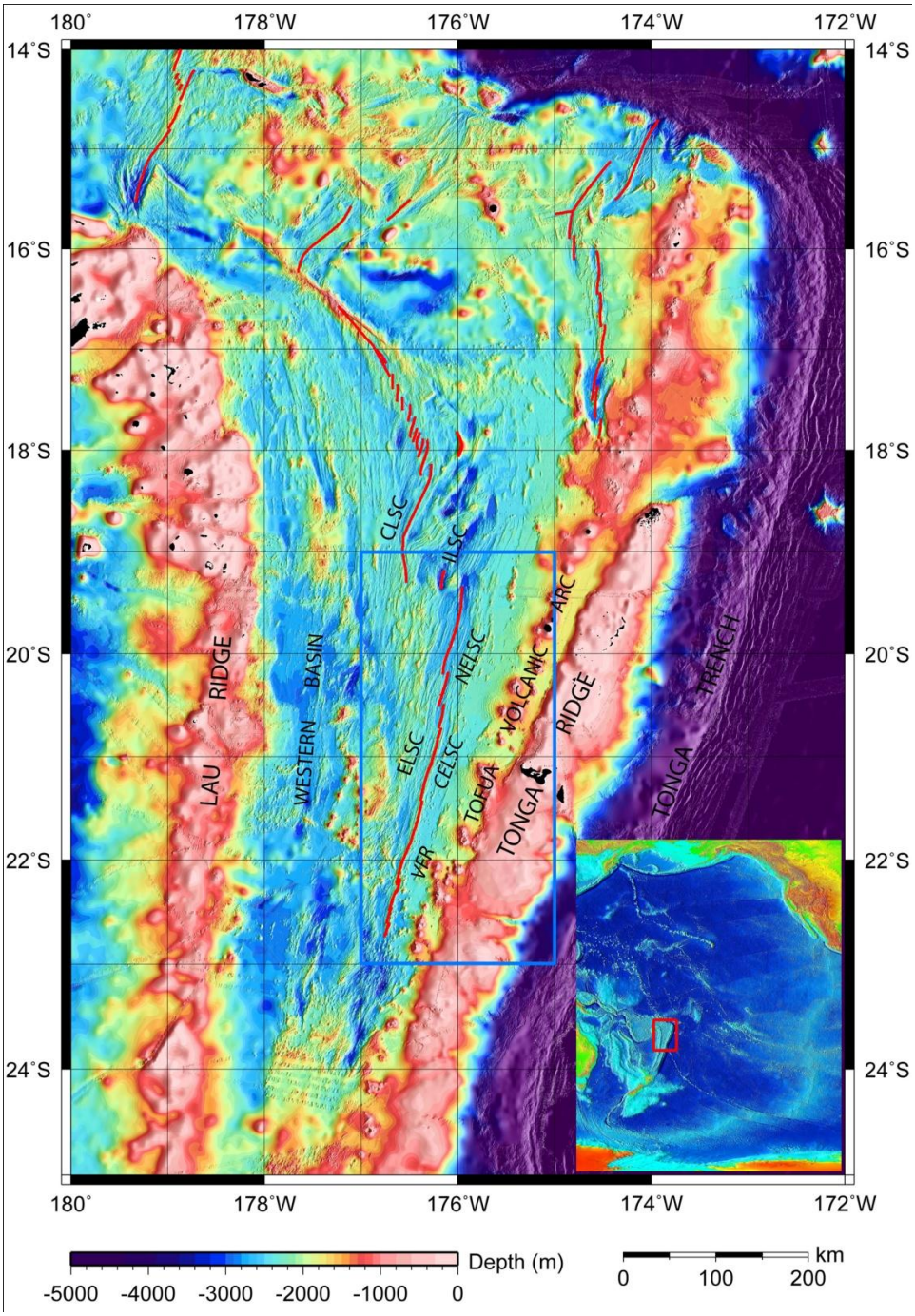

Figure 1: Compiled bathymetry map (100 m cell size) of the entire Lau basin. Gaps in multibeam coverage are filled with predicted bathymetry from satellite altimetry [*Smith and Sandwell, 1997*]. Inset shows Lau basin in a red box in the southwest Pacific. Identified spreading segments relevant to this study are marked with solid red lines and labeled as follows: CLSC = Central Lau Spreading Center, ILSC = Intermediate Lau Spreading Center, ELSC = Eastern Lau Spreading Center, NELSC = Northern ELSC, CELSC = Central ELSC, VFR = Valu Fa Ridge. The blue box outlines the focus region of the study and the limits of *Fig. 2*.

thickness increases toward the south from ~5.5 km to ~9 km [*Martinez et al., 2006*] as the lavas become more porous and more andesitic in composition and overall magmatism increases [*Jenner et al., 1987, Vallier et al, 1991, Pearce et al., 1994*]. These large-scale systematic changes can be attributed to the increasing influence of water and other subduction-related processes southward as the spreading axis approaches the arc [*Martinez et al., 2006*]. Similar trends are seen along other backarc ridges (BAR's) that approach within ~150 km of the arc volcanic front, including the Mariana, East Scotia, and Manus Basins [*Martinez and Taylor, 2003*]. Within ~80 km of the arc, where subduction influence and hydrous flux is strongest, magmatism and crustal thickness increase, creating magmatically robust, inflated spreading axes [*Martinez et al., 2006*]. In the intermediate zone between ~80-150 km from the arc, subduction effects act to create an anomalous reduction in magmatism and crustal thickness relative to MOR's with similar spreading rates, and the lavas erupted along the axis become denser, less porous, and more basaltic in composition [*Martinez et al., 2006*]. It appears that this zone of reduced magmatism is related to recirculation of depleted mantle wedge material under the spreading axis, as well as an abrupt reduction in influx of hydrous melt from the slab [*Martinez and Taylor, 2002*]. By ~150-200 km from the arc, the influence of the slab essentially disappears and the spreading centers become similar both morphologically and geochemically to MOR's, where characteristics vary primarily with spreading rate [*Martinez et al., 2006*].

This study focuses on describing intra-segment geologic variability in the characteristics of the spreading centers of the central and southern Lau basin, including the ELSC and VFR, which is the location of the Lau Integrated Studies Site associated with the Ridge 2000 program [*Taylor et al., 2001*]. The ELSC and VFR have been traditionally divided into three main segments: VFR, Central ELSC (CELSC), and the NELSC, but for this study these three have been subdivided into six second-order segments, as defined by *Macdonald et al., 1991a,* from south to north: VFR-S, VFR-N, CELSC-S, CELSC-N, NELSC-S, and NELSC-N (*Fig. 2*). The geology of these segments is characterized through

detailed geologic mapping along six segments of the ELSC and VFR, with the mapping concentrated on the portions of the axis covered by the 2008 survey on *R/V Kilo Moana* (KM0804) [*Martinez et al., 2008*]. The study focuses on the geology of the spreading segments as revealed in sonar imagery and bathymetry from both deep-towed and hull-mounted multibeam systems, providing complimentary data with variable resolution and areal coverage. Along the VFR-S, VFR-N, and the CELSC-S segments, a consistent pattern can be observed in axial morphology, relief, and depth. Segment ends are consistently the shallowest and highest relief portions of the axis, while segment centers are consistently the deepest and lowest relief portions within each segment, similar to a cosine curve. In the center of the CELSC-N segment, the depth of the axis abruptly drops, coinciding with abrupt changes in crustal thickness, porosity, and composition [*Dunn and Martinez,* 2011]. The NELSC no longer shows a discernable intra-segment pattern like the VFR and CELSC-S. *Figures 3-5* summarize these along axis changes through bathymetry plots, sidescan images, and along-axis profiles. Based on $^{206}Pb/^{204}Pb$ ratios from axial lavas collected along the majority of the axis [*Jenner et al., 1987, Vallier et al., 1991, Loock et al., 1992, Peate et al., 2001, Escrig et al., 2009*] intra-segment variations in subduction influence show a positive correlation with the changes observed in axial morphology, relief, and depth (*Fig. 8*). The local highs in $^{206}Pb/^{204}Pb$ ratios correspond with relatively shallow, high relief portions of the axis, and local lows in $^{206}Pb/^{204}Pb$ ratios correspond with deeper, lower relief portions of the segment, suggesting that local changes in subduction influence may be controlling the observed geologic variations along the axis. Furthermore, the sudden drop in $^{206}Pb/^{204}Pb$ ratios at ~20.6^{o} S is reflected in the sudden morphologic changes that occur within the CELSC-N segment and the characteristics of the NELSC. The correlation between local variations in subduction influence and axial morphology is the primary focus of this study and its implications form the backbone of the interpretations presented herein. Other geologic characteristics, such as faulting and hydrothermal activity, are also discussed to determine how they may or may not relate to the observed intra-

segment variations and gain insight into the controls on these processes [*Martinez et al., 2008, Baker et al., 2006, Baker et al., 2010*].

2. Geologic Setting and Background

2.1 Lau basin

The Lau basin is a backarc basin formed behind the Tonga subduction zone, the locus of the fastest subduction on earth, with Pacific-Tonga Ridge convergence rates along the Tonga trench of up to 240 $\pm$11 mm/yr along the northernmost portion of the system, decreasing to 164 $\pm$5 mm/yr near the island of Tongatapu [*Bevis, 1995*]. The specific effects of these high convergence rates are not well understood, but at the very least they should increase the rate at which water and other slab-derived components are introduced into the mantle wedge, affecting its viscosity and melting characteristics to a greater degree than a subduction zone with lower convergence rates. The subducting Pacific plate, which has an average age of ~100 Ma, varies in dip from ~25-30^{o} within a ~200 km lateral distance from the trench, steepening to ~45-55^{o} under the rest of the basin, but does not vary significantly along-strike [*Harmon and Blackman, 2010*]. The basin is bounded on the west side by the Lau Ridge, a remnant arc, and on the east side by the active Tofua arc volcanic front and the Tonga Ridge, a volcanic forearc massif. Along the northern margin of the basin, the Pacific plate no longer subducts under the Australian plate, but instead moves in a west-northwest direction along a transform boundary [*Pelletier and Louat, 1989*], which is accommodated by a tear in the Pacific plate [*Millen and Hamburger, 1988*]. In the northern portion of the basin north of the CLSC, spreading is accommodated in a complex manner and is divided among numerous short spreading segments distributed across the basin [*Pelletier et al., 2001, Zellmer and Taylor, 2001*]. Along the CLSC, the spreading axis lies on the boundary between the Australian plate and the Niuafo'ou micro-plate, while along the ELSC and VFR, the spreading axis is along the Pacific and Australian plates [*Zellmer and Taylor, 2001*]. South of the VFR, spreading appears to be distributed in a diffuse

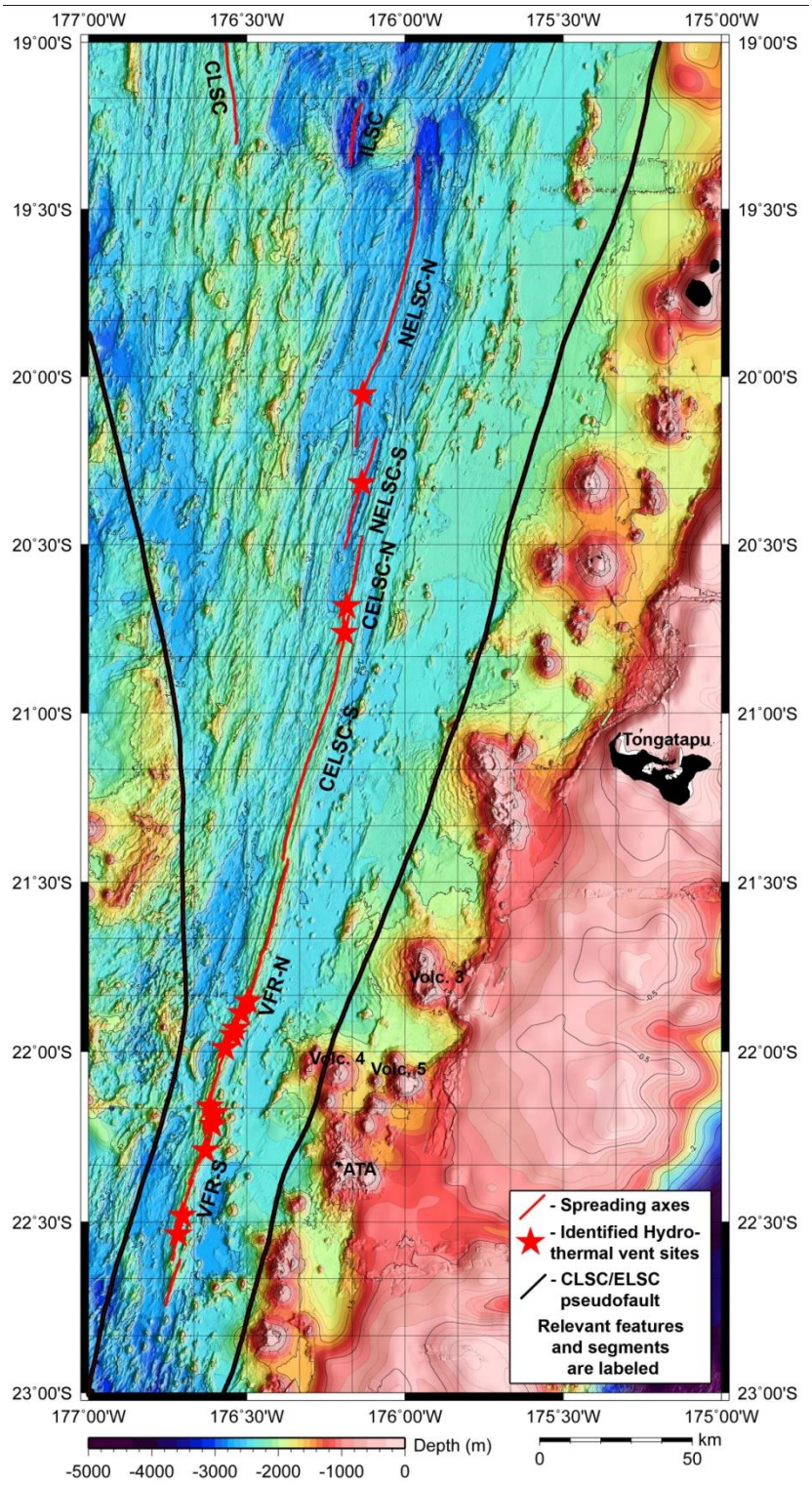

Figure 2: Compiled bathymetry map (100 m cell size) of the ELSC and VFR. Gaps in multibeam coverage are filled with predicted bathymetry from satellite altimetry data [*Smith and Sandwell, 1997*]. Identified spreading segments are marked with red lines and identified hydrothermal vent sites are marked as red stars. The six 2nd order segments that this study focuses on are labeled.

manner across a wide patch of seafloor, the basin becomes narrower, and ultimately it transitions into the Havre Trough by ~25^{o}36' S. This transition corresponds to the location of the subducting Louisville Seamount Chain (LSC), which marks the boundary between the Tofua and Kermadec arcs. Although the effects of LSC subduction are not well constrained, it is notable that it projects directly under the VFR, which may partially explain some of the anomalous characteristics seen along that portion of the axis.

The complex geologic history of the Lau basin began ~6 Ma with crustal stretching and rifting within the pre-existing forearc region, now preserved as the Tonga Ridge [*Gill, 1976*]. As basin opening progressed southward from ~6 Ma to ~4 Ma, extension was accommodated through crustal accretion along relatively short-lived spreading centers, the evidence of which is now preserved in the crust of the western basin [*Martinez and Taylor, 2006*]. The western basin crust was initially interpreted as rifted pre-existing arc crust, but analysis of seafloor magnetization anomaly patterns and the characteristics of the western basin seafloor have informed this revised model of crustal accretion along short-lived spreading segments, rather than purely arc rifting [*Martinez and Taylor, 2006, Austin et al., 2009*]. At ~4 Ma, the ELSC initiated in the northern portion of the basin and began to propagate southward in a north-south orientation until ~2 Ma, when the ELSC rotated 15-25^{o} clockwise, subdivided into left-stepping overlapping segments, and continued to propagate southward [*Taylor et al., 1996*]. At the same time, the CLSC initiated and began propagating southward to 19^{o}20' S where the present rift tip is located, replacing the ELSC as it grew [*Taylor et al., 1996*].

2.2 ELSC and VFR

The combined length of the ELSC and VFR is ~400 km, extending from ~19^{o}20' S to 22^{o}45' S in a N-NE/S-SW direction and progressively approaching the Tofua arc volcanic front from ~100 km away in the north to ~40 km away at the southern end [*Martinez et al., 2006*]. Along its length, the spreading rate also VFR at the southern end [*Zellmer and Taylor, 2001*], while the geologic and

changes from ~96 mm/yr in the north along the NELSC to ~39 mm/yr along the geophysical characteristics of the spreading axes also change drastically [*Martinez and Taylor, 2006*]. The variations in geologic characteristics, such as axial morphology, faulting, volcanic structures, lava composition, and style of volcanism range from abrupt to gradual and occur at a variety of scales within and between the segments. In the subduction-influenced backarc setting of the Lau basin, the trend in morphology appears to be independent of spreading rate and opposite that of MOR's, where fast spreading is associated with smooth axial highs and slow spreading with deep axial valleys [*Macdonald et al., 1990*]. In the Lau basin, the axial high is along the VFR, closest to the arc and spreading at the slowest rate, and the axial deep is in the north along the NELSC, where spreading rates are highest. Along the CELSC and VFR, the crust ranges from ~7.5 km to 9 km thick, while along the NELSC it decreases to ~5-6 km [*Martinez and Taylor, 2002*]. Multi-channel seismic (MCS) data shows a decrease in crustal seismic velocities and deepening of the AMC reflector toward the south, consistent with increasingly porous lava and thicker crust [*Harding et al., 2000, Jacobs et al., 2007*]. These changes in crustal thickness have been attributed to both the reduced magmatic production as the spreading center gets further from the volatile-rich arc source and a change in magma chemistry from more porous andesitic lavas along the VFR and most of the CELSC to denser depleted MORB lavas along the NELSC [*Pearce et al., 1994, Martinez and Taylor, 2002*]. This compositional change can be seen in geochemical analyses of axial lavas which generally become more andesitic toward the south [*Jenner et al., 1987, Vallier et al., 1991, Pearce et al., 1994*], but show a sharp change in composition at ~20.6^{o} S, within the central portion of the CELSC-N segment [*Escrig et al., 2009*]. This abrupt compositional change, which will be discussed in detail in section *4.5*, also corresponds to the disappearance of the axial magma chamber (AMC) reflector in MCS imagery, which is mostly continuous along the segments south of this transition zone [*Jacobs et al., 2007, Harding et al., 2000*].

2.21 Valu Fa Ridge (VFR)

The VFR comprises the southernmost two second-order segments of the Lau basin spreading system (*Fig. 3*). Each segment is separated by a non-transform step-over of 2-3 km and an overlap zone of ~1 km at the southernmost step-over at ~22^{o}37' S to nearly 10 km at the VFR-N/VFR-S overlap zone along ~22 ^{o}10-15' S. Third-order segments separated by non-transform offsets of less up to ~2 km were identified within the VFR-S, while third-order segmentation was not identified along the VFR-N. The VFR extends from the southern end of the Lau basin spreading system at ~22^{o}45' S to ~21^{o}26' S [*Martinez and Taylor, 2006*], where it abruptly terminates and activity jumps westward to the CELSC through a ~2 km wide non-transform offset [*Parson et al., 1990, Baker et al., 2006, Baker et al., 2010*]. The VFR is located ~40-60 km away from the active arc, approaching the arc toward the south, and therefore displays the strongest arc influence in its characteristics. The axis of the VFR is characterized by an inflated magmatically robust axial high, rising ~500 m to over 1000 m above the surrounding seafloor. The crest of the axis varies from a shallow, knife-like linear ridge to a deeper, discontinuous series of volcanic ridges and linear chains of cones. These variations in ridge crest morphology and depth are correlated with changes in style of volcanism and backscatter intensity, as well as relative subduction input based on ^{206}Pb /^{204}Pb ratios [*Jenner et al., 1987, Vallier et al., 1991, Loock et al., 1992, Escrig et al., 2009*]. Spreading rates along the VFR increase from 39 mm/yr at the southern end to 61 mm/yr near the northern end [*Martinez and Taylor, 2006*]. A nearly continuous axial magma chamber reflector was identified in MCS images at ~2.7-3 km beneath the seafloor under the entire length of the VFR, with the exception of small discontinuities near the VFR/CELSC overlap zone [*Harding et al., 2000, Jacobs et al., 2007*]. The lavas erupted along the VFR have a higher water content and a more andesitic composition than typical MORB lavas [*Jenner et al., 1987, Vallier et al., 1991*] due to the influence of water-rich melt rising from the subducting. Volcaniclastic debris from explosive arc volcanism commonly buries off-axis features along most of the axis, but the VFR is the only segment where ridge-sourced

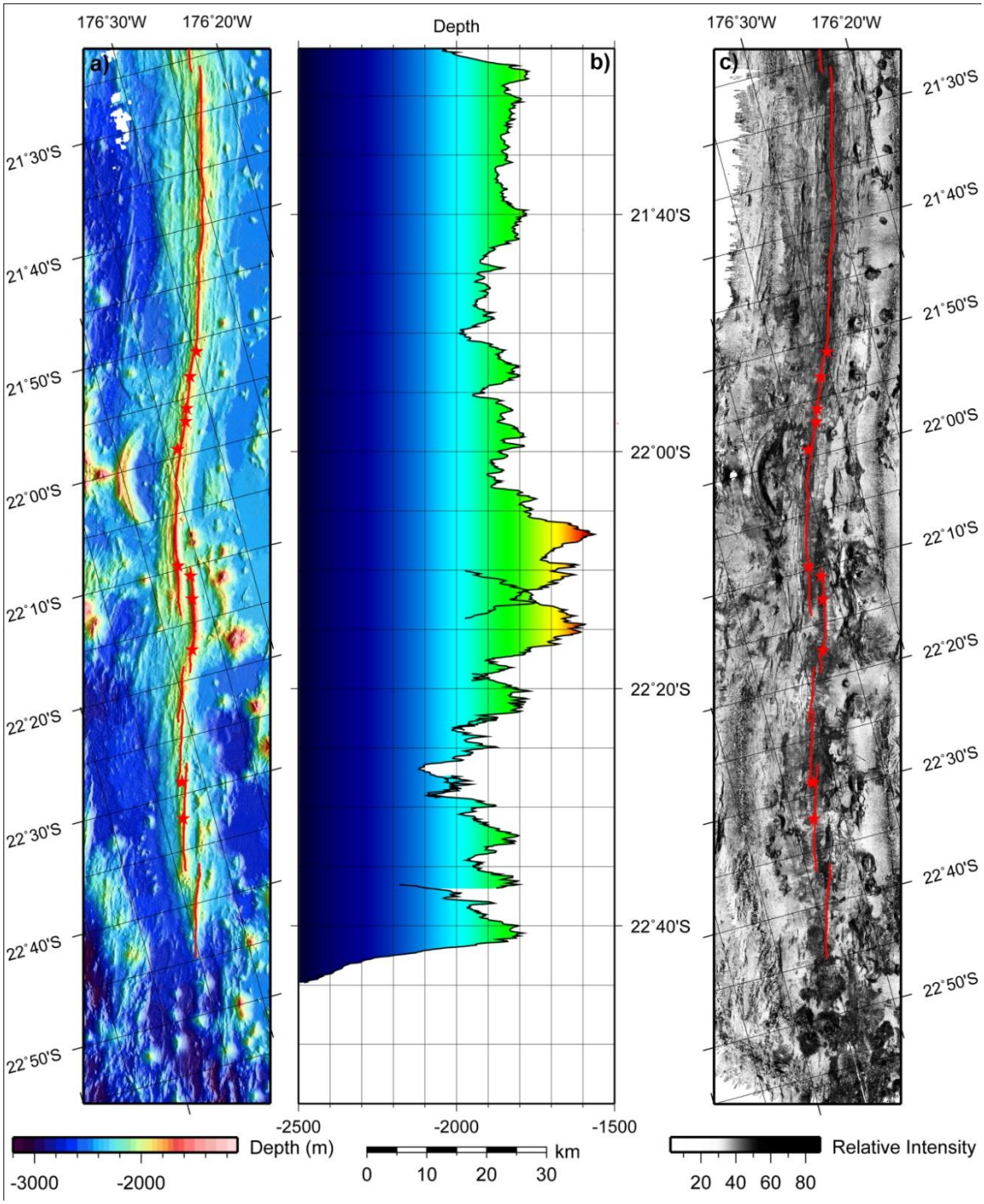

Figure 3: VFR summary figure showing both the VFR-N and VFR-S second-order segments. a) EM-120 bathymetry plot (20 m cell size); b) along-axis profile; c) EM-120 sidescan image (20 m cell size. Spreading axis picks are shown as red lines and identified hydrothermal vent sites are shown as red stars. [Data Sources: *Goodliffe, 1995, Martinez and Taylor, 2006, Martinez et al., 2008, Escrig et al., 2009*].

volcaniclastics are observed, and overall magmatism is much more abundant than MOR's with similar spreading rates [*Martinez and Taylor, 2006*]. Also, the style and abundance of volcanism can change very abruptly along axis, especially along the VFR-S segment, causing abrupt changes in morphology and axial depth. Depending on local source composition and local changes in subduction input, as well as changes in axial depth, the style of volcanism varies from explosive eruptions producing volcaniclastic debris to sheet flows, lobate flows, and small constructional cones and ridges. Faults and fissures in the VFR, where present, are relatively short and have small apparent throws (~10's of m at most), increasing in length and displacement toward the north as proximity to the axis decreases [*Martinez and Taylor, 2006*]. In general, faults are more easily identified on the west side of the axis where burial by volcaniclastic debris from the arc volcanoes is not as prevalent, although this may partially be due to a tectonic explanation such as asymmetric extension as well. Lava flows and ridge-sourced volcaniclastics also act to bury and obscure near-axis faults, further reducing fault exposure. Further north along the NELSC, near-axis faults have large enough throws to confine axial lava flows, whereas lava flows and volcaniclastic debris along the VFR commonly bury the small near-axis faults.

2.22 The Central Eastern Lau Spreading Center (CELSC)

The CELSC comprises two second-order segments along the central portion of the ELSC, extending for ~90 km from 21^{o}26' S in the south to 20^{o}32' S in the north, where it terminates in an abrupt non-transform step-over transition into the NELSC (*Fig. 4*) [*Martinez and Taylor, 2006*]. This segment varies in its proximity to the arc from ~60 km in the south to ~80 km at the northern end. Similar to the VFR, the CELSC has a mostly continuous axial magma chamber reflector along its length at a slightly shallower depth of ~2-2.5 km below the seafloor [*Harding et al., 2000, Jacobs et al., 2007*]. Faulting becomes more abundant compared to the VFR, increasing in length and apparent displacement toward the north. Spreading rates at the CELSC increase to 61-75 mm/yr, the axis deepens to 2000-2500 m, and the overall morphology changes to a broad

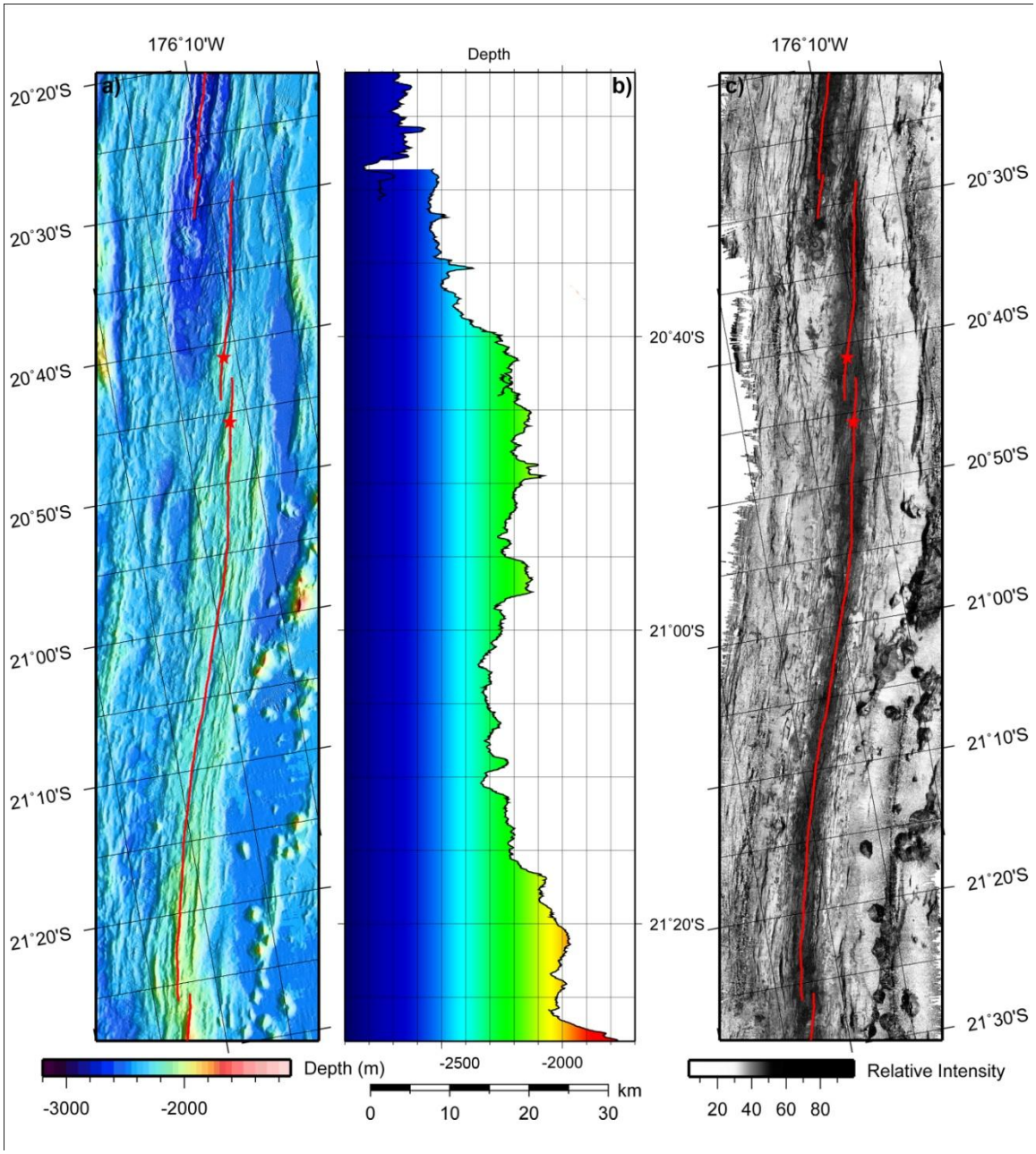

Figure 4: CELSC summary figure showing both the CELSC-N and CELSC-S segments. a) EM-120 bathymetry plot (20 m cell size); b) along-axis profile; c) EM-120 sidescan image (20 m cell size). Spreading axis picks are shown as a solid red line and identified hydrothermal vent sites are shown as red stars. Along the CELSC-S, we see a similar pattern to the VFR with relative morphologic highs near the ends and a relative low near the center of the segment. Along the CELSC-N, there are abrupt changes in morphology and axial depth associated with the 20.6^{o} S geochemical transition zone in the center of the CELSC-N segment. [Data sources: *Goodliffe, 1995, Martinez and Taylor, 2006, Martinez et al., 2008, Dunn et al., 2009, Escrig et al., 2009*].

axial high with a relief of <500 m. The morphology of the active spreading axis shows a lot of variability along its length, ranging from a narrow rounded peak constructed on a broad axial high, to a narrow valley within the axial high, to a nearly flat axis along the northern half of the CELSC-N. The flanks of the axial high and the off-axis crust consist of a complex pattern of discontinuous ridges and valleys at a wide range of scales, often asymmetric about the axis. Some ridges appear to have been cut by a failed spreading center or extensional faulting, while some appear to be fully intact. This level of on- and off-axis morphologic variability suggests that there is a strong element of temporal variation in melt supply which affects the long-term character of the axial and near-axis crust. Although evidence of temporal variation exists along the NELSC and VFR as well, the CELSC displays the widest range of variability in the on- and off-axis morphology. The characteristics of the CELSC demonstrate that on the scale of the entire ELSC axis, the spreading segments are making a relatively gradual transition in morphology and melt production from the heavily arc-influenced VFR in the south to the north end of the CELSC. These gradual changes are replaced by an abrupt change in morphology and a precipitous drop in magmatism within the CELSC-N segment, as the segment crosses the aforementioned 20.6^{o} S geochemical transition zone. This transition zone will be discussed in detail in section *4.5.*

2.23 The Northern Eastern Lau Spreading Center (NELSC)

The NELSC comprises two segments at the northern end of the ELSC, extending for ~160 km from the northern end of the ELSC at 19^{o}20' S to ~20^{o}32' S, and located ~80-100 km west of the Tofua arc (*Figs. 8-9*). The relatively gradual transition in first-order geologic and geophysical characteristics from the VFR through the CELSC abruptly stops at the ~5 km wide non-transform step-over between the CELSC-N and the NELSC-S, which overlap by ~6 km. The NELSC-S is being overtaken and shut down at both ends by the CELSC-N and the NELSC-N, which are propagating northward and southward respectively. The extinct basins west of the CELSC-N and east of the southern tip of the

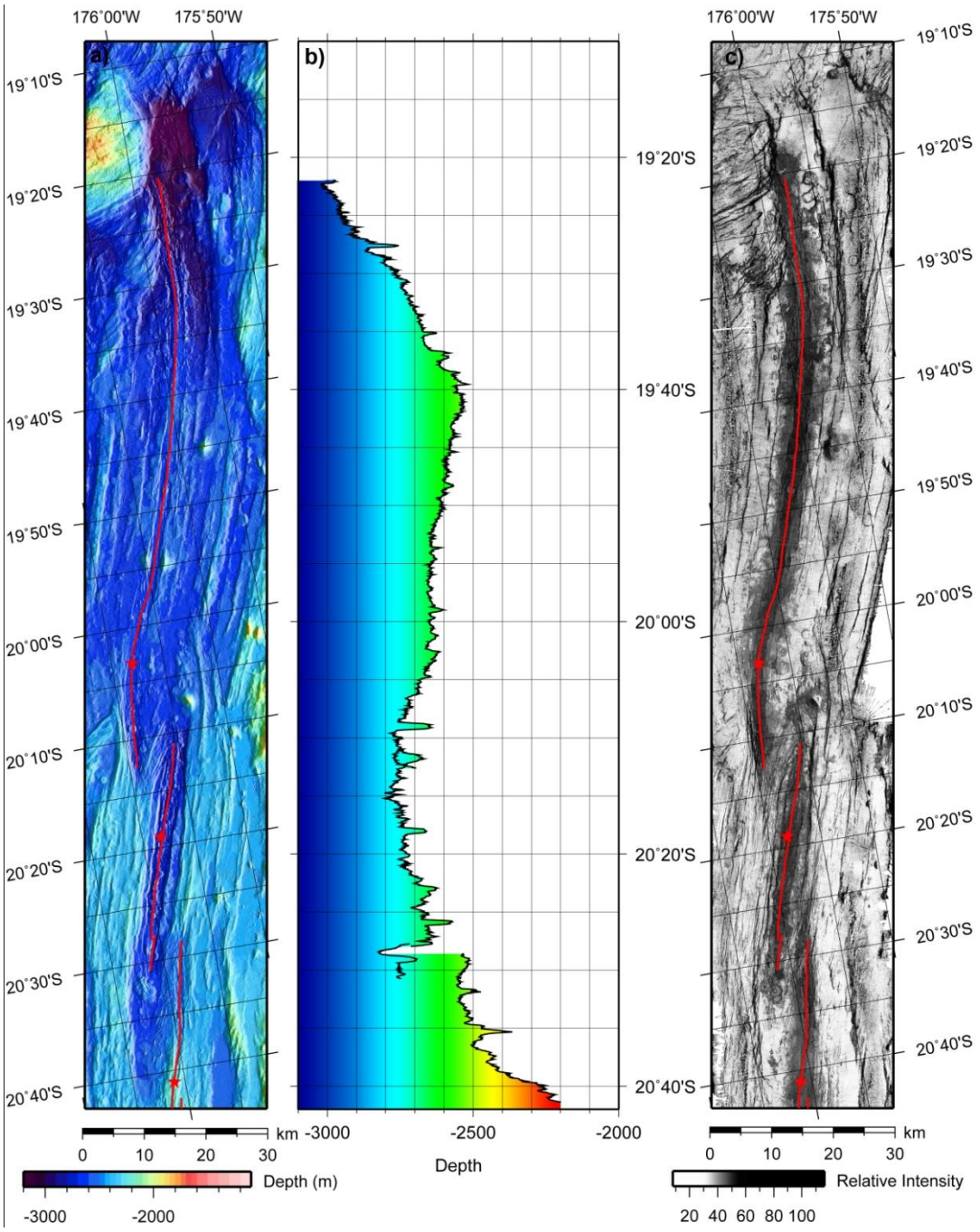

Figure 5: NELSC summary figure showing both the NELSC-N and NELSC-S. a) EM-120 bathymetry plot (20 m cell size); b) along-axis profile; c) EM-120 sidescan image (20 m cell size). Spreading axis picks are shown as red lines and identified hydrothermal vent sites are shown as red stars. The characteristics of the NELSC-S show how the axial morphology changes to a flat, deep axis in the aftermath of this sudden geochemical change. The NELSC-N, which has been spreading in this manner for much longer, shows the long term effects of this geochemical transition [Data sources: *Goodliffe, 1995, Martinez and Taylor, 2006, Martinez et al., 2008, Dunn et al., 2009, Escrig et al., 2009*].

NELSC-N show the previous extent of the NELSC-S. Across the CELSC-N to NELSC-S transition, there are abrupt changes in axial morphology associated with the 20.6^{o} S transition zone. The spreading rate continues the along-strike trend, increasing from ~76 mm/yr to a maximum of ~96 mm/yr at the northern limit of the ELSC [*Zellmer and Taylor, 2001*] and hydrothermal plume incidence also increases with spreading rate similar to MOR trends [*Baker et al., 2006, Baker et al., 2010*], but the morphology and structure of the ridge change entirely. MCS data from this segment show that the mostly continuous AMC reflector under the VFR and CELSC abruptly terminates at 20.6^{o} S and only discontinuous thin sills of melt remain under the NELSC [*Harding et al., 2000, Jacobs et al., 2007*]. As previously mentioned, this transition appears to actually begin within the CELCS-N segment, but the effects are much more strongly expressed along the NELSC-S, which has undergone this transition in the relatively recent past. Along the NELSC-S, the spreading axis becomes a deep flat floor reaching depths of 2500 m to over 3000 m, situated within off-axis crust that appears to have been formed in conditions similar to those at the current CELSC-S. The flat axis is situated within an axial valley bounded by one to two corresponding pairs of major faults with an apparent total displacement of ~400 m from the floor of the axis to the elevated off-axis crust. These faults have abnormally large apparent throws (~100 to 300+ m) compared to MOR's with similar spreading rates [*Martinez and Taylor, 2006, Dunn and Martinez, 2011*]. These large apparent throws can be explained through a combination of mechanisms that compliment the tectonic extensional forces: deflation and collapse of the axial magma chamber in response to the sharp reduction in magma supply, as well as a decrease in crustal thickness accompanying the abrupt change from lower density more andesitic lavas to higher density more basaltic lavas [*Dunn and Martinez, 2011*]. Along the NELSC-N, these faults virtually disappear as the off-axis crust becomes thinner and flatter, and the axis itself becomes almost entirely flat. Much smaller axis-bounding faults (10's of m throws at most) act as lateral barriers which confine the majority of lava flows generated within the neo-volcanic zone, creating a sharp boundary between the high backscatter of the

neo-volcanic zone and the low backscatter of the sediment-covered crust surrounding the axis.

3. Methodology

3.1 Data Collection

We compiled data from multiple cruises in the area to examine the characteristics of the ELSC and VFR at a scale and level of detail that is sufficient to observe and describe intra-segment geologic variation. Most of the mapping and interpretation was done using a combination of multibeam bathymetry and sidescan sonar data collected from various hull-mounted systems (EM-120 and EM-122) along with the much higher resolution near-bottom IMI-120 system which was used during the 2008 KM0804 and 2004 KM0410 cruises on *R/V Kilo Moana*. During both *R/V Kilo Moana* cruises, the IMI-120 was towed ~100 m above the seafloor, and an array of miniature autonomous plume recorder's (MAPR's) were tethered to the tow cable and beneath the sonar's depressor to detect hydrothermal plume signatures in the water column. During the KM0410 survey at least one tow was made on each side of the axis, spaced less than ~500 m apart, providing a narrow swath of data along the full length of the ELSC and VFR. The KM0804 survey focused on two portions of the ELSC and VFR to examine the possible extent of off-axis hydrothermal activity [*Baker et al., 2010*]. The northern KM0804 survey, which includes portions of four segments within the NELSC and CELSC, covered an area ~10 km wide by ~85 km long centered on the spreading axis. Tracks were spaced ~1 km apart, but as close as ~500 m in the vicinity of the ABE hydrothermal vent field, and the survey also included the Tow Cam and Kilo Moana vent fields [*Martinez et al., 2008, Baker et al., 2010*]. The southern KM0804 survey, which includes portions of 2 segments of the VFR, covered a ~5 km wide by ~55 km long area with ~700 m-spaced tracks, including the Vai Lili, Mariner, and Tui Malila vent sites [*Martinez et al., 2008*]. The IMI-120 has a resolution as fine as 1 m, filling the gap between the resolution of most hull-mounted systems (~30-100+ m), and ROV surveys which cover much smaller

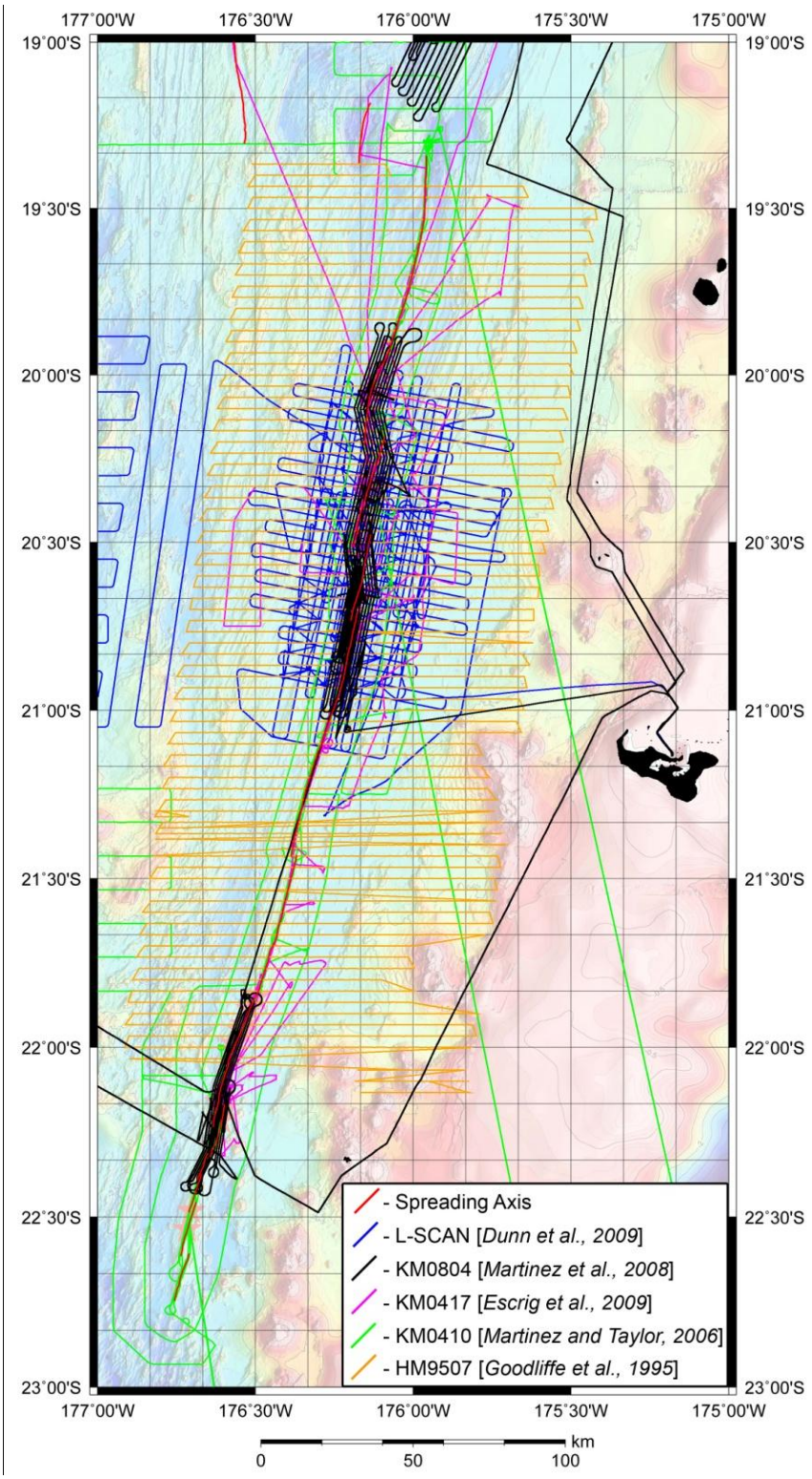

Figure 6: Plot of ship tracks for the five primary cruises from which bathymetry and sidescan data were utilized overlain on a bathymetry plot of the Lau basin. [Data sources: *Goodliffe, 1995, Martinez and Taylor, 2006, Martinez et al., 2008, Dunn et al., 2009, Escrig et al., 2009*].

areas at sub-cm resolution [*Ferrini et al., 2008*].

In order to increase the effective resolution and coverage area of the KM0804 EM-120 data, they were combined with sidescan and bathymetry data from multiple previous cruises in the area. The data sets used here were collected with the Seabeam system aboard *R/V Hakurei Maru* (HM9507), the EM-120 system aboard *R/V Kilo Moana* (KM0804, KM0410, KM0417), and the EM-122 system aboard *R/V Marcus G. Langseth* (L-SCAN) [*Goodliffe, 1995, Martinez and Taylor, 2006, Martinez et al., 2008, Escrig et al., 2009, Dunn et al., 2009*]. The combined bathymetry data set provides dense data coverage in the axial and near-axis regions, as well as off-axis coverage that extends well outside of the study area. The best results for the combined hull-mounted sidescan data came from combining the KM0804 and KM0410 surveys, which provided a coverage width of ~35 km along the entire axis, with as much as 60 km along the southern portion of the VFR. The MAPR data from the KM0804 and KM0410 cruises [*Baker et al., 2006, Baker et al., 2010*], as well as geochemical and seismic data collected along the ELSC and VFR in previous cruises were also correlated with the primary sidescan and bathymetry data sets [*Jenner et al., 1987, Vallier et al., 1991, Loock et al., 1992, Turner et al., 1999, Harding et al., 2000, Peate et al., 2001, Jacobs et al., 2007, Dunn, et al., 2009*, *Escrig et al., 2009, Dunn and Martinez, 2011*].

3.2 Data Processing Methods

3.21 Hull-mounted sidescan data

The hull-mounted EM-120 sidescan sonar data from the KM0804 and KM0410 cruises was one of the most important data sets for mapping and interpretation. The KM0804 and KM0410 surveys were planned with closely spaced IMI-120 track lines, so the much wider swaths of the hull-mounted EM-120 data overlap extensively and were collected at slow ship speeds of about 1.5 to 2 knots, providing a dense coverage area near the axis [*Martinez and Taylor, 2006, Martinez et al., 2008*]. Although the inherent resolution of the 12 kHz

multibeam data is several tens of meters, the dense overlapping data coverage made it possible to grid the sidescan data with a cell size as fine as 10 m using Generic Mapping Tools (GMT) [*Wessel and Smith, 1998*]. Furthermore, this data redundancy made it possible to filter out the majority of the nadir and swath edge distortion inherent to sidescan surveys and create an image which is much smoother and easier to interpret. The primary difference between the processing method used in this study and those that are typically used for this type of data is that the individual beam data were extracted, combined, filtered, and gridded together, rather than superimposed as individual swaths.

3.22 Hull-mounted bathymetry data

The combined hull-mounted bathymetry data set was important for examining changes in morphology and mapping tectonic and volcanic features. Compilation of data from 4 to 5 previous cruises provided much denser data coverage than any single cruise could provide [*Goodliffe, 1995, Martinez and Taylor, 2006, Martinez et al., 2008, Dunn et al., 2009, Escrig et al., 2009*]. This made it possible for data that typically has a resolution of ~50-100 m to be gridded with a cell size as fine as 10 m, providing some of the most detailed bathymetry maps of the ELSC and VFR axis to date. Combining, filtering, and plotting of the bathymetry data was also done using GMT [*Wessel and Smith, 1998*].

3.23 Deep-towed sidescan and bathymetry data

The IMI-120 sidescan and bathymetry data were gridded at a cell size of 2 m, providing highly detailed imagery of the ELSC and VFR axes and near-axis regions. Data collected with the IMI-120 system requires navigational correction because the deep-towed instrument's position cannot be directly measured and is instead estimated based on the ship position from the GPS/inertial navigation system and the digitally-monitored length of the tow cable [*Martinez et al., 2008*]. When the ship changes course or a deep-ocean current is encountered, the position of the instrument deviates from the ship's track and can cause feature

locations to be off by as much as 100's of m. Software packages developed by the Hawaiian Mapping Research Group (HMRG) at the University of Hawaii at Manoa [*R. Davis, personal communication, 2009*] were utilized to graphically correct the navigation based on feature matching between the shipboard multibeam data and the deep-towed sidescan and bathymetry data. However, the nature of the data sets and the limitations of the program meant that while it was possible to significantly improve the IMI-120 navigation, inaccuracies and imperfect agreement in localized areas on the order of ~100 m or less are inevitable. More details on this method are provided in the appendix. Also, a new manual method was developed for blending overlapping edges of sidescan swaths using Adobe Photoshop CS3® to selectively trim parts of the overlapping swaths where the underlying swat showed more information. Because of the somewhat irregular nature of the quality of deep-towed sidescan data near swath edges, automatic methods for blending overlapping edges or cutting them off at a certain distance from the nadir are unable to determine which of the overlapping swaths contains the "best" data. Consistent display of the best data in swath overlap areas can only be done with a manual method such as the one used in this study, the details of which are contained in the appendix.

3.3 Other data sets

While the sidescan and bathymetry data were the most important data sets for mapping and interpretation, other geophysical and geochemical data from the ELSC and VFR were utilized to gain more insight into the relationships between various processes along the ridge. The MAPR data from the KM0804 and KM0410 cruises were used to correlate hydrothermal activity with the ridge structures and help understand how it might relate to the observed intra-segment variations [*Baker et al., 2006, Baker et al., 2010*]. For the KM0804 MAPR data, the navigational corrections that were made to the IMI-120 sidescan and bathymetry data were applied to the MAPR data as well to provide more accurate locations for plume signatures. Geochemical data from samples collected along the majority of the ELSC and VFR axis were examined mostly to help understand

how the subduction input varies along the axis so that this variation could be correlated with changes in ridge morphology and volcanic activity [*Jenner et al., 1987, Vallier et al., 1991, Loock et al., 1992, Escrig et al., 2009*]. Seismic data from the L-SCAN experiment [*Dunn et al., 2009, Dunn and Martinez, 2011*] and a previous MCS study along the ELSC [*Harding et al., 2000, Jacobs et al., 2007*] were utilized to examine the extent and continuity of the AMC reflector under the spreading axis and determine its relationship to the observed intra-segment variation, as well as look at changes in crustal density and thickness based on seismic velocities.

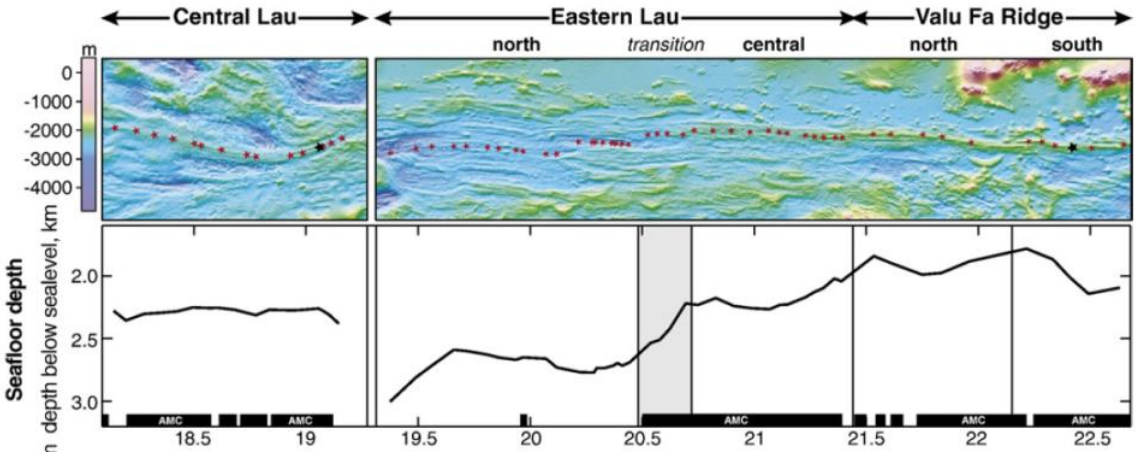

Figure 7: Summary of multi-channel seismic results from 12/99 survey. Top: bathymetry plot from the CLSC through the ELSC and VFR; bottom: along-axis profile and continuity of AMC reflector (black bar along base of fig), note gap under NELSC and small discontinuities near VFR/CELSC step-over. [Taken from: *Jacobs et al., 2007*]

3.4 Mapping Methods

The features marked on the geologic maps of each segment were all manually mapped using Adobe Illustrator CS3®. The EM-120 sidescan and bathymetry data are the primary basemaps on which the features are mapped. Sidescan imagery proved useful for identifying fault scarps and the limits of lava flows, while the bathymetry was more useful for identifying volcanic features, confirming feature locations, and understanding the morphology of the seafloor. IMI-120 sidescan data proved to be useful for identifying and mapping small

features, distinguishing faults from other lineations, determining dip direction for small faults, and identifying the areas of most recent volcanism. Faults were primarily identified based on the high backscatter return from the face of the scarp in the sidescan imagery, and are all mapped along the top of the scarp. Faults with displacements of over ~10-20 m could generally be identified in the bathymetry data as well, but anything smaller could only be seen in the sidescan imagery. The limits of volcanic features are often difficult to distinguish in the IMI-120 sidescan imagery due to the increased nadir and swath edge distortion, so the combined hull-mounted bathymetry and sidescan plots were used as the primary means to map volcanic features. Mapping of volcanic features focuses on constructional features that are relevant to what is discussed in the study, including: prominent off-axis seamounts, ridge crest volcanic cones along the VFR-S, and other prominent or unique on-axis features. Recent lava flows with high backscatter in the sidescan data were mapped where the boundaries of the flows could be distinguished, although this can be ambiguous near the axis where many flows overlap each other. Mass wasting was noted mostly in regions dominated by low backscatter sediment or volcaniclastic material along steep flanks, but slumping was also mapped along portions of the larger fault scarps.

4. Observations and Results

4.1 Summary of intra-segment variations

The entire ELSC and VFR spreading system is a single first-order segment as defined by *Macdonald et al.,* 1991a, but due to the along-axis variations, it has traditionally been divided into the NELSC, CELSC, and VFR based on the distinctive characteristics of each. The six segments discussed in this study (*Fig. 2*) are each separated by a non-transform offset of approximately 2 to 5 km, which puts them in the second-order classification of *Macdonald et al., 1991a*. Smaller 3rd and 4th order discontinuities can further be observed within each segment. The intra-segment variations in axial morphology and volcanism are very distinct and strongly expressed along the segments closest to the arc,

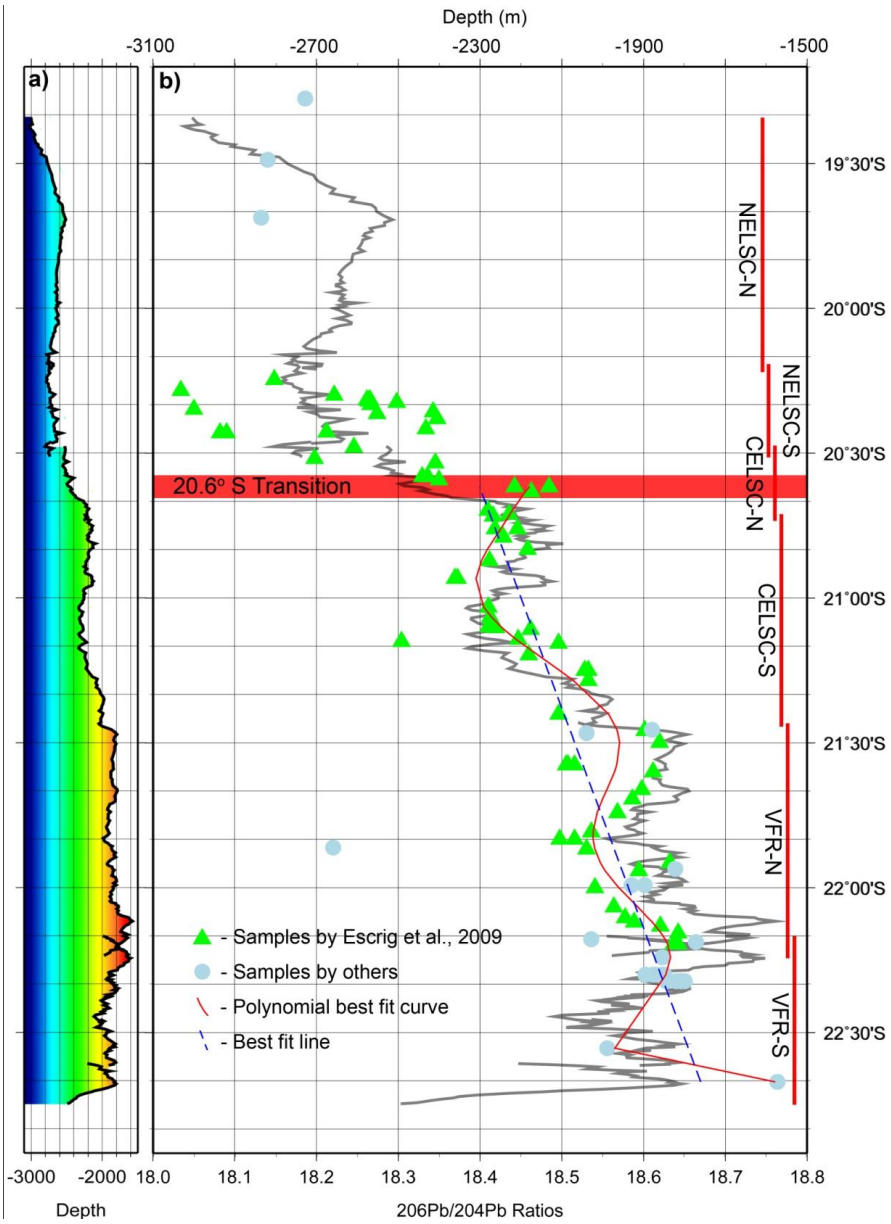

Figure 8: Summary figure showing intra-segment variations. a) along-axis profile of the entire ELSC and VFR; b) plot of all ^{206}Pb /^{204}Pb ratios of near-axis lava samples overlain on an exaggerated profile. 2nd order segments are shown schematically on the far right side. The linear first-order trend of decreasing subduction influence toward the north is shown as a blue dashed line and the 10th order robust polynomial fit is shown as a solid red curve. *Escrig et al., 2009* first recognized the sinusoidal variation along the VFR-N, which has been extended through the rest of the CELSC-S for this study. Green triangles are from the KM0417 cruise [*Escrig et al., 2009*], blue circles are samples from others [*Jenner et al., 1987, Vallier et al., 1991, Loock et al., 1992, Peate et al., 2001*]. The most important features of this plot are the pattern of relative highs in both Pb ratios and axial depth near 2nd order segment ends from the southern end to the 20.6^{o} S transition, and the sudden drop in both axial depth and Pb ratios north of the 20.6^{o} S transition.

but become more subtle as the spreading center moves further from the arc, in a similar manner to the first-order variation. These intra-segment variations display a positive correlation with relative subduction input as indicated by $^{206}Pb/^{204}Pb$ ratios in axial lavas collected along the ELSC and VFR (*Fig. 8*) [*Escrig et al., 2009*], and may be the expression of corresponding along-strike spatial and/or temporal variations in the mantle wedge beneath the spreading systems. Since Pb is a fluid-mobile element, this ratio tends to co-vary with water content, and it is a widely used indicator of relative slab input in lava samples [*Escrig et al, 2009*]. Along the VFR-N and CELSC-S these ratios appear to vary in a systematic pattern superimposed on a linear trend (*Fig. 8*), with relative highs that coincide with the ends of the VFR-N and CELSC-S segments and relative lows that correspond to the centers of these segments. *Escrig et al., 2009* were the first to describe the roughly sinusoidal variation in $^{206}Pb/^{204}Pb$ ratios along the VFR-N and the southern portion of the CELSC-S; all but four of their samples fell along a smooth sinusoidal trend. Axial depth and relief along these two segments generally follow this sinusoidal trend, with relatively shallow, high relief portions of the axis corresponding to relative highs in $^{206}Pb/^{204}Pb$ ratios and relative Pb lows corresponding to relatively deep, low relief portions of the axis. The lack of sampling along the VFR-S axis makes the same correlation impossible, but it too shows a similar cosine-like along-axis pattern in morphology and axial depth. Since relative highs in subduction influence should correspond to relative highs in melt production, it shouldn't be surprising to find higher relief and shallower depths associated with local highs in subduction influence, but this is the first time a correlation like this has been identified in a mature backarc spreading system. Another major feature of the Pb trend is the sudden drop in ratios north of 20.6^{o} S within the central portion of the CELSC-N (*Fig. 8*). This corresponds to an abrupt change in crustal density and thickness over a distance of a few km, and the values no longer display any discernable patterns or trends north of this transition [*Escrig et al, 2009, Dunn and Martinez, 2011*]. This abrupt drop in $^{206}Pb/^{204}Pb$ ratios correlates directly with an abrupt change in ridge morphology from a broad axial high to a nearly flat axis, which

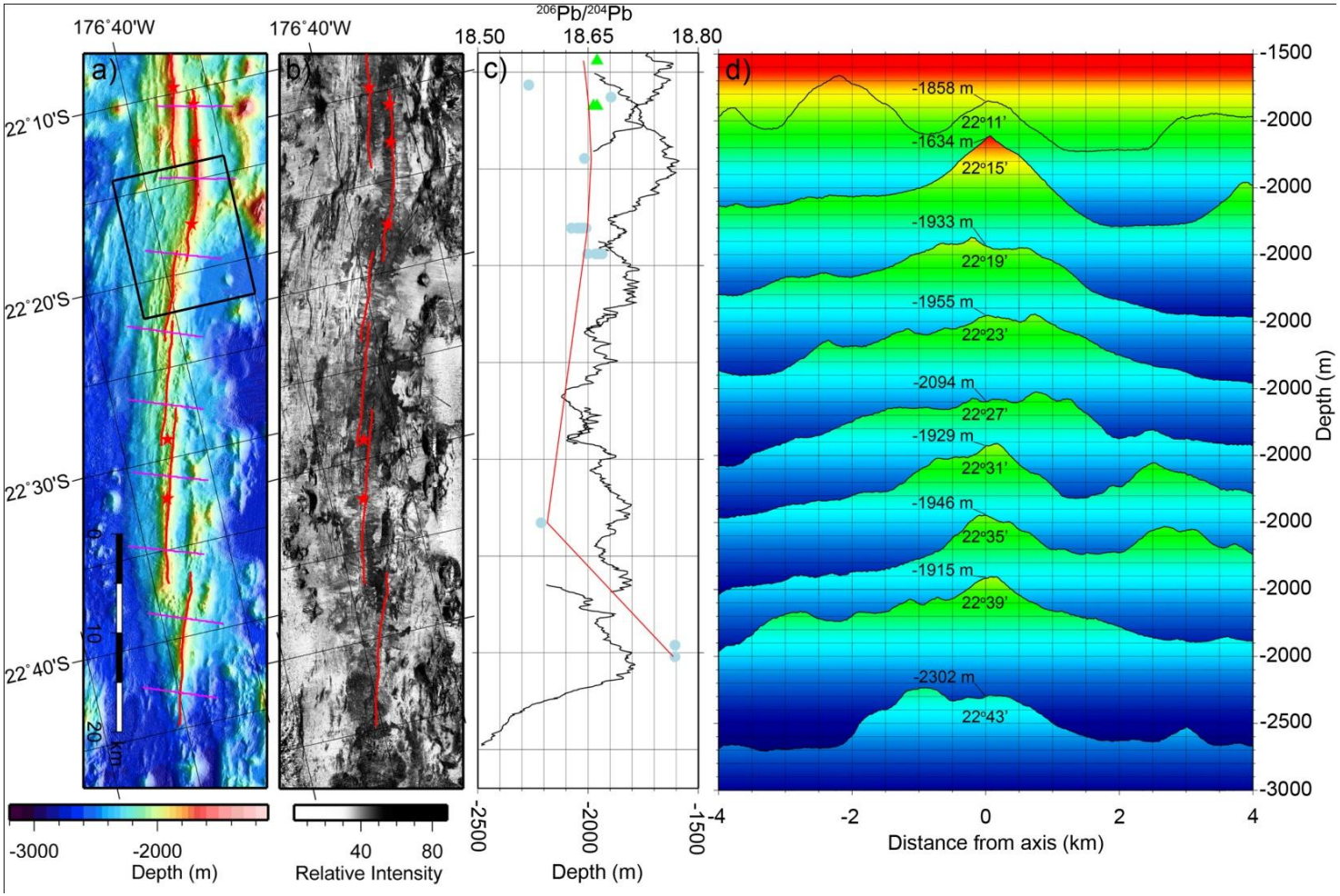

Figure 9: VFR-S summary figure. a) EM-120 bathymetry (20 m cell size); b) EM-120 sidescan (20 m cell size); c) along-axis profile overlain with $^{206}Pb/^{204}Pb$ ratios and the best fit curve; d) across-axis profiles. [Data sources: Jenner et al., 1987, Vallier et al., 1991, Loock et al., 1992, *Goodliffe, 1995, Martinez and Taylor, 2006, Martinez et al., 2008, Escrig et al., 2009*].

also occurs over the distance of a few km. This transition will be discussed in detail in section *4.*5. Although we lack the data to definitively prove a causal connection between variations in $^{206}Pb/^{204}Pb$ ratios and variations in ridge morphology at this stage, the correlation is worthy of consideration. The following sections will discuss the geologic variations observed within each of the six second-order segments along the ELSC and VFR, focusing on the observed correlation with $^{206}Pb/^{204}Pb$ ratios and variations in axial morphology.

4.2 Valu Fa Ridge, southern segment (VFR-S)

The Valu Fa Ridge, southern segment (VFR-S) is the southernmost spreading center covered by the KM0804 survey and the closest to the Tofua arc (*Fig. 9*). The segment extends for ~66 km from ~22°10' S to ~22°45' S, where it terminates at a ~2.5 km wide and ~7.5 km long overlapping step-over transition with the VFR-N. The VFR-S segment can be broken into four third-order segments separated by non-transform offsets of ~300 m to just over 2 km. The axis of the VFR-S varies from a narrow, strongly peaked, smooth-flanked ridge to a wider, lower relief axial high topped with short discontinuous ridge segments and linear chains of cones which can be either oblique or parallel to the overall trend of the axis. The strongly peaked smooth-flanked portions of the ridge generally correlate with areas that are dominated by volcaniclastic debris, identified by its low backscatter intensity and distinct texture in the sidescan data. These volcaniclastic-dominated portions are also typically associated with small cones along the crest of the ridge. The best example of this morphology is along the northern portion of the segment from ~22°10'-16' S (*Figs. 10-11*), although similar volcaniclastic-dominated portions can be observed from ~22°20-23' S, 22°31-33' S, and 22°39-42' (*Fig. 9*). The portions of the axis with lower relief and a discontinuous ridge crest correlate well with patches of volcanism with high acoustic reflectivity, mostly consisting of sheet and lobate flows. The best example of one of these zones is from ~22°16-20' S (*Figs. 10-11*), although similar zones can be observed from ~22°23-31' S, ~22°34-39' S, and at the southern tip of the VFR-S from ~22°42-45' (*Fig. 9*). Along the VFR-S, unlike the

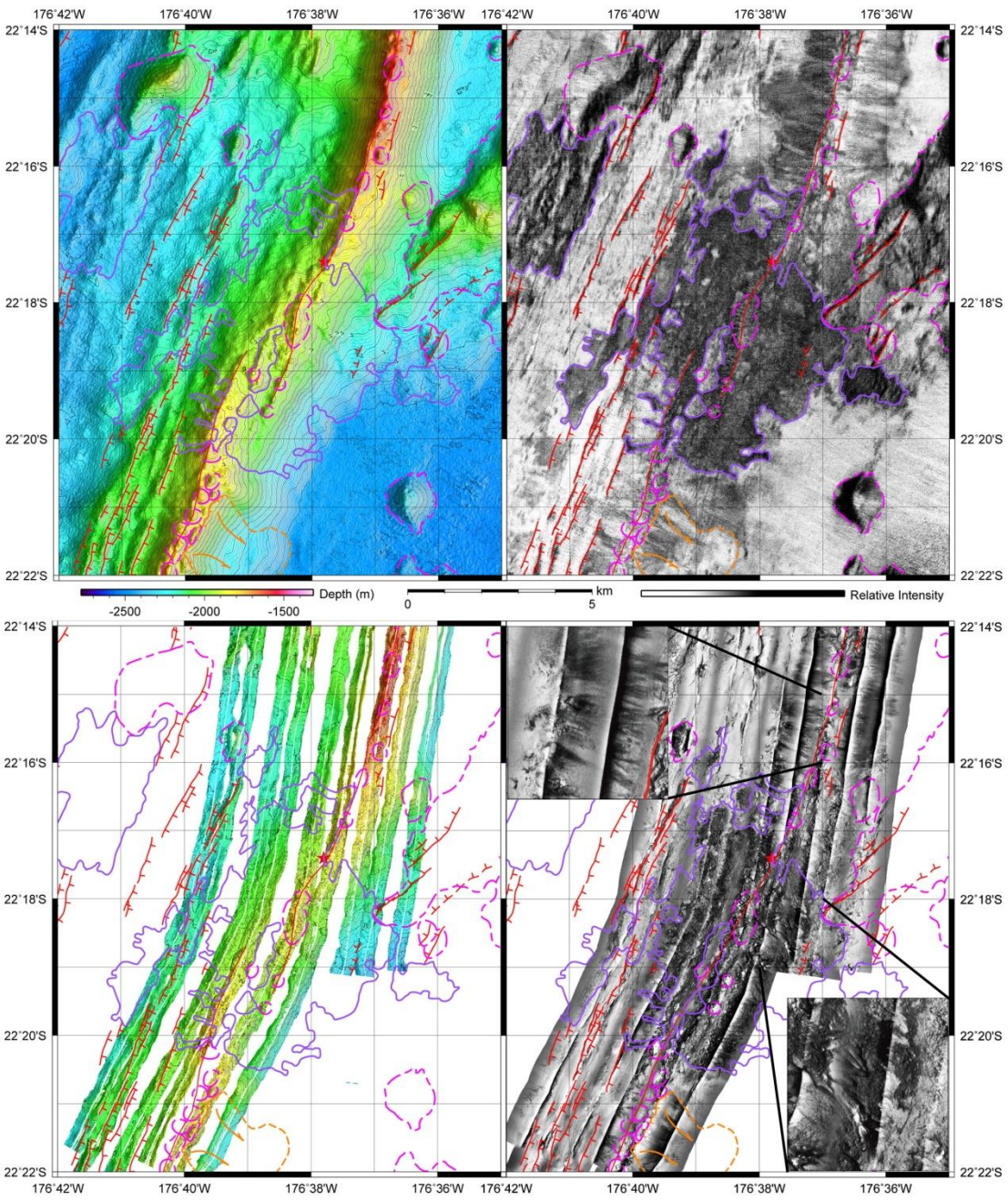

Figure 10: VFR-S, sonar imagery of northern transition zone. a) EM-120 bathymetry (10 m cell size); b) EM-120 sidescan (20 m cell size); c) IMI-120 bathymetry (2 m cell size); d) IMI-120 sidescan (2 m cell size, insets show textures). See *Fig. 11* for discussion. Spreading axis picks are shown as solid red lines, identified hydrothermal vent sites are shown as red stars, faults are mapped as red lines with tick marks pointing in the apparent dip direction and dashed where approximate, constructional volcanic features are outlined with dashed magenta lines, recent mappable lava flows are outlined with solid purple, and mass wasting features are indicated with orange lines. [Data sources: *Goodliffe, 1995, Martinez and Taylor, 2006, Martinez et al., 2008*].

rest of the segments toward the north, there are very distinct boundaries between zones of high backscatter lava flows and low backscatter volcaniclastic sedimentation, while the associated changes in axial morphology are similarly abrupt. These abrupt and easily identifiable changes in morphology and volcanism make this the ideal location to test the correlation between local variations in subduction influence and the geologic variations seen along the axis. Unfortunately sampling and geochemical data along this segment are limited, there are only 5 locations along the VFR-S axis where $^{206}Pb/^{204}Pb$ ratios were measured, and they are not distributed favorably to get a reasonable idea of how the ratios vary along the length of the segment [*Jenner et al., 1987, Vallier et al., 1991, Loock et al.,1992*]. The dense sampling from the KM0417 cruise ends at the southern end of the VFR-N [*Escrig et al., 2009*], making it difficult to make the same small-scale correlations between subduction input and axial morphology and volcanism like those along the segments to the north.

4.21 Variations in morphology and volcanism (VFR-S)

The overall along-axis pattern in morphology along the VFR-S is similar to the pattern seen along the VFR-N and CELSC-S (sections *4.3 and 4.4*), where the segment ends are relatively shallower and higher relief than the center of the segment (*Fig. 9*). Toward the southern end, near the transition from organized spreading to diffuse spreading, the axis deviates from this trend and dives down steeply. Otherwise, the deepest part of the axis is along the central portion around 22°27' S, reaching depths of -2100 m, while depths along the northern end decrease to -1600 to -1700 m, and the axis of the southernmost segment is as shallow as -1900 m (*Fig. 9*). However, the VFR-S is unique with respect to the amplitude of along-axis variation within this overall pattern, which is 5 to 10 times greater than at MOR's with similar spreading rates [*Wiedicke and Collier, 1993*], and the abrupt nature of many of these variations. In order to understand the details of variations in morphology and volcanism along the VFR-S, we will look at the portion of the axis along which these variations are best expressed. *Figs. 10 and 11* show a close up view of the axis between 22°14' S and 22°22' S,

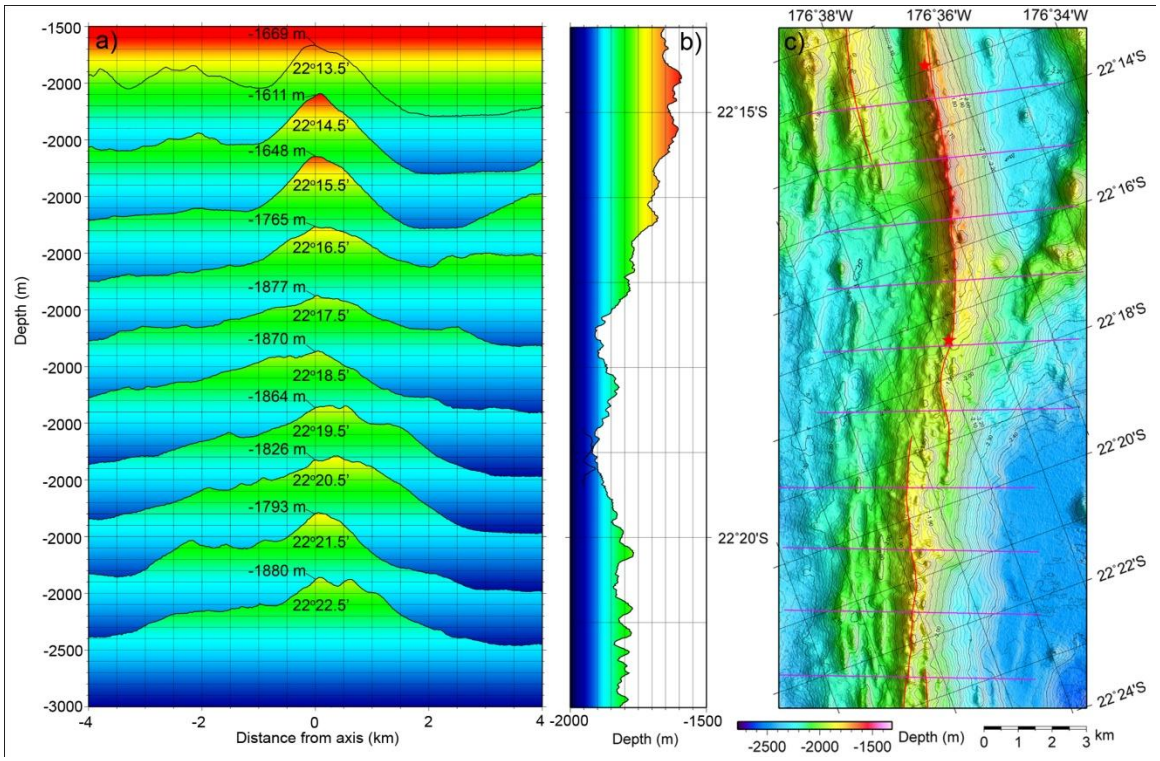

Figure 11: VFR-S, profiles along northern transition zone. a) across-axis profiles; b) along-axis profile; c) EM-120 bathymetry (10 m cell size) showing profile locations. All across-axis profiles in this and later figures are shown with 2x vertical exaggeration to emphasize morphologic changes. See *Fig. 10* for corresponding bathymetry and sidescan images. The bathymetry plots and profiles show the change from a narrow, strongly peaked, smooth-flanked axial high in the north, with an abrupt transition across ~22^{o}17'-18' S to a broader, lower relief axial high with more variable flank topography. The central portion is 200 to 300 m deeper than the northern portion and dominated by highly reflective sheet and lobate flows with minimal volcaniclastics. South of this zone by ~22^{o}20' S, the axis abruptly changes back to a narrow axial high dominated by low backscatter volcaniclastics, although this portion is deeper and the flanks are more irregular than the northern portion. On the bathymetry plot, spreading axis picks are shown as a red line, identified hydrothermal vent sites are shown as red stars, and profile locations are shown with magenta lines. [Data sources: *Goodliffe, 1995, Martinez and Taylor, 2006, Martinez et al., 2008*].

individual chains of volcanic cones arranged in an almost en-echelon configuration oblique to both the axial trend and the opening direction. The sidescan data show an abrupt increase in backscatter intensity and a change in texture consistent with a transition from volcaniclastic debris to sheet and lobate lava flows. The 2 m IMI-120 sidescan data is especially useful here for centered

on the best example of a high backscatter zone dominated by effusive volcanism bounded along-axis by areas dominated by low backscatter volcaniclastic sediments. Moving south from the overlap zone with the VFR-N on the north side of the plot, the VFR-S ridge axis is a strongly peaked, smooth-flanked ridge rising to as shallow as -1600 m, and the backscatter intensity and texture are consistent with volcaniclastic debris erupted from the ridge axis. By ~22^{o}16' S, the peaked axis rapidly transitions into a lower relief, wider axial high rising to only -1850 to -1900 m, and the uniform ridge crest breaks down into distinguishing between the various volcanic textures (*Fig. 10*). Within the 1' square bounded by 176^{o}37-38' W and 22^{o}18-19' S, a particularly large lobate flow extends with a finger-like geometry for over 1.5 km in a SE direction down the ridge flank (*Fig. 10d inset*). Some of the best examples of sheet flows, which can be identified by their high backscatter intensity and fine-scale surface roughness (*Fig. 10d inset*), can be seen from ~22^{o}17-18' on the west flank of the ridge, where they appear to be the dominant style of volcanism. Around ~22^{o}20' S, there is another abrupt transition back to a strongly peaked smooth-flanked ridge draped with low backscatter volcaniclastic debris, although the ridge crest here is deeper and more irregular than the northern volcaniclastic-dominated portion. Although the limits of individual zones and the morphologic changes are not quite as obvious toward the south, this same pattern is repeated two more times along the southern portion of this segment, in the locations mentioned in the previous section (*Fig. 4*). The strong morphologic response to these changes in style of volcanism indicates that these are not simply variations over the time-scale of individual eruptive episodes but that these may be longer-term features of the ridge.

4.22 Variations in faulting and hydrothermal activity (VFR-S)

Faulting along the VFR-S is less abundant overall than any segment toward the north, and shows a general trend of decreasing abundance toward the south. The pattern of faulting follows the general first-order trend correlated with increasing subduction influence and melt production toward the south and

does not appear to be sensitive to the local changes in morphology and volcanism. Exposed faults are concentrated within a triangular zone defined by the pseudo-faults on either side that narrows toward the south. Fault throws are at most a few 10's of m, while the vast majority are not large enough to be expressed in the ship multibeam bathymetry grids. Faults are better exposed on the west side of the axis furthest from the arc volcanoes, although it is unclear whether seafloor exposure is affected solely by burial from arc volcaniclastics and pelagic sediments or whether there is actually a partial tectonic explanation (i.e. asymmetric spreading or variable amounts of extension on each plate). As is the case along the rest of the VFR, ridge-sourced lava flows and volcaniclastics easily bury the small near-axis faults, further reducing fault exposure along this segment. Hydrothermal activity also shows a pattern of generally increasing toward the north, but there is a major spike in activity near the overlap zone with the VFR-N, where 3 vent fields have been identified: Mariner and Vai Lili on the VFR-S itself, and Tahi Moana 4 on the VFR-N [*Baker et al., 2006, Nautilus Minerals, Inc., 2009, Baker et al., 2010*]. Toward the south, at least 3 more vent fields were identified: Tahi Moana 6, 3, and 5 from north to south, but these don't appear to be as active as those near the overlap zone [*Nautilus Minerals, Inc., 2009*].

4.3 Valu Fa Ridge, northern segment (VFR-N)

The VFR-N segment extends for ~90 km from ~22^{o}14' S to ~21^{o}26' S where it terminates in a ~1.6 km wide and ~1 km long non-transform step-over with the CELSC-S (*Fig. 12*). Unlike the VFR-S, the VFR-N consists of one continuous second-order segment for its entire length. There are lower order bends and potential discontinuities on the scale of a few 100 m at most, but these likely represent temporary changes in the location of the active spreading or possible third-order segmentation. Intra-segment variations in general are expressed in a different manner than along the VFR-S. Changes along the axis are much more gradual and there are no longer sharp boundaries between zones of contrasting volcanic and morphologic characteristics. Even though the

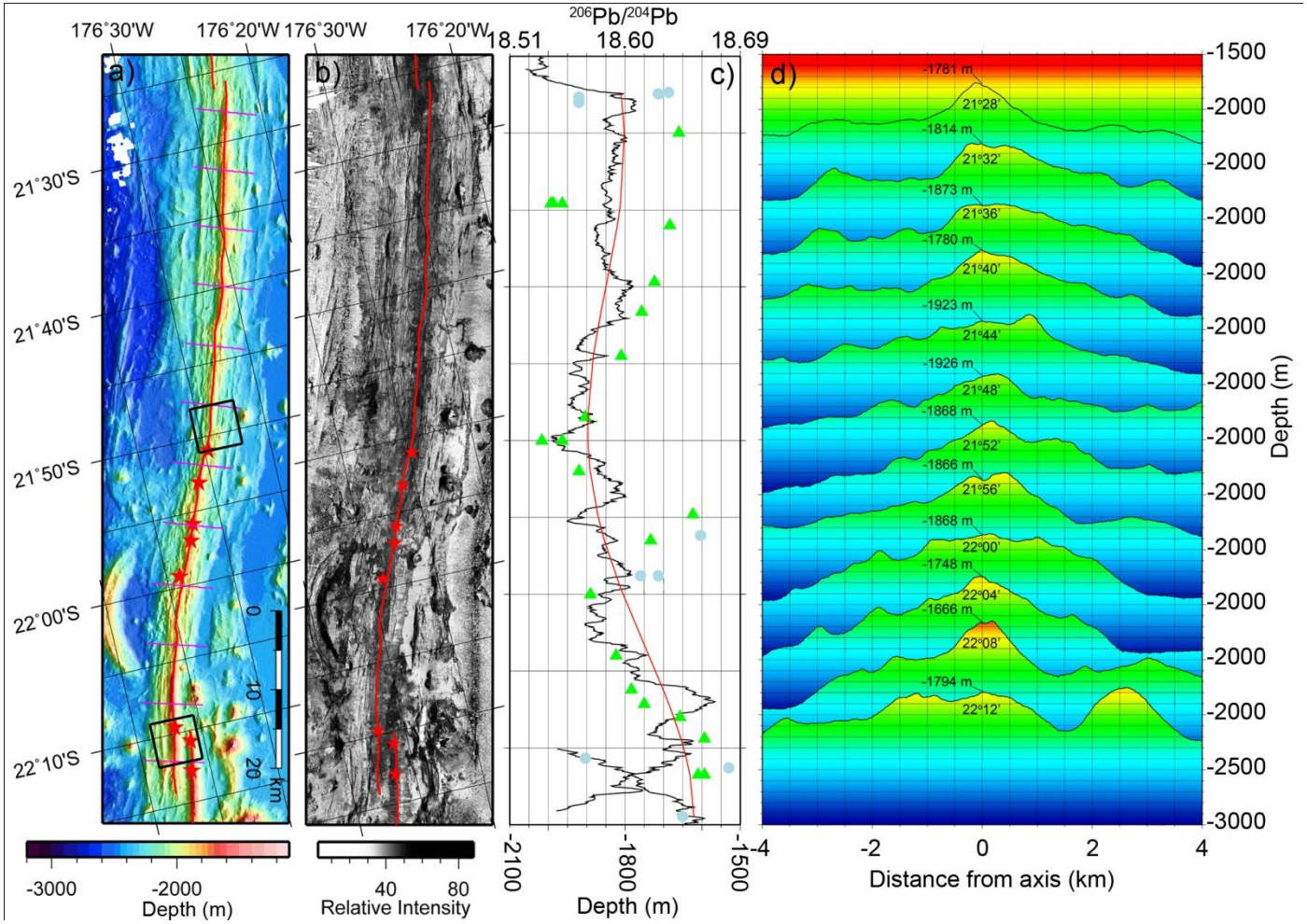

Figure 12: VFR-N summary figure. a) EM-120 bathymetry (20 m cell size); b) EM-120 sidescan (20 m cell size); c) Along-axis profile overlain with $^{206}Pb/^{204}Pb$ ratios and the best fit curve; d) Across-axis profiles. [Data sources: *Loock et al., 1992*, *Goodliffe, 1995, Martinez and Taylor, 2006, Martinez et al., 2008, Escrig et al., 2009*].

morphology of the axis along this segment is consistently an axial high and it does not change as abruptly as the VFR-S, there are significant variations in geologic characteristics that can be observed. In general, the axial ridge is shallower and higher relief near the segment ends and deeper and lower relief near the center, a similar trend to the VFR-S and CELSC-S. The $^{206}Pb/^{204}Pb$ ratios vary in a similar manner along the segment, with the best-fit polynomial curve showing a similar pattern of highs near the ends and a relative low near the center (*Figs. 8, 12*). Also, the highest $^{206}Pb/^{204}Pb$ ratios along this segment are near the southern end where the axis is shallowest and most strongly peaked, and the lowest values are at the center of the segment at around $21^{o}50'$ S, where the axis is deepest (~1900-2000 m) and axial relief is lowest (*Fig. 12*). *Escrig et al., 2009* also noted geochemical affinities between some of the arc volcanoes and portions of the VFR-N that project along the same slab flow lines. Two of these volcanoes, Ata and Volcano 3, line up with the southern and northern ends of the VFR-N, respectively, suggesting that there may be a deep connection between the mantle sources feeding the spreading axis and the arc volcanoes [*Escrig et al., 2009*]. A third volcano, Volcano 4, lines up nicely with two anomalously high $^{206}Pb/^{204}Pb$ values between 21.9^{o} and 22.0^{o} S that fall outside of the sinusoidal trend (*Figs. 3-4*), provided a plausible explanation for this departure from the trend.

4.31 Variations in morphology and volcanism (VFR-N)

The changes in axial morphology along the VFR-N are more subtle and gradual, and there are no longer sharp boundaries between zones that are dominated by one type of volcanism. Rather than alternating zones dominated by either sheet/lobate flows or volcaniclastics which characterizes the VFR-S, the majority of the VFR-N axis is dominated by sheet flows, with minor amounts of pillow lavas and minor volcaniclastics toward the southern end of the segment. The distribution of different styles of volcanism doesn't show an obvious along-axis pattern that can be correlated with other characteristics. There are no longer any portions of the VFR-N that are dominated by volcaniclastics erupted

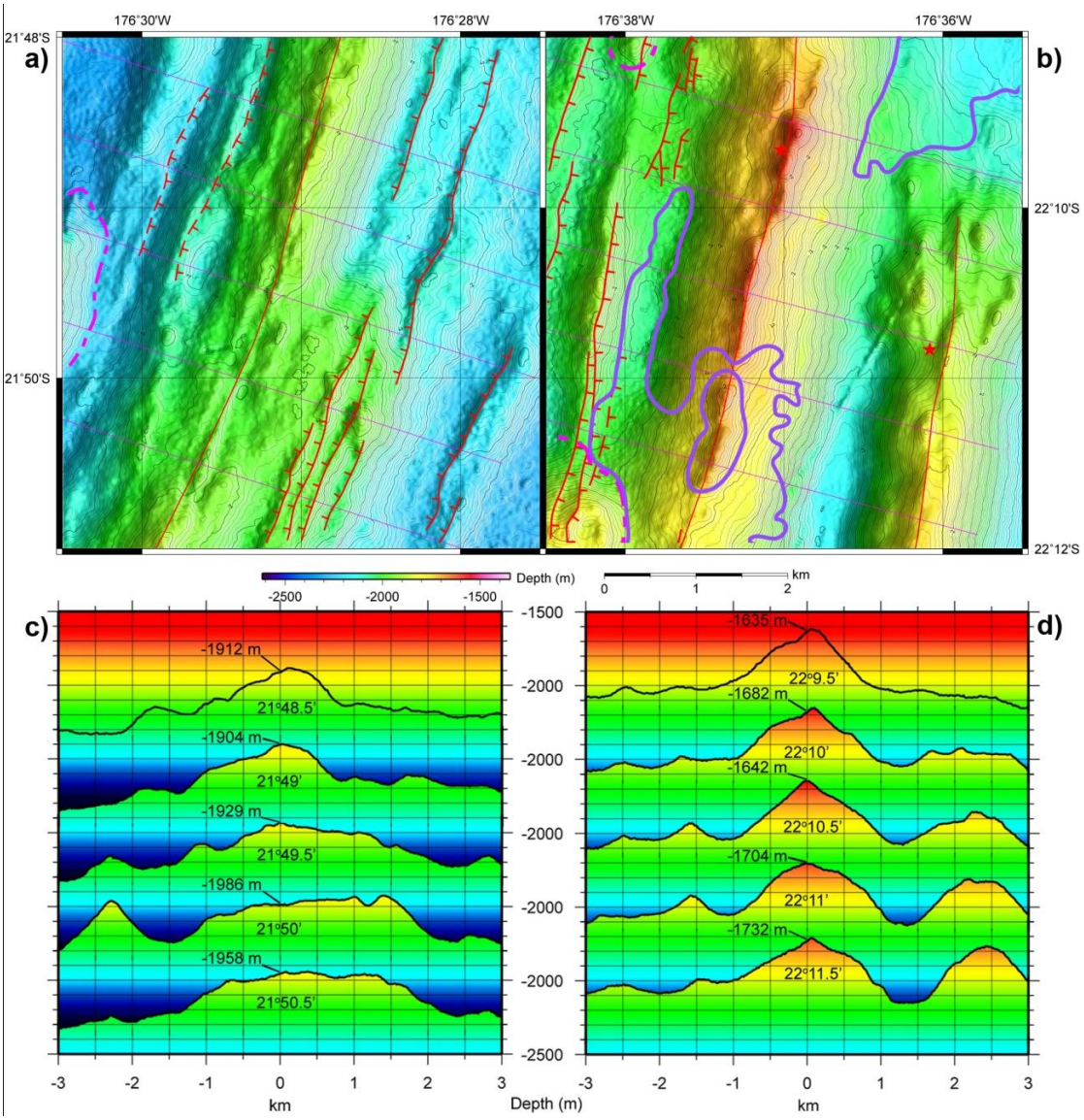

Figure 13: VFR-N focus areas, bathymetry and across-axis profiles. a) and b) EM-120 bathymetry plots (10 m cell size), and c) and d) across-axis profiles of two portions of the VFR-N, comparing the segment center (left side), where $^{206}Pb/^{204}Pb$ ratios are at a relative low, and the southern segment end (right side), where Pb ratios are relatively high [*Loock et al., 1992, Escrig et al., 2009*]. Sidescan images of these areas are in *Fig. 14*. The axis in the southern area is narrower, much higher relief, and is 200-300 m shallower than the central area, correlating with the higher Pb ratios at the southern end. Spreading axis picks are shown as solid red lines, identified hydrothermal vent sites are shown as red stars, faults are mapped as red lines with tick marks pointing in the apparent dip direction and dashed where approximate, constructional volcanic features are outlined with dashed magenta lines, recent mappable lava flows are outlined with solid purple, and mass wasting features are indicated with orange lines. [Data sources: *Goodliffe, 1995, Martinez and Taylor, 2006, Martinez et al., 2008, Escrig et al., 2009*].

from the axis. Minor volcaniclastics that appear to be erupted from the ridge axis can be seen on the ridge flanks in the IMI-120 sidescan data along one portion of the axis from ~22^{o}06'-08' S, but these could be from nearby off-axis cones as well. There are numerous off-axis cones, mostly east of the axis, which appear to be recently active based on high backscatter in the sidescan data (*Fig. 4*). Also, there is a prominent 250+ m high cone with a summit crater on the eastern flank of the axis located between ~176^{o}35-36' W and ~22^{o}05-06' S that appears to be erupting volcaniclastics, based on the texture in the sidescan data and the radial pattern on the flanks (*Fig. 12*). Based on the volcanic and morphologic changes that appear to start at ~22^{o}06' S, it is unlikely to be entirely a coincidence that also starting at ~22^{o}06' S ^{206}Pb/^{204}Pb ratios begin to climb rapidly (*Fig. 4*), staying at a relative high until the southern end of the segment, where dense sampling ends [*Escrig et al., 2009, Loock et al., 1992*]. Another interesting correlation is that the anomalously high ^{206}Pb/^{204}Pb values between 21.9^{o} S and 22.0^{o} S (*Fig. 8*) correspond with a portion of the ridge axis that appears to be anomalously shallower and narrower than the adjacent portions to the north and south, seen in *Fig. 12*. As noted in the previous section, this anomalous area lines up along the slab flow line with Volcano 4 in the Tofua arc, providing a potential explanation for this departure from the overall sinusoidal trend. It is much more difficult to explain the anomalously low values at around 21^{o}35' S, as they fall right within a local high point along the axis. Anomalies such as this emphasize the need for more data collection along this axis to confirm the correlation between ^{206}Pb/^{204}Pb ratios and ridge morphology.

4.32 Variations in faulting and hydrothermal activity (VFR-N)

The overall trend in fault length and displacement is similar to the overall along-axis trend and to what is observed along the VFR-S. Faulting is generally more abundant than along the VFR-S and occurs in an increasingly wider zone toward the north. Fault length and throws increase toward the north with increasing separation from the arc, although throws only reach a few 10's of m at most, and most faults have throws of less than 10 m. Also, faults are again

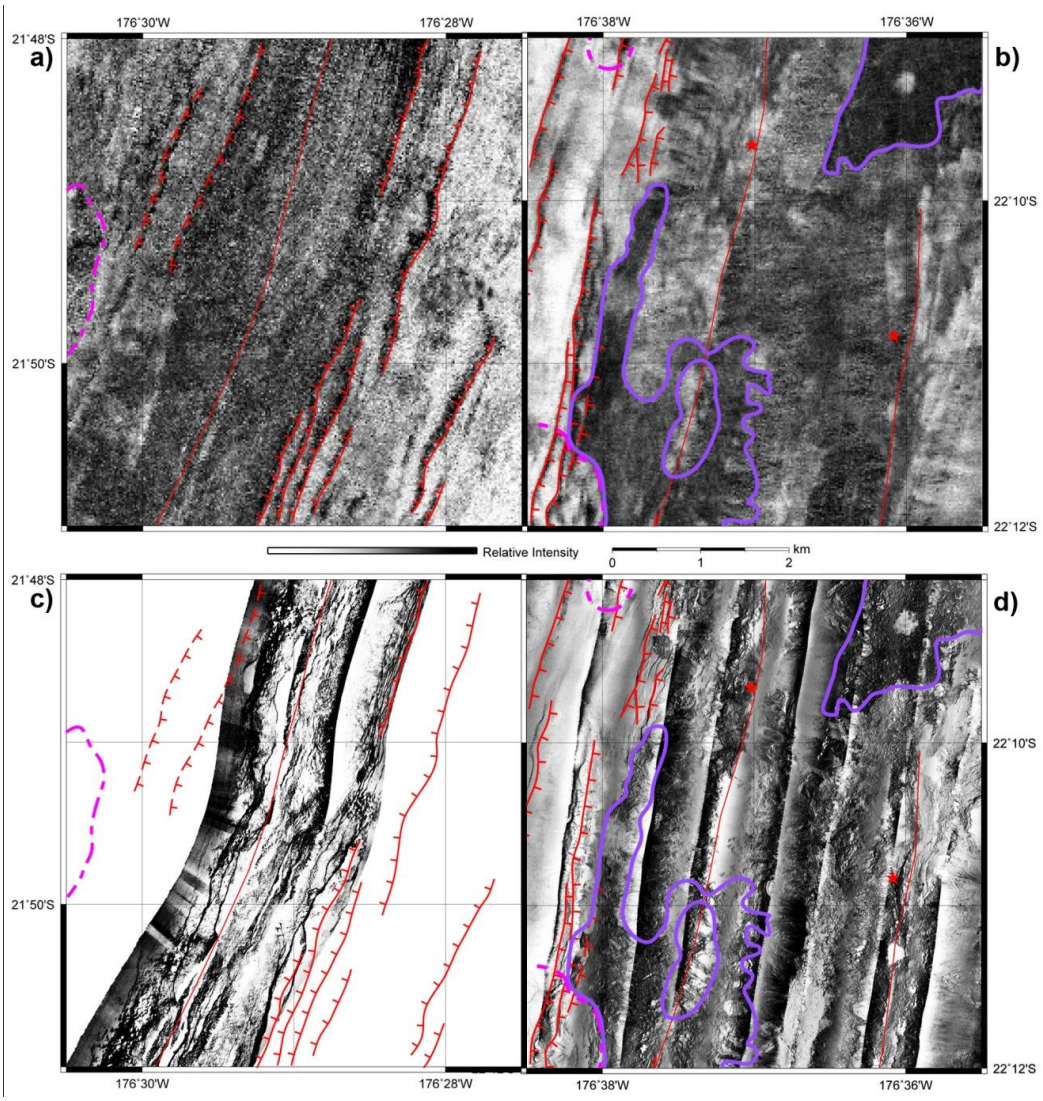

Figure 14: VFR-N focus areas, sidescan images. a) and b) EM-120 (20 m cell size) and c) and d) IMI-120 (2 m cell size) sidescan images from two portions of VFR-N, chosen to show the contrast between the segment center (left side), where $^{206}Pb/^{204}Pb$ ratios are at a relative low, and the southern segment end (right side), where $^{206}Pb/^{204}Pb$ ratios are relatively high [*Loock et al., 1992, Escrig et al., 2009*]. See *Fig. 14* for bathymetry plots and across-axis profiles. Sheet flows are more dominant and more voluminous in the southern area, while there appear to be more exposed near-axis faults and more pillow constructs along the central portion. Minor volcaniclastics may be present in the southern section, but the source is unclear. Spreading axis picks are shown as solid red lines, identified hydrothermal vent sites are shown as red stars, faults are mapped as red lines with tick marks pointing in the apparent dip direction and dashed where approximate, constructional volcanic features are outlined with dashed magenta lines, recent mappable lava flows are outlined with solid purple, and mass wasting features are indicated with orange lines. [Data sources: *Martinez and Taylor, 2006, Martinez et al., 2008*].

better exposed along the west side of the axis than the east side, similar to the trend seen along the VFR-S. This asymmetric fault exposure can be seen in the rest of the segments to the north as well. Most faults along the axis itself are relatively small and generally buried by axial lava flows. Hydrothermal activity appears to be high near the overlap zone with the VFR-S, a region where magmatism in general appears to be anomalously high [*Turner et al., 1999*], but resumes a trend of generally increasing toward the north for the rest of the segment north of the overlap zone [*Baker et al., 2006, Baker et al., 2010*]. There does not appear to be a correlation between intra-segment variations in faulting and hydrothermal activity and intra-segment variations in $^{206}Pb/^{204}Pb$ ratios. Rather, as with the rest of the ELSC and VFR, faulting and hydrothermal activity appear to be correlated with the overall first-order trends in decreasing arc influence and increasing spreading rate toward the north.

4.33 The VFR-N/S overlap zone

The overlap zone between the VFR-N and VFR-S is a region with some anomalous characteristics that should be described, as they don't quite fit within the overall pattern of variation along the rest of the segments. This zone appears to be the most magmatically robust portion of the entire system based on the shallow depths and abundant volcanism (*Fig. 15*). Axial depths range from ~-1700 m to shallower than -1600 m, whereas the shallowest portion of the axis outside of this zone is barely above -1800 m (*Figs. 9, 12*). Abundant volcaniclastics have been erupted from the VFR-S and abundant sheet flows can be seen on the flanks of the VFR-N. A continuous AMC reflector was observed under both segments in the overlap zone, and it actually appears to be widest within this zone [*Jacobs et al., 2007, Harding et al., 2000, Wiedicke and Collier, 1993*]. Looking at the arc volcanoes, there appears to be an anomalously high concentration of volcanoes with abnormally small spacing between them adjacent to the VFR (*Fig. 2*). All of these characteristics indicate that the VFR-N/S overlap zone is a region of anomalously enhanced magmatism that may require an explanation beyond simply intra-segment variations in subduction

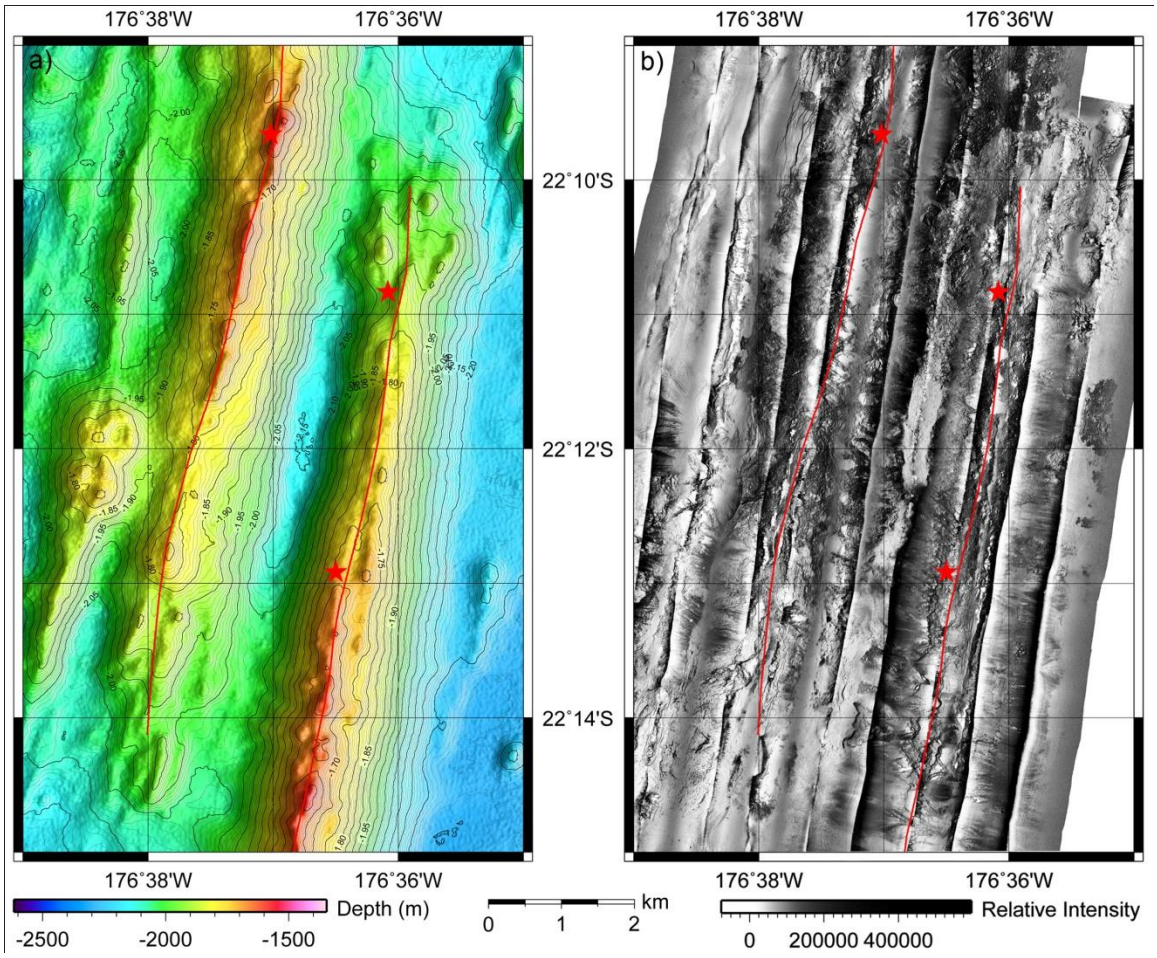

Figure 15: VFR-N/S overlap zone. a) EM-120 bathymetry (10 m cell size); b) IMI-120 sidescan (2 m cell size). This zone is the shallowest, most magmatically robust portion of the entire ELSC and VFR. The southern end of the VFR-S should be based on its closer proximity to the arc, indicating that something other than variations in subduction influence is affecting this area. [Data sources: *Goodliffe, 1995, Martinez and Taylor, 2006, Martinez et al., 2008, Escrig et al., 2009*].

influence. If variations in subduction influence were the only process affecting the axis, we would expect that the southern end of the VFR-S, in closest proximity to the arc, would be the shallowest and most magmatically robust portion of the system. A possible explanation for this could be the subduction of the Louisville Seamount Chain that projects under the VFR axis, although the effects on mantle composition and melting characteristics are not well understood at this time and this remains a speculative theory.

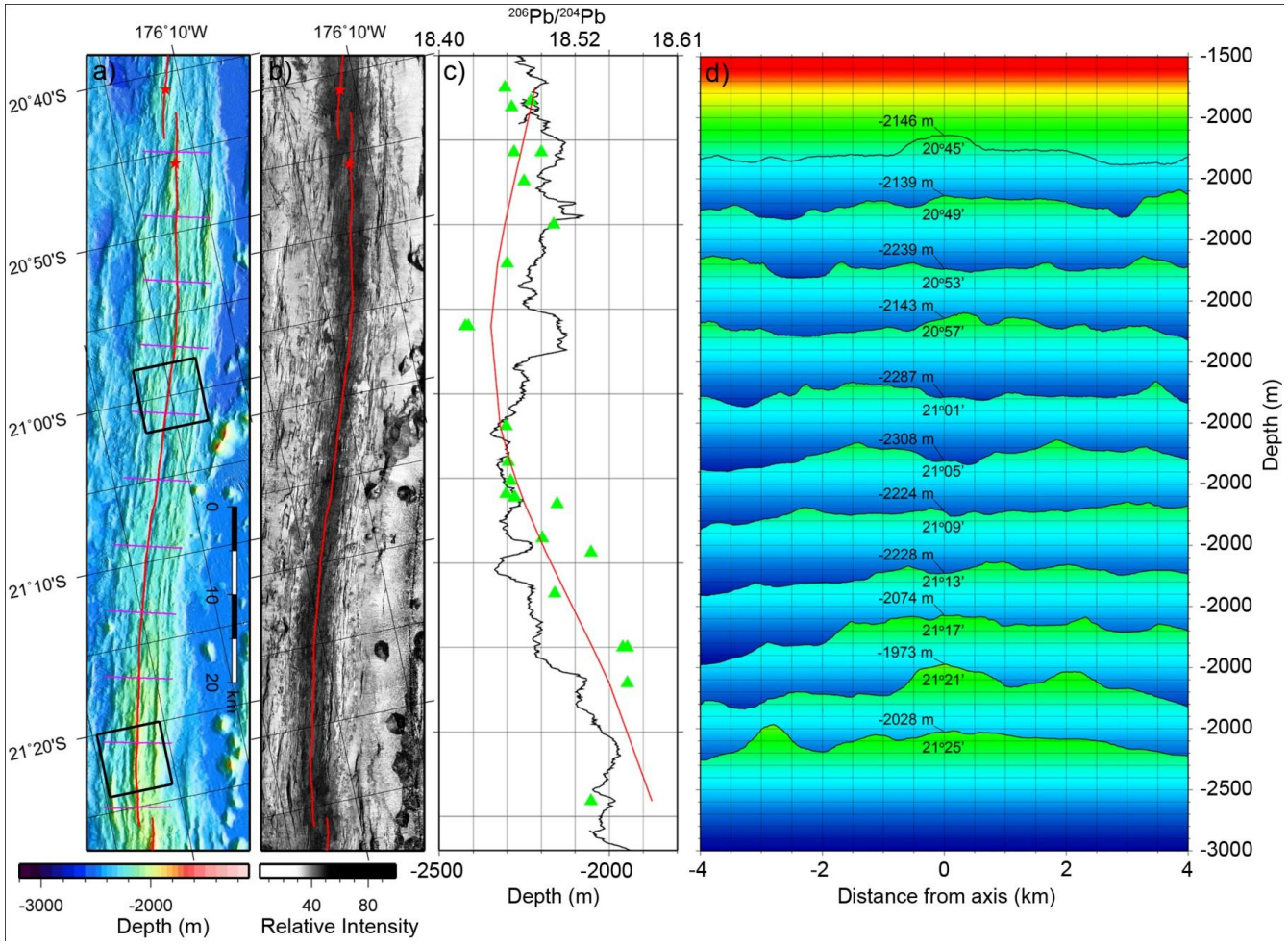

Figure 16: CELSC-S summary figure. a) EM-120 bathymetry (20 m cell size); b) EM-120 sidescan (20 m cell size); c) along-axis profile overlain with 206Pb/204Pb ratios and best fit curve; d) across-axis profiles. [Data sources: *Goodliffe, 1995, Martinez and Taylor, 2006, Martinez et al., 2008, Dunn et al., 2009, Escrig et al., 2009*].

4.4 The Central Eastern Lau Spreading Center, southern segment (CELSC-S)

The CELSC-S segment extends for ~83 km from ~21^{o}26' S to ~20^{o}42.5' S at the northern end, where it terminates into a ~1.6 km wide non-transform step-over that overlaps the CELSC-N by ~ 3 km (*Fig. 6*). The CELSC-S axis is characterized by a broad, relatively low relief axial high rising ~100-400 m above the surrounding seafloor. There is a lot more variability in on- and off-axis topography than along the VFR. The axis itself varies from a peak within the broad axial high (see across-axis profile along 21^{o}21' S in *Fig. 16*) to a small valley within the axial high (see across-axis profile along 21^{o}05' S in *Fig. 7*). The off-axis topography is similarly variable, characterized by axis-parallel constructional volcanic ridges and intervening valleys with an irregular distribution (*Fig. 6*). Some of these off-axis ridges have greater relief than the active spreading axis; the ridges extending from ~20^{o}45'-55' S ~4 km off either side of the axis are good examples (*Fig. 4a*). This morphologic variability suggests that along with a general decrease in subduction-augmented melt supply toward the north, there is also increased temporal variation in melt supply and magmatism compared to the VFR. However, the morphology and depth of the axis still show a similar cosine-like pattern of variation to the VFR-N, with relative highs near the segment ends and a relative low in the central portion. The pattern here is more subtle than along the VFR, but can also be observed in the bathymetry and profiles presented in *Figs. 6-7*. Also, the sidescan data show that there is a subtle narrowing in width and decrease in backscatter intensity of the high backscatter neo-volcanic zone toward the center of the segment, while it is relatively wider and slightly more reflective near the ends (*Fig. 6*), suggesting that there is a slight reduction in magmatism near the center. Like the VFR-N, there appears to be a correlation between the morphology and depth of the axis and the $^{206}Pb/^{204}Pb$ ratios measured in samples collected along the segment. Although there still is a cosine-like trend in the polynomial fit for the $^{206}Pb/^{204}Pb$ plot on *Fig. 8,* this correlation is weaker than along the VFR-N and all that can be said with much confidence is that the values are highest near the southern end, where axial depth is shallowest and relief is highest [*Loock et al., 1992, Escrig et*

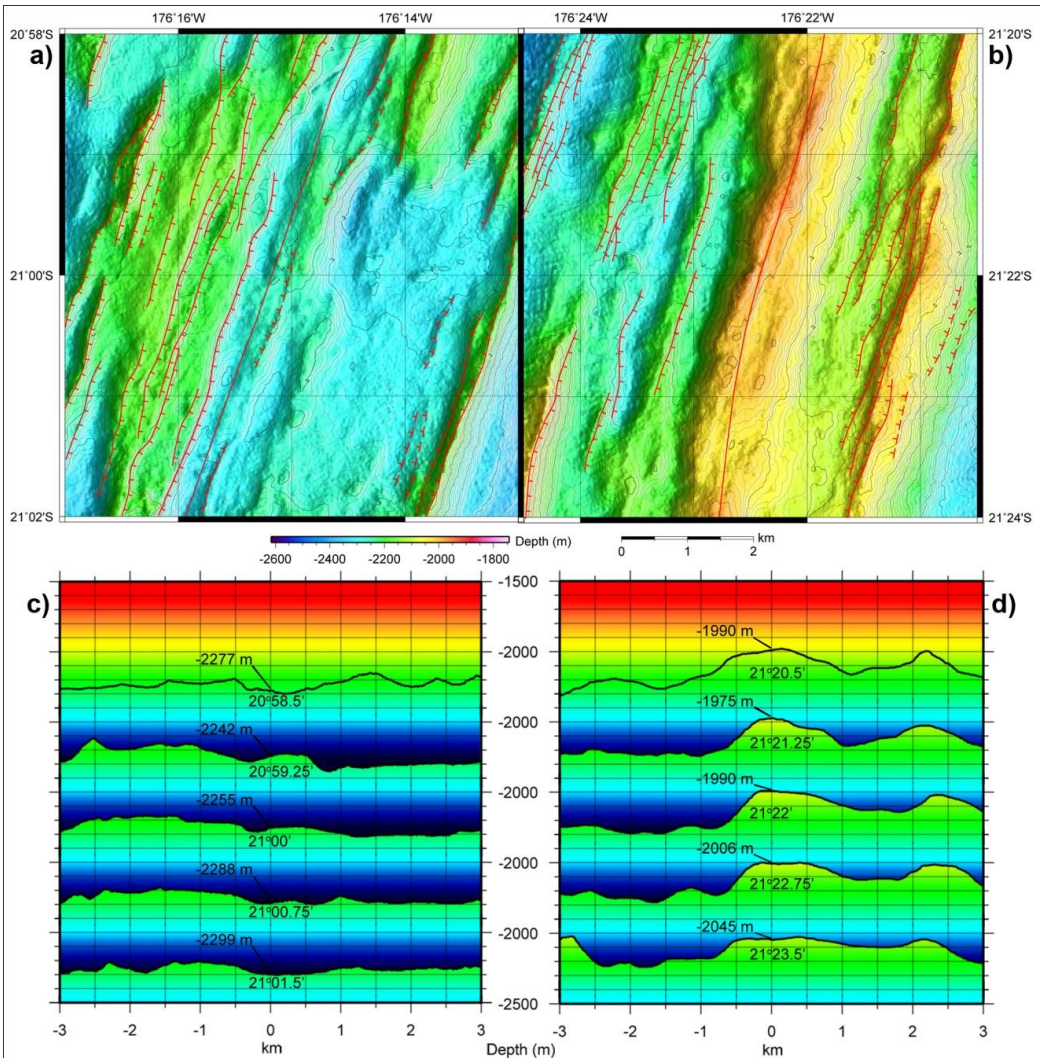

Figure 17: CELSC-S focus areas, bathymetry and across-axis profiles. a) and b) EM-120 bathymetry (20 m cell size); c) and d) across-axis profiles from two portions of the CELSC-S, chosen to show the contrast between the segment center (left side), where $^{206}Pb/^{204}Pb$ ratios are relatively low, and the southern segment end (right side), where $^{206}Pb/^{204}Pb$ ratios are relatively high [*Jenner et al., 1987, Vallier et al., 1991, Loock et al., 1992, Escrig et al., 2009*]. The southern portion, where subduction influence is highest along the CELSC-S, is over 250 m shallower on average and has a much higher relief axial volcanic ridge. The central area, where subduction influence is at its lowest along the CELSC-S, is flatter and deeper, and it lacks the axial ridge seen in the southern portion. Spreading axis picks are shown as solid red lines, identified hydrothermal vent sites are shown as red stars, faults are mapped as red lines with tick marks pointing in the apparent dip direction and dashed where approximate, constructional volcanic features are outlined with dashed magenta lines, recent mappable lava flows are outlined with solid purple, and mass wasting features are indicated with orange lines. [Data sources: *Goodliffe, 1995, Martinez and Taylor, 2006, Martinez et al., 2008, Escrig et al., 2009*].

al., 2009]. The values from samples near the northern end are also generally higher than near the center of the segment between ~21°00' and 21°10' S, where the best fit curve for the Pb values also bottoms out (*Figs. 3-4*), but the values are too close to make any robust conclusions about the correlation at this scale. It is not surprising that this correlation becomes weaker and more difficult to distinguish toward the north as subduction influence also weakens due to increasing distance between the arc and the spreading axes.

4.41 Variations in morphology and volcanism (CELSC-S)

Although the correlation with $^{206}Pb/^{204}Pb$ ratios along the CELSC-S is weaker in general, the morphology still shows a pattern of relative highs near the northern and southern ends and a relative low near the center of the segment. This can be seen in the bathymetry plot and the across-axis profiles in *Fig.* 16. *Figs. 17-18* show a more detailed view comparing a section near the center of the segment from 20°58' to 21°02' S with a section near the southern end from 21°20' to 21°24' S. The axis in the central portion has much lower relief and is over 250 m deeper on average, while the southern portion is higher relief and has a distinct ridge along the axis which rises 100 to 300 m above the surrounding seafloor. The northern end is relatively lower relief and deeper than the southern end, but still relatively shallower and higher relief than the central portion. Volcanism is dominated by a combination of sheet flows and pillow lavas along the CELSC-S. The sheet flows along the CELSC-S are smaller and cover less area than those along the VFR. This is likely due to a combination of reasons, including lower melt supply, larger near-axis faults, and less steep axial flanks. Volcaniclastics erupted from the ridge axis were not observed in the sidescan data. As seen in the sidescan images in *Fig.* 18, the high backscatter neo-volcanic zone along the axis is wider at the southern segment end compared to the center. Looking at the narrow swaths of IMI-120 sidescan data, it appears that the southern end has more abundant pillow volcanism, while there are more faults exposed along the central portion. Because the small near-axis faults are relatively easily obscured by lava flows, it is difficult to determine whether the

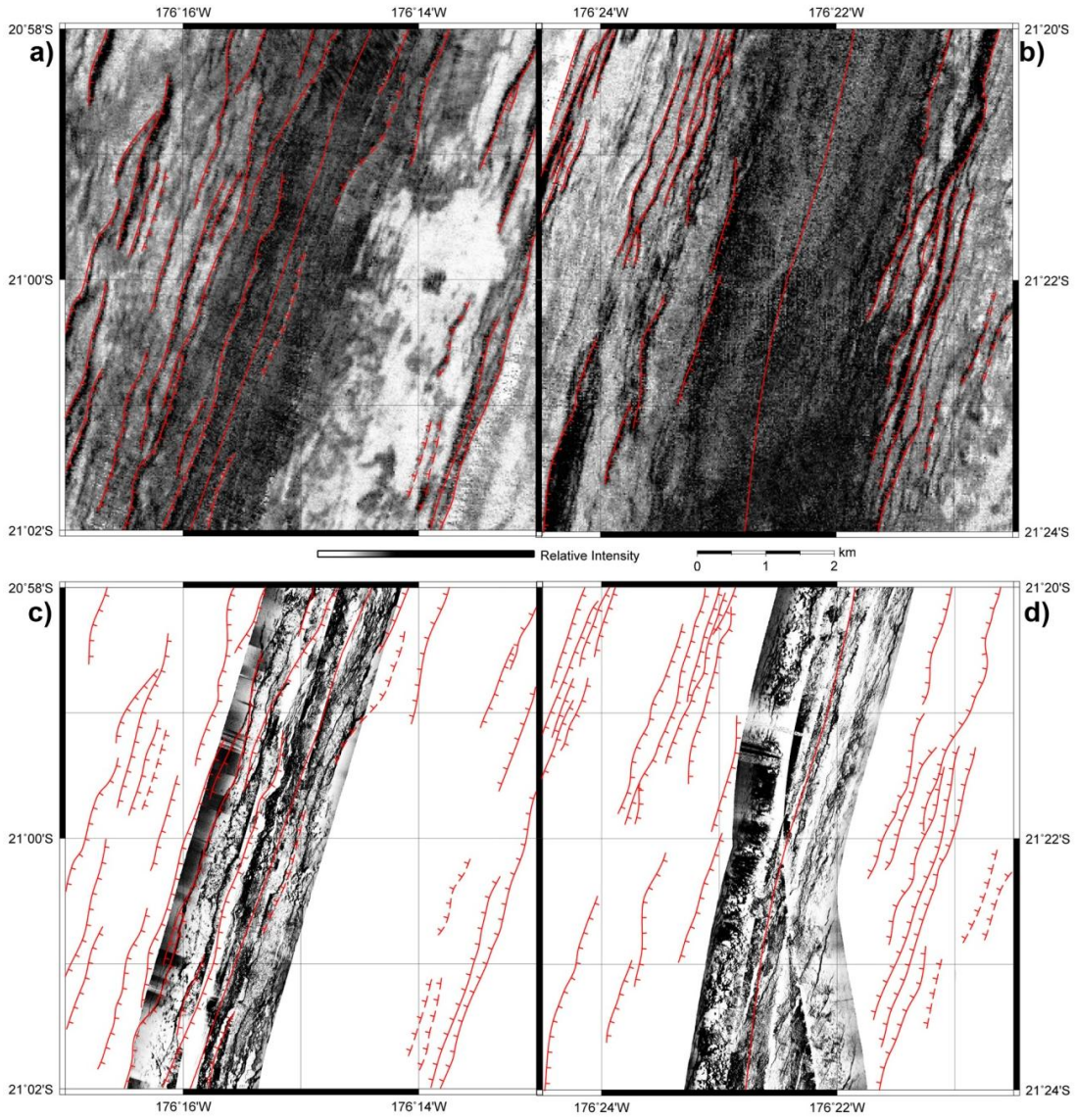

Figure 18: CELSC-S focus areas, sidescan images. a) and b) EM-120 (20 m cell size); c) and d) IMI-120 (2 m cell size) sidescan images from the central (left) and southern (right) portions of the CELSC-S, as seen in the bathymetry plots and across-axis profiles in *Fig. 17*. The high backscatter neo-volcanic zone is wider in the southern region and in the IMI-120 data there appears to be more near-axis volcanism and less exposed faulting compared to the central region. These observations are consistent with increased magmatism along the southern portion of the segment, which is to be expected where subduction influence is relatively high. Spreading axis picks are shown as solid red lines, identified hydrothermal vent sites are shown as red stars, faults are mapped as red lines with tick marks pointing in the apparent dip direction and dashed where approximate, constructional volcanic features are outlined with dashed magenta lines, recent mappable lava flows are outlined with solid purple, and mass wasting features are indicated with orange lines [Data Sources: *Martinez and Taylor, 2006, Martinez et al., 2008*].

changes in fault exposure are due to burial or whether they actually reflect an increase in the abundance of faults. These pieces of evidence support the idea that the segment ends are more magmatically robust than the center, which is to be expected where subduction input is relatively higher.

4.42 Variations in faulting and hydrothermal activity (CELSC-S)

As with both segments of the VFR, the CELSC-S generally follows the first-order along-axis trend of increasing fault abundance, length, and displacement toward the north as spreading rate increases and subduction-augmented melt supply decreases. Faults are better exposed in general than along the VFR, but off-axis fault exposure is again asymmetric, with increased exposure on the west side of the axis compared to the east side. Apparent fault throws reach over 100 m in some locations, but typically are on the order of 50 m or less. There are numerous small unmapped faults and fissures within the neo-volcanic zone as well, although they are commonly partially buried by lava flows or pillow constructs. Hydrothermal activity appears to generally increase toward the north following the overall trend, with a major spike in activity at ~20.7^{o} S, just south of the major geochemical transition zone at 20.6^{o} S and near the overlap zone with the CELSC-N, where the ABE vent field is located [*Baker et al., 2006, Baker et al., 2010*].

4.5 The Central Eastern Lau Spreading Center, northern segment (CELSC-N)

The CELSC-N segment extends for ~29 km from ~20^{o}44’ to ~20^{o}29’ S, where it terminates in a ~4.5-5 km wide and ~5 km long non-transform step-over overlapping the southern end of the NELSC-S (*Fig. 19*). The CELSC-N is currently propagating northward, shutting down the NELSC-S and leaving behind an extinct spreading center in the basin located off of the west side of the axis, which can be recognized by the low backscatter and subdued topography relative to the active CELSC-N axis (*Fig. 19*). In the longer term, the NELSC is propagating southward as the spreading system separates from the arc, “dueling” back and forth with the CELSC as it progresses. A poorly understood

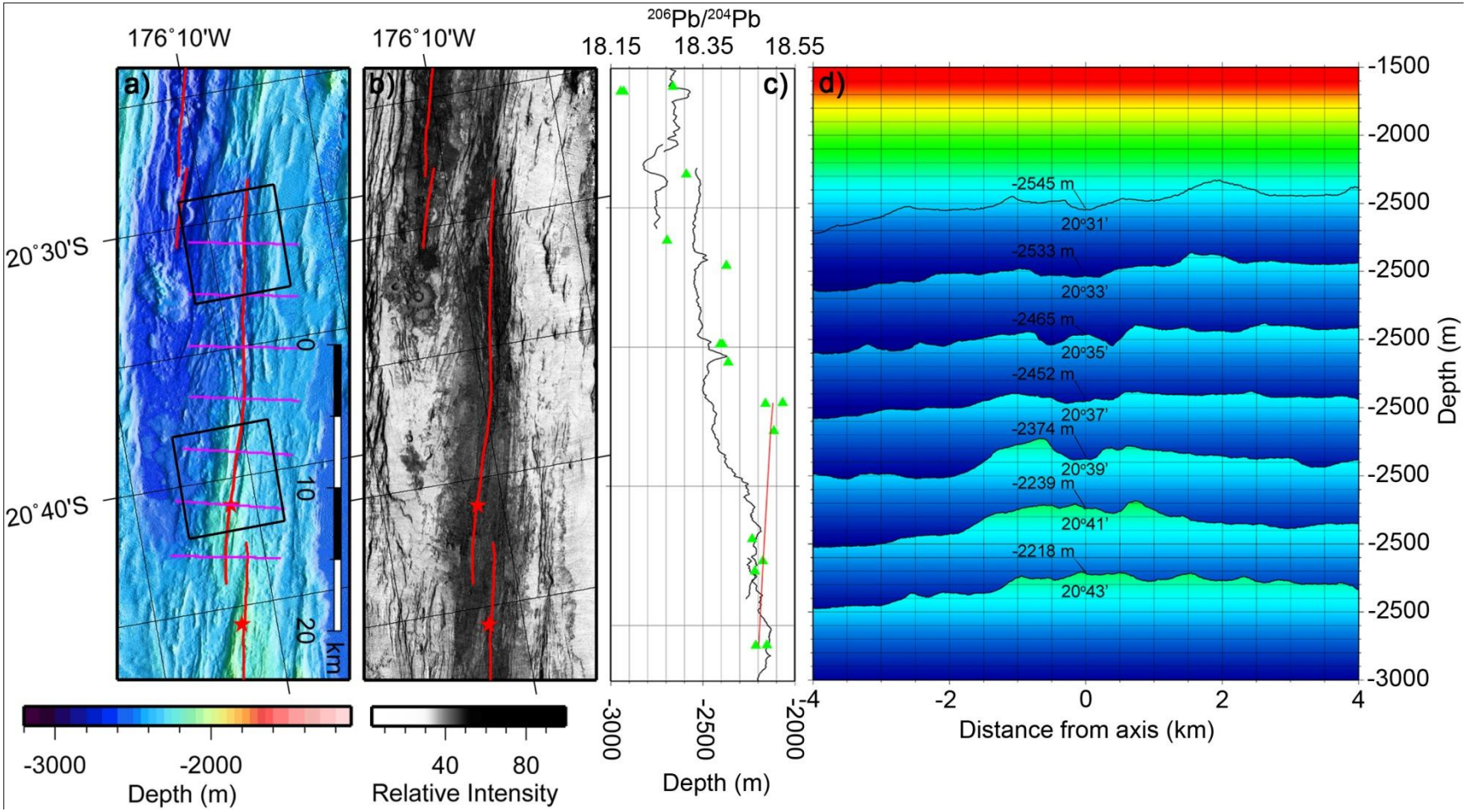

Figure 19: CELSC-N summary figure. a) EM-120 bathymetry (20 m cell size); b) EM-120 sidescan (20 m cell size); c) along-axis profile overlain with $^{206}Pb/^{204}Pb$ ratios and best fit curve; d) across-axis profiles. [Data sources: *Goodliffe, 1995, Martinez and Taylor, 2006, Martinez et al., 2008, Dunn et al., 2009, Escrig et al., 2009*].

aspect of these dueling propagators is that although the lateral offsets are small (~5 km), each axis is accreting distinctly different types and volumes of magma [*Dunn and Martinez,* 2011]. This segment is unique because it sits astride a major geochemical and geophysical change in the mantle, the nature of which is only beginning to be understood [*Escrig et al., 2009, Dunn and Martinez, 2011*]. This change occurs over a narrow transition zone around 20.6^{o} S, and can be seen in the morphology and volcanic features as well as the $^{206}Pb/^{204}Pb$ ratios of the axial lavas [*Escrig et al., 2009*]. MCS data collected in this region show that the continuous AMC reflector abruptly disappears north of this transition zone and is replaced with discontinuous thin sills of melt [*Harding et al.,* 2000, *Jacobs et al., 2007*]. *Dunn and Martinez, 2011* also observed an abrupt change in crustal seismic velocities, crustal thickness, and gravity anomalies across this

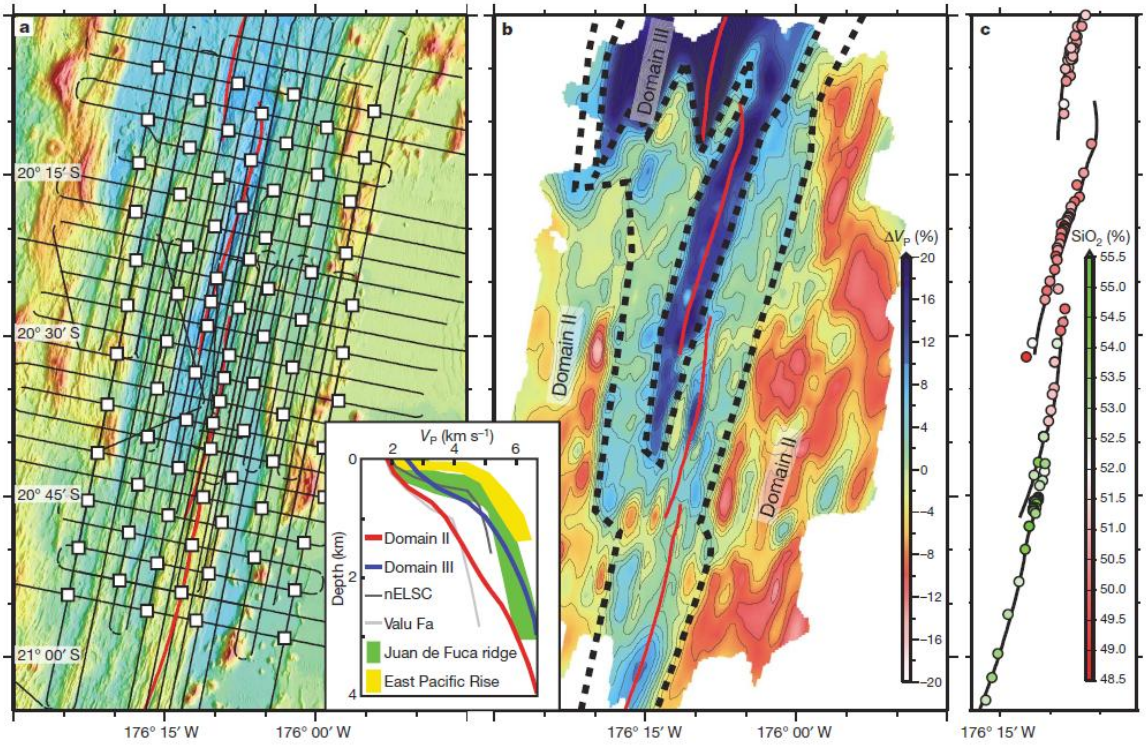

Figure 20: Summary of L-SCAN tomography results. a) bathymetry plot shows OBS layout and shot lines; b) seismic tomography results show abrupt change in p-wave velocities between Domain II and Domain III over a narrow transition zone, reflecting the sudden change in crustal thickness and porosity between the crust typical of the CELSC-S and VFR and the NELSC, spreading axes in red, domain boundaries shown as dashed black lines; c) SiO_2 plot of axial lava samples showing abrupt change from andesitic (green) to basaltic (red) lavas; inset) velocity profiles of Domain II and III compared with other ridges. [Taken from: *Dunn and Martinez, 2011*].

transition using data collected during the L-SCAN experiment (*Fig. 20*). Upper crustal seismic velocities increased abruptly from 4.0 to 5.0 ms^{-1} at 1 km depth across a zone only a few km wide, which was interpreted to be the result of a sudden change from more porous andesitic magmas to denser basaltic magmas [*Dunn and Martinez, 2011*]. Also, based on low Bouguer gravity values and isostatic calculations, the crust is ~1.9 km thinner on average north of the transition zone, which can also be accompanied by a change to denser basaltic lavas [*Dunn and Martinez, 2011*]. Unlike the CELSC-S, there is a very abrupt change in the $^{206}Pb/^{204}Pb$ ratios across the 20.6^{o} S transition zone. This can be seen best in *Fig. 8* which shows the $^{206}Pb/^{204}Pb$ ratios along the entire ELSC and VFR axis and the 20.6^{o} S transition zone is shown as a red box [*Jenner et al., 1987, Vallier et al., 1991, Loock et al., 1992, Escrig et al., 2009*]. Over a distance of less than 4 km from ~20^{o}35'-37' S the values abruptly drop by over 15% of the total range along the entire ELSC and VFR. The rest of the samples toward the north show a chaotic scatter pattern at values much lower than along the rest of the axis toward the south and no longer have any kind of discernable trend. *Figs. 21-22* show detailed bathymetry and sidescan plots, as well as across-axis profiles comparing two regions north and south of the transition zone in order to highlight the abrupt changes in the geologic characteristics of the CELSC-N axis.

4.51 Variations in morphology and volcanism (CELSC-N)

The abrupt change in mantle chemistry that occurs across the 20.6^{o} S transition zone corresponds with a similarly abrupt change in axial morphology that is easily observed in the bathymetry plots and across-axis profiles in *Fig. 6.* South of the transition zone (*Figs. 16-17, right side*), the axis is characterized by an inflated axial high with an average depth of around -2200 m, rising 100 to 300 m above the surrounding seafloor. North of the transition zone (*Figs. 16-17, left side*), the axis abruptly dives down to depths below -2500 m and the morphology is characterized by a shallow valley within an axial high with much lower relief overall. The portion of the axis from ~20^{o}40' S to ~20^{o}38' S appears to be actively crossing the geochemical transition zone. Over a distance of ~3-4 km,

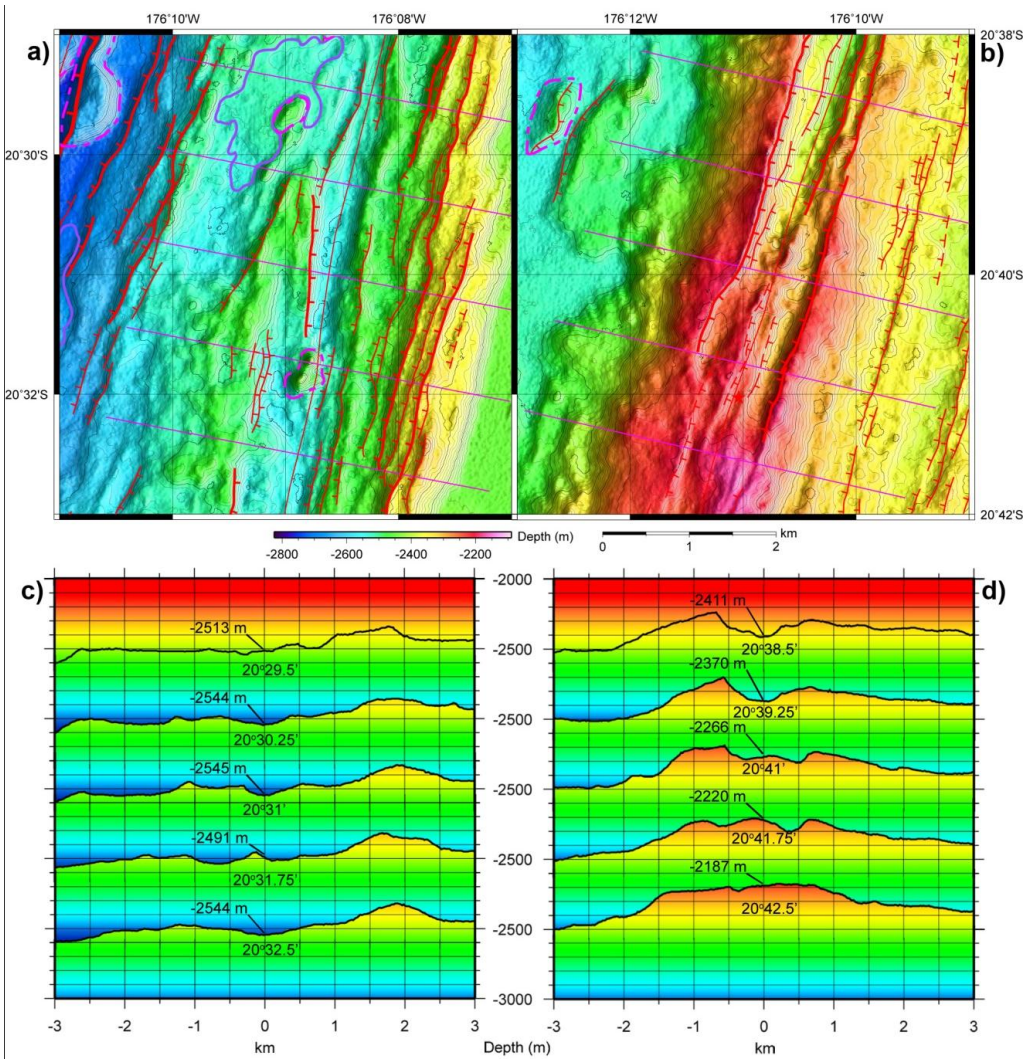

Figure 21: CELSC-N focus areas, bathymetry and across-axis profiles. a) and b) EM-120 bathymetry plots (10 m cell size); c) and d) across-axis profiles of a portion, chosen to show the abrupt changes that occur across the 20.6^{o} S transition zone, where $^{206}Pb/^{204}Pb$ ratios abruptly decrease [*Escrig et al., 2009*]. See *Fig. 22* for sidescan imagery of the same regions. There are abrupt changes in mantle properties across this transition, which are expressed in the morphology and depth of the axis, crustal thickness and density, and magmatism. The northern portion is characterized by a shallow axial valley within a very low relief, broad axial high while the southern portion is characterized by a higher relief axial high that is over 300 m shallower on average. Spreading axis picks are shown as solid red lines, identified hydrothermal vent sites are shown as red stars, faults are mapped as red lines with tick marks pointing in the apparent dip direction and dashed where approximate, constructional volcanic features are outlined with dashed magenta lines, recent mappable lava flows are outlined with solid purple, and mass wasting features are indicated with orange lines. [Data sources: *Goodliffe, 1995, Martinez and Taylor, 2006, Martinez et al., 2008, Dunn et al., 2009, Escrig et al., 2009*].

the axis changes from a small axial ridge around -2250 m depth to a narrow fault-bounded valley reaching depths of over -2450 m (*Figs. 16-17, right side*). Variability in off-axis topography, and by proxy temporal variation in melt supply, is difficult to evaluate for the CELSC-N because it is still relatively young and in the process of propagating northward, so there has only been a narrow zone of crust (< 5 km) accreted along this segment. These changes in morphology and axial depth indicate that the southern portion of the segment is more magmatically robust than the northern portion, suggesting that one of the effects across the transition zone is an overall decrease in melt supply. The dominant style of volcanism along the entire segment is pillow lavas, although sheet flow texture is visible in some locations, especially south of the transition zone. The neo-volcanic zone is generally widest near the southern end, narrowing toward the center of the segment and then widening slightly again near the northern end. Overall, the evidence strongly suggests that these abrupt changes in ridge characteristics are the direct expression of abrupt changes in the nature of the underlying mantle [*Dunn and Martinez, 2011*].

4.52 Variations in faulting and hydrothermal activity (CELSC-N)

Faulting generally increases in abundance toward the north, especially within the neo-volcanic zone, but trends in fault length and displacement depart from those seen in the segments toward the south. This likely has to do with the abrupt change in crustal thickness and density across the 20.6^{o} S transition, plus the relatively short length and young age of this segment makes it more difficult to observe a distinct trend in faulting. If you look right around the active spreading axis in the northern portion, there are numerous small faults and fissures with throws on the order of a few m within the neo-volcanic zone that are not mapped (*Figs. 21-22, left side*). Larger faults (10's of m throws) are only observed off-axis, especially to the east, where they are exposed on the west-facing flank of what appears to be a split axial ridge formed at a previous now-extinct spreading center. In the southern portion (*Figs. 21-22, right side*) , there is an observable decrease in the number of faults within the neo-volcanic zone,

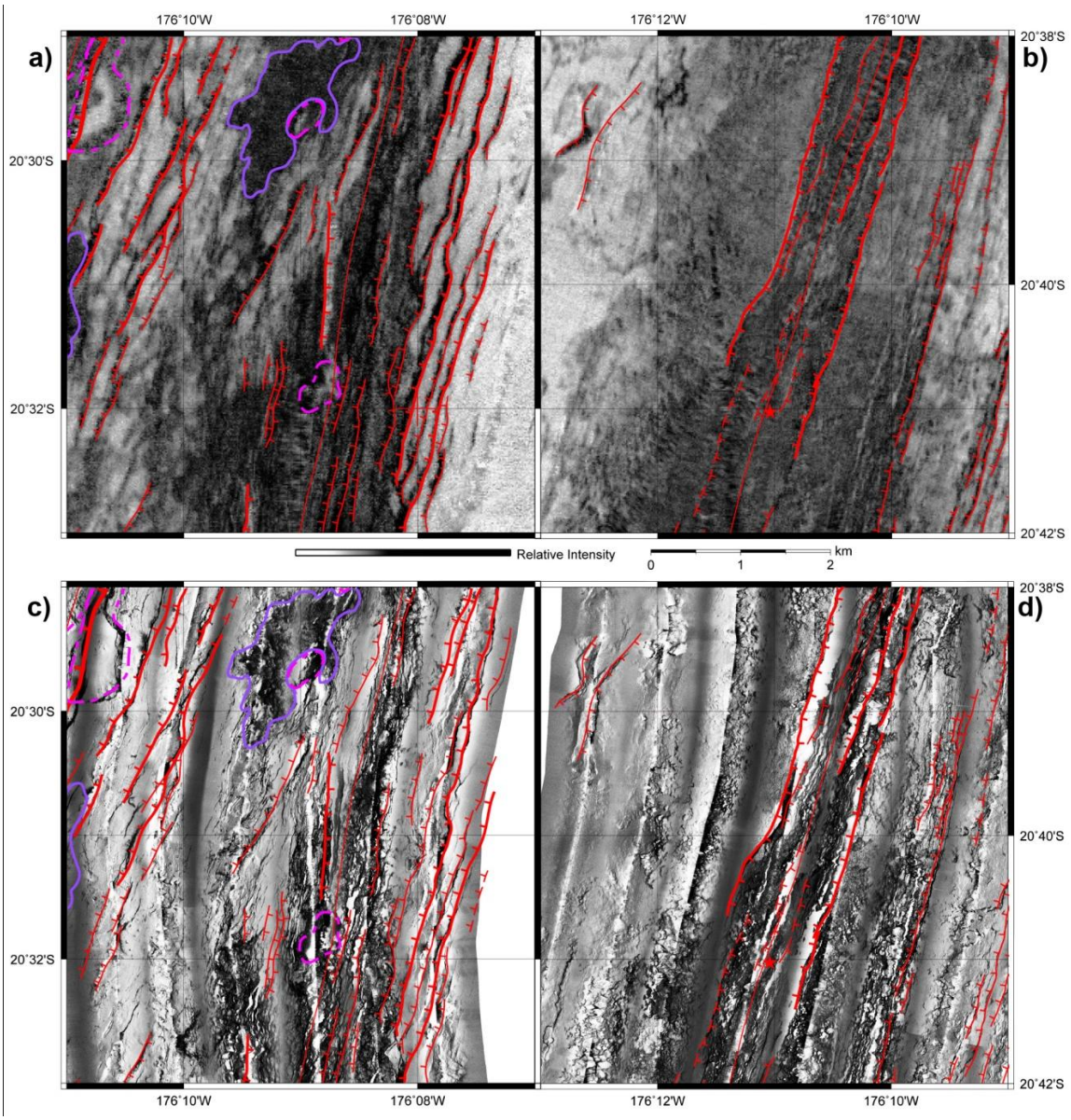

Figure 22: CELSC-N focus areas, sidescan images. a) and b) EM-120 (20 m cell size); c) and d) IMI-120 (2 m cell size) sidescan images, located north (left side) and south (right side) of the 20.6^{o} S transition zone. See *Fig. 21* for corresponding bathymetry plots and axial profiles. It appears that the southern region is more magmatically robust overall, based on the increased neo-volcanic zone width and increased abundance of pillow lavas as well as the morphologic and axial depth changes seen in *Fig. 21*. Spreading axis picks are shown as solid red lines, identified hydrothermal vent sites are shown as red stars, faults are mapped as red lines with tick marks pointing in the apparent dip direction and dashed where approximate, constructional volcanic features are outlined with dashed magenta lines, recent mappable lava flows are outlined with solid purple, and mass wasting features are indicated with orange lines [Data Sources: *Martinez and Taylor, 2006, Martinez et al., 2008*].

but there are large (up to ~90 m throws) axis-bounding faults which begin to form around 20°42' S, increasing in length and throw toward the center of the segment as the axis crosses the mantle transition zone. These faults span the portion of the segment that appears to be actively crossing the transition zone. Throws are most likely augmented by the sudden decrease in melt supply and crustal thickness, as well as the change in crustal composition and increased density. Hydrothermal activity along the CELSC-N follows the same pattern as the rest of the characteristics, showing an abrupt change across the transition zone. Plume incidence is anomalously high from the southern segment end to ~20°38' S, where the segment appears to be most magmatically robust and the only identified vent site, Tahi Moana 1, is located [*Baker et al., 2006, Baker et al., 2010, Nautilus Minerals, Inc., 2009*]. North of ~20°38' S, hydrothermal activity abruptly drops, nearly disappearing altogether along the northern portion of the segment [*Baker et al., 2006, Baker et al., 2010*], before resuming along the NELSC-S. It appears that along this segment, the abrupt changes in the mantle locally dominate the overall along-axis trend of increasing plume incidence toward the north.

4.6 The Northern Eastern Lau Spreading Center, southern segment (NELSC-S)

The NELSC-S segment extends for ~39 km from ~20°31' to ~20°11' S, where it terminates in a ~6 km wide and ~3.5 km long non-transform step-over with the NELSC-N (*Figs. 8-9*). This segment is being overtaken and shut down at the north and south ends by the propagating tips of the NELSC-N and the CELSC-N, respectively. Based on the extent of the extinct basins along the north and south ends of this segment, it initially extended from ~20°02' to ~20°42' S, about twice its current length (*Fig. 8*). *Fig. 8* shows bathymetry and sidescan plots of the entire NELSC axis, along with an along-axis profile, a plot of $^{206}Pb/^{204}Pb$ ratios from samples within the NELSC, and across-axis profiles along both segments. Along the NELSC-S, the low, broad axial high that characterizes the majority of the CELSC is replaced by a relatively flat axis within a deep axial valley. This valley is bounded on either side by one or two corresponding pairs

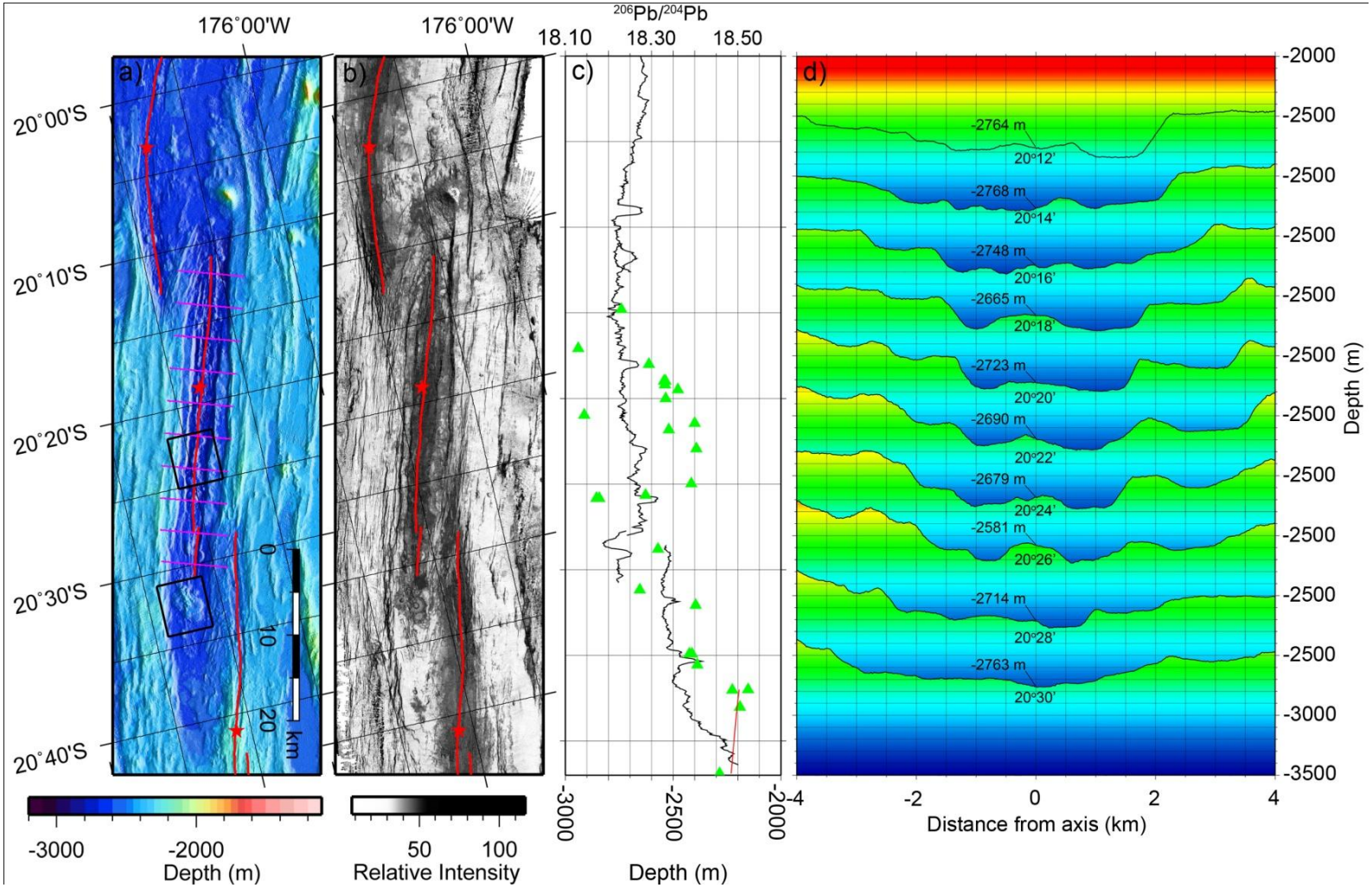

Figure 23: NELSC-S summary figure. a) EM-120 bathymetry (20 m cell size); b) EM-120 sidescan (20 m cell size); along-axis profile overlain with $^{206}Pb/^{204}Pb$ ratios and the best fit curve; d) across-axis profiles. [Data sources: *Goodliffe, 1995, Martinez and Taylor, 2006, Martinez et al., 2008, Dunn et al., 2009, Escrig et al., 2009*].

of major faults which take up the majority of the ~400 m of apparent displacement. The axis itself is similar in character to the CELSC-N north of the 20.6^{o} S transition zone, but the NELSC-S has more constructional volcanic features along the axis. This segment lacks an obvious along-axis pattern in morphology or axial depth beyond gradually getting ~100 m deeper on average from south to north, and the geologic characteristics don't change drastically within the active portion of the segment. As mentioned in the CELSC-N description, $^{206}Pb/^{204}Pb$ ratios along this segment are distributed in a chaotic manner and lack a discernable trend, but are all uniformly low relative to the rest of the axis to the south (*Figs. 8, 23*) [*Escrig et al., 2009*].

4.61 Variations in morphology and volcanism (NELSC-S)

The NELSC-S shows very little morphologic variability within the active portion of the segment compared to the segments to the south. *Figs. 24-25* show detailed sidescan and bathymetry plots comparing a typical region within the active portion of the axis with a region to the south within the extinct portion of the axis. The large valley-bounding faults act as a natural barrier to any lava flows along the axis, creating a very sharp boundary around the neo-volcanic zone. The near-axis seafloor is mostly flat in overall relief, but along with small pillow mounds and domes, there are distinct constructional volcanic features along much of the length of the axis unlike volcanic features seen along any of the segments to the south. These features tend to be larger toward the southern end of the segment, but otherwise there are no strong morphologic trends. The bathymetry plots on the left side of *Fig. 24* show some particularly large examples of these features located near the southern end of the active portion of the axis. They are characterized by relatively flat tops and steep sides, with relief of up to 150 m above the surrounding seafloor. Looking at the IMI-120 sidescan data in *Fig. 25d*, we can see that these features appear to be covered with pillows and small domes, which means they would most likely be classified as relatively large pillow mounds. Another unique volcanic feature can be seen along the extinct portion of the axis to the south (*Fig. 24-25, right side*). This

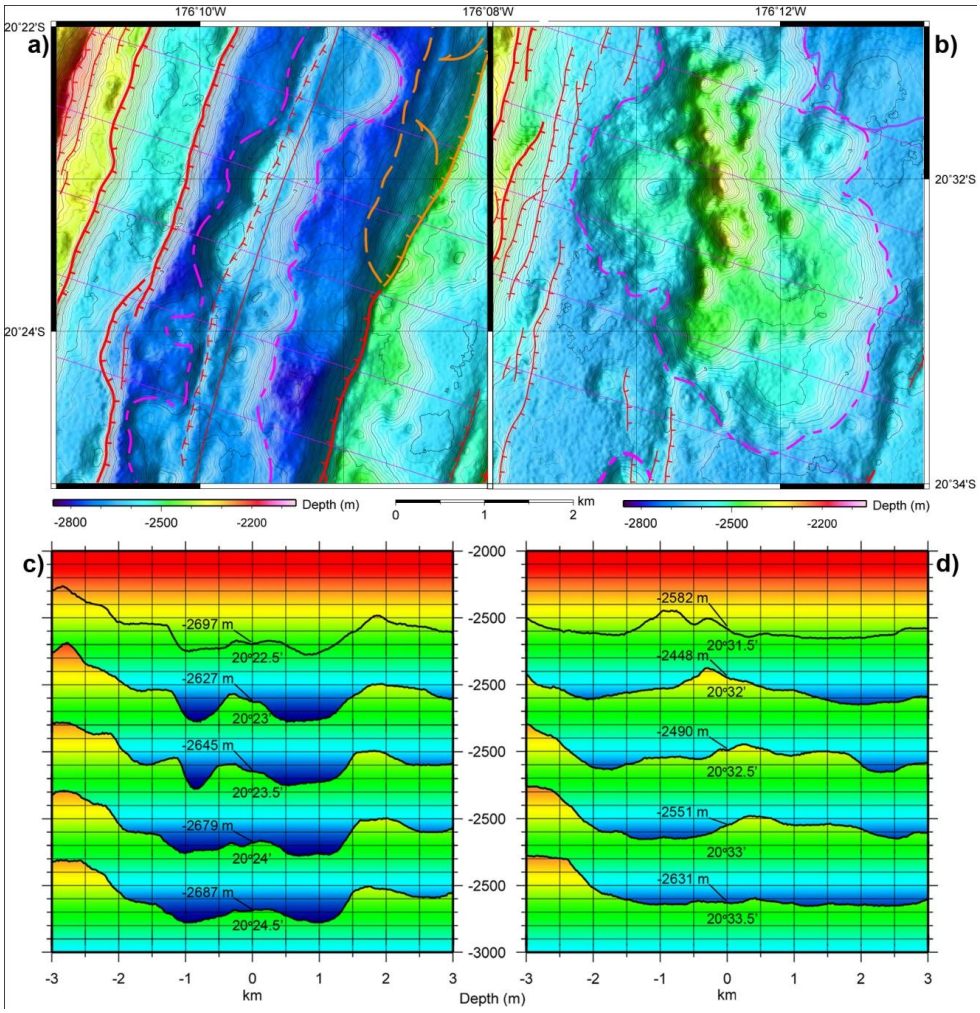

Figure 24: NELSC-S focus areas, bathymetry and across-axis profiles. a) and b) EM-120 bathymetry plots (20 m cell size); c) and d) across-axis profiles from two portions of the NELSC-S, chosen to show two contrasting examples of near-axis morphology and volcanic structures. See *Fig. 25* for corresponding sidescan images. The northern area (left side) is an example of the fault-bounded axial valley morphology that is typical of the active portion of the NELSC-S. Note the large 200 m+ apparent throws of the faults on either side of the axis, and the flat-topped, steep-sided pillow mounds along the axis that are common along this segment. The southern area (right side) shows an extinct portion of the axis below the southern tip of the segment. Note the large cluster of volcanic mounds, which are interpreted to have formed from the last of the melt under the dying axis. Spreading axis picks are shown as solid red lines and identified hydrothermal vent sites are shown as red stars. Mapped faults are indicated with red lines with tick marks pointing down-dip and dashed where approximate, constructional volcanic features are outlined with a dashed magenta line, recent mappable lava flows are outlined in solid purple, and mass wasting features are indicated with orange lines. [Data sources: *Goodliffe, 1995, Martinez and Taylor, 2006, Martinez et al., 2008, Dunn et al., 2009, Escrig et al., 2009*].

feature appears to have been constructed in at least two stages based on the morphology. The first stage is a cluster of 5 to 6 pillow mounds with a similar morphology to the flat-topped pillow mounds toward the north. Depressions that appear to be collapsed summit calderas can also be seen on the two largest mounds (*Fig. 24-25, right side*). The second stage is built on top of the first and is characterized by a linear ridge with steep cones along the crest, aligned at an oblique orientation relative to the axis. This feature is interpreted to represent a "last gasp" of volcanism as the axis ceased spreading, fed by the residual and likely strongly differentiated magmas remaining in the crustal magma chamber under the axis. It's possible that the prominent conical feature and smaller volcanic constructs that can be seen in *Fig. 23* located between ~20^{o}04'-09' S and ~176^{o}02'-05' W is another example of the "last gasp" of the northern end of the segment as it was shut down. Sampling of these features would be necessary to evaluate this interpretation and determine the origin of these features.

4.62 Variations in faulting and hydrothermal activity (NELSC-S)

Faulting does not vary much along the active portion of the NELSC-S. In the extinct portions to the north and south, the faults gradually fade away, succumbing to erosion and burial by pelagic and volcaniclastic sediments. Most of the apparent displacement of ~400 m from the base of the axial valley to the elevated crust outside the valley is taken up by the major axis-bounding faults. The largest of these faults, with an apparent throw of up to 300 m, exists near the north end of the segment on the east side of the axis from ~22^{o}10-15' S and between ~176^{o}04-05' W (*Fig. 8*), although ~100 to 200 m is a more typical range. In this location, there is only one major fault taking up the displacement on this side of the axis, resulting in an abnormally large throw on the fault. Moving south along the east side of the axis, a new fault initiates closer to the axis at around 20^{o}15' S, growing toward the south and causing the total apparent displacement to be split between two major faults, as is typical of the entire west side of the axis. There are abundant smaller faults within the elevated off-axis crust which

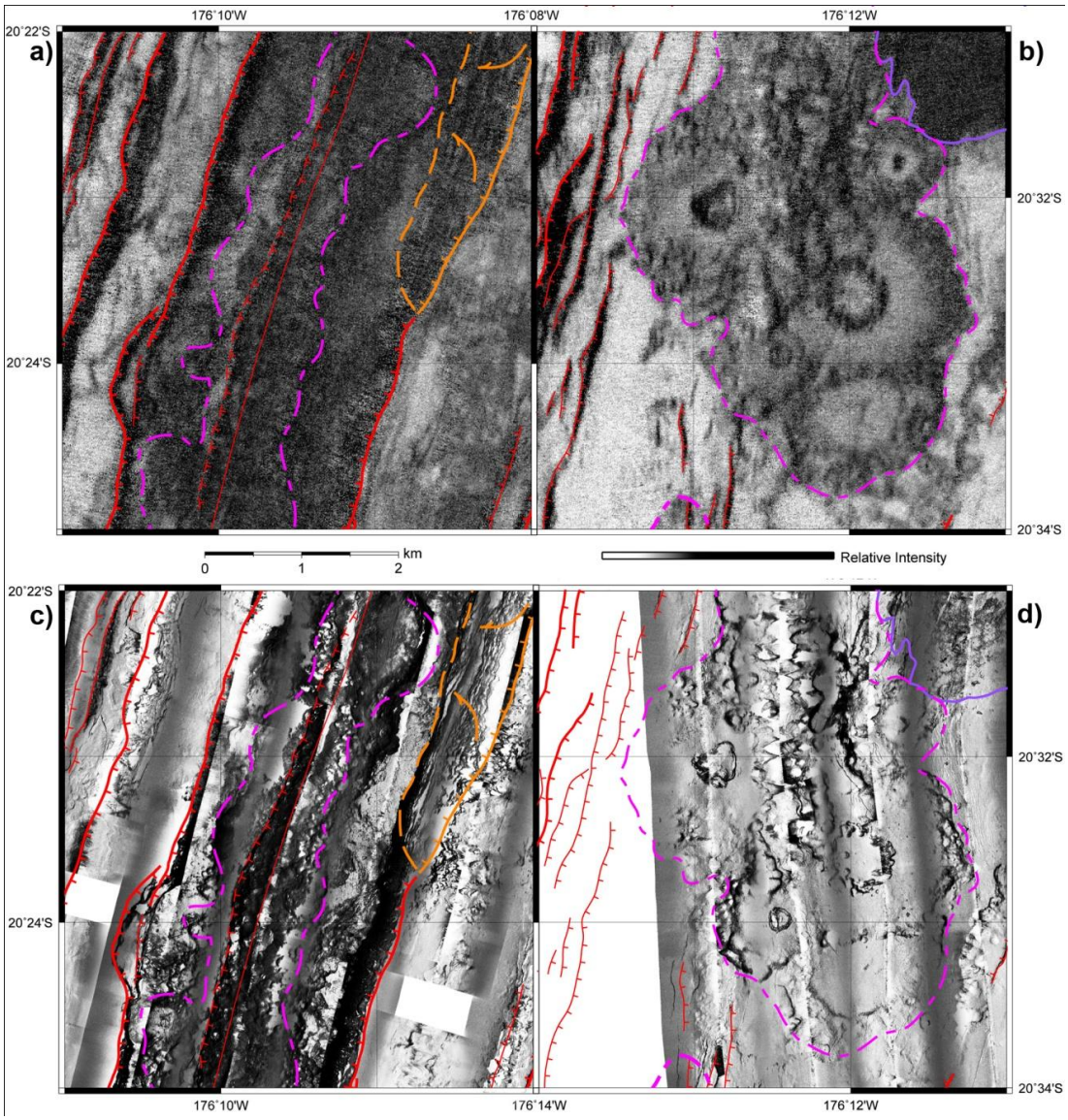

Figure 25: NELSC-S focus areas, sidescan images. a) and b) EM-120 (20 m cell size); c) and d) IMI-120 (2 m cell size) sidescan images from two portions of the NELSC-S, chosen to show two contrasting examples of near-axis morphology and volcanic structures. See *Fig. 24* for corresponding bathymetry plots and profiles from each of these areas. The northern area (left side) is an example of the fault-bounded axial valley morphology that is typical of most of the length of the NELSC-S. The lower backscatter intensity and the sediment cover visible in the IMI-120 image confirm that the southern area is extinct. Spreading axis picks are shown as solid red lines and identified hydrothermal vent sites are shown as red stars. Mapped faults are indicated with red lines with tick marks pointing down-dip and dashed where approximate, constructional volcanic features are outlined with a dashed magenta line, recent mappable lava flows are outlined in solid purple, and mass wasting features are indicated with orange lines. [Data sources: *Martinez and Taylor, 2006, Martinez et al., 2008*].

show the same pattern of better exposure on the west side of the axis that was seen along the CELSC and VFR. These faults are similar in length and throw to the faults along the CELSC-S, which makes sense because the elevated off-axis crust looks similar to the crust accreting along the CELSC-S right now. Based on the IMI-120 sidescan data along this segment, faults within the neo-volcanic zone appear to be less abundant, longer, and spaced further apart than those along the CELSC. This could be attributed to burial by lava flows and pillow mounds, but it could also be attributed to the increased density and strength of the crust forming along the NELSC compared to the CELSC. Hydrothermal activity is concentrated primarily at one vent field, Tow Cam, within a few 100 m of the axis near the center of the segment, and does not vary with any discernable pattern along the length of the segment. Even though the AMC reflector largely disappears under this segment, hydrothermal activity is still abundant here overall [*Harding et al., 2000, Baker et al., 2006, Baker et al., 2010, Jacobs et al., 2007*].

4.7 The Northern Eastern Lau Spreading Center, northern segment (NELSC-N)

The NELSC-N segment extends for ~97 km from ~20^{o}12.5' S to the northern end of the ELSC at ~19^{o}20' (*Fig. 26*) where it terminates and activity jumps ~25 km westward to the Intermediate Lau Spreading Center, which acts as a short relay segment between the ELSC and the CLSC. The CLSC is propagating southward, taking up the extension along the NELSC-N and shutting it down at the north end as it propagates further south (*Fig. 1*). The overall morphology of this segment is characterized by a mostly flat axis similar to the NELSC-S and the northern portion of the CELSC-N, situated within relatively flat crust that extends for at least 15 km to the east and west. In the along-axis and across-axis profiles in *Fig. 26*, a trend of decreasing axial depth from the southern end to ~19^{o}41' S can be observed, with average depth changing from ~-2650 m to ~-2550 m. North of ~19^{o}41' S, axial depth dives down to ~-3000 m before the segment ends. Not much can be said about correlations between ^{206}Pb/^{204}Pb ratios and axial characteristics because there are only 3 samples

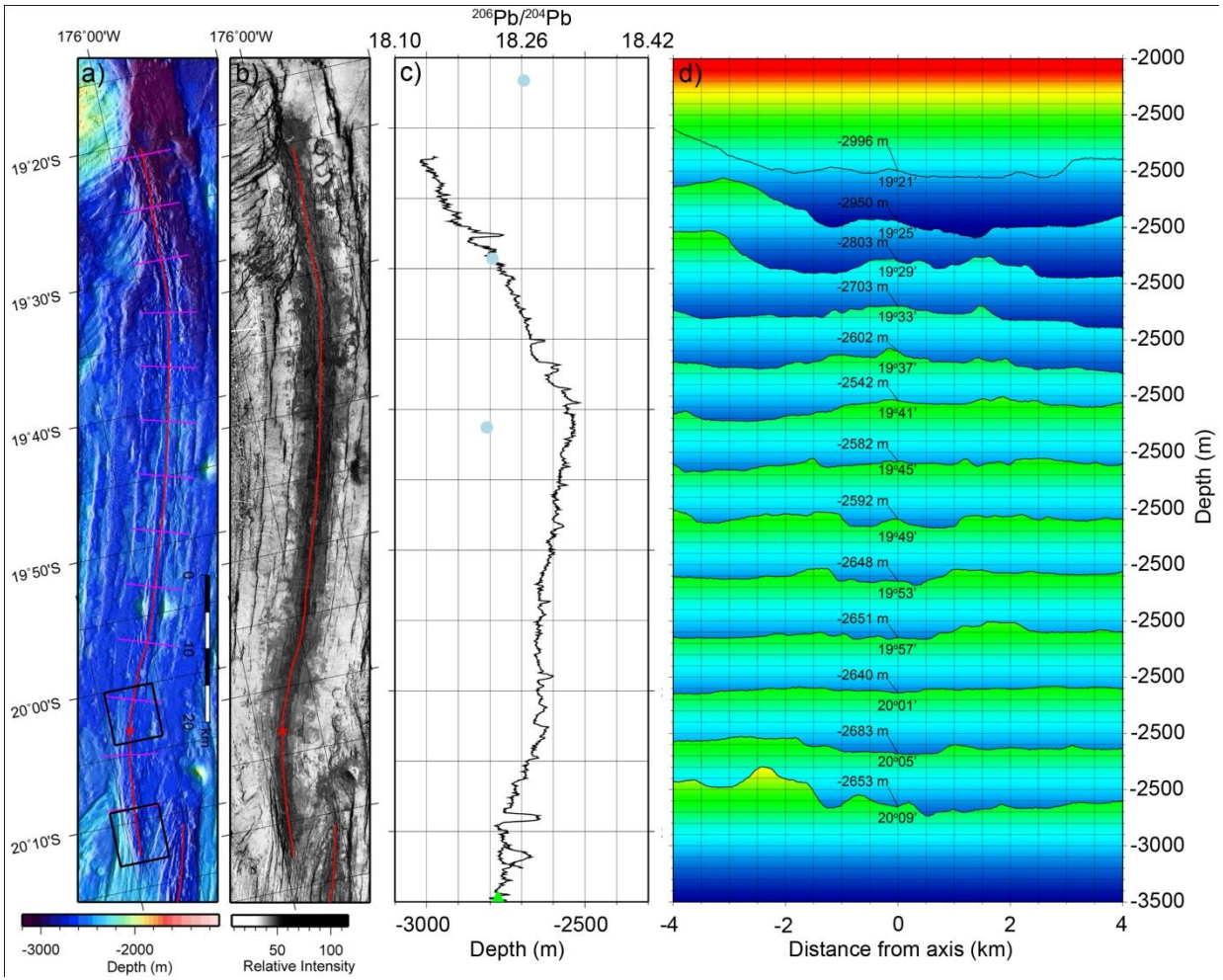

Figure 26: NELSC-N summary figure. a) EM-120 bathymetry (20 m cell size); b) EM-120 sidescan (20 m cell size); c) along-axis profile overlain with $^{206}Pb/^{204}Pb$ ratios; d) across-axis profiles. [Data sources: *Goodliffe, 1995, Peate et al., 2001, Martinez and Taylor, 2006, Martinez et al., 2008, Dunn et al., 2009, Escrig et al., 2009*].

along the entire segment, all within the lower half of the range of values along the NELSC-S. However, it is not unreasonable to assume that we would see a similar pattern of scattered low values like we see along the NELSC-S if more samples were collected. The NELSC-N displays the long-term effects of the abrupt changes in mantle properties along the 20.6^{o} S transition zone. The extent of flat off-axis crust demonstrates that this segment has been spreading in a similar mode for a long period of time. This supports the idea that the abrupt changes seen along the 20.6^{o} S transition zone are not simply due to a temporary drop in melt supply or localized mantle heterogeneity, but rather are reflecting an abrupt and permanent change in mantle properties.

4.71 Variations in morphology and volcanism (NELSC-N)

Beyond the trend in axial depth discussed in the previous section, variations in morphology and volcanism are generally subtle along the NELSC-N. *Figs. 22-23* show bathymetry and sidescan plots comparing a typical section of the axis (left side of *figs.*) to a section of the axis near the southern end (right side) where it is propagating into thicker crust. Constructional volcanic features along the axis become more abundant and prominent toward the north, generally taking the form of small domes and pillow mounds with flat to rounded tops and relatively steep sides (*Fig. 26, left side of Fig. 27*). The reason for this increase in constructional volcanism is unclear, but may be related to a change in composition or a local increase in melt supply. Near the northern end of the segment, where activity is dying out, the dome clusters look strikingly similar to the “last gasp” volcanic features seen in the extinct portions of the NELSC-S (*Figs. 24-25*). This similarity may indicate that these types of volcanic features are common along dying spreading axes, but a closer examination, including sampling, would be required to confirm this interpretation. The dominant style of volcanism along this segment consists of pillow mounds and small domes, although small lumpy flows can be seen breaching the faults bounding the neo-volcanic zone in some locations.

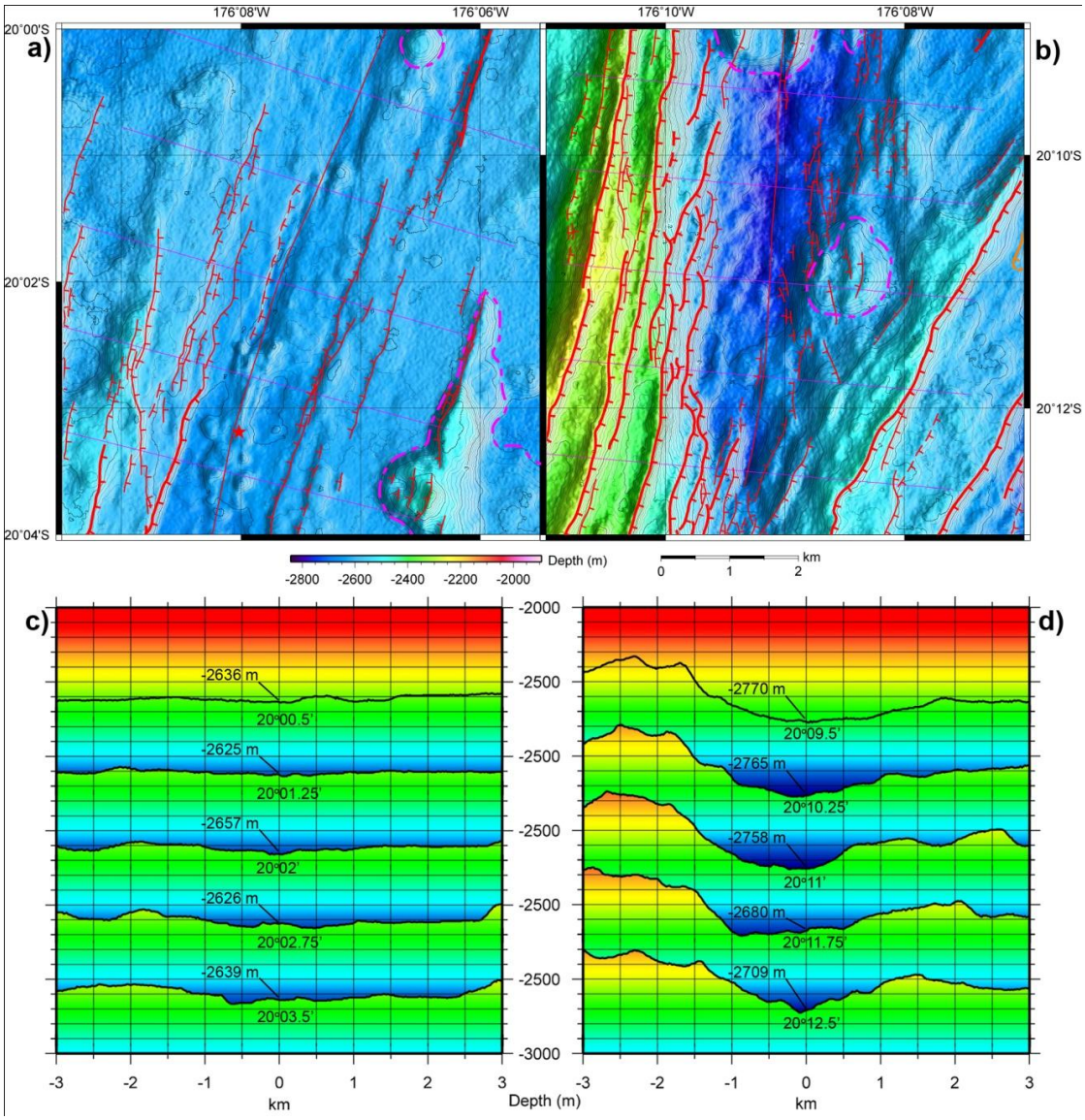

Figure 27: NELSC-N focus areas, bathymetry and across-axis profiles. a) and b) EM-120 (20 m cell size); c) and d) across-axis profiles from two portions of the NELSC-N, chosen to show two contrasting examples of near-axis morphology. The northern area (left side) is an example of the flat axial morphology that is typical of most of the length of the NELSC-N, while the southern area (right side) shows how the character of the axis changes as it propagates into thicker crust at the southern end of the segment. *Fig. 28* shows corresponding sidescan imagery. Spreading axis picks are shown as solid red lines and identified hydrothermal vent sites are shown as red stars. Mapped faults are indicated with red lines with tick marks pointing down-dip and dashed where approximate, constructional volcanic features are outlined with a dashed magenta line, recent mappable lava flows are outlined in solid purple, and mass wasting features are indicated with orange lines. [Data sources: *Goodliffe, 1995, Martinez and Taylor, 2006, Martinez et al., 2008, Dunn et al., 2009, Escrig et al., 2009*].

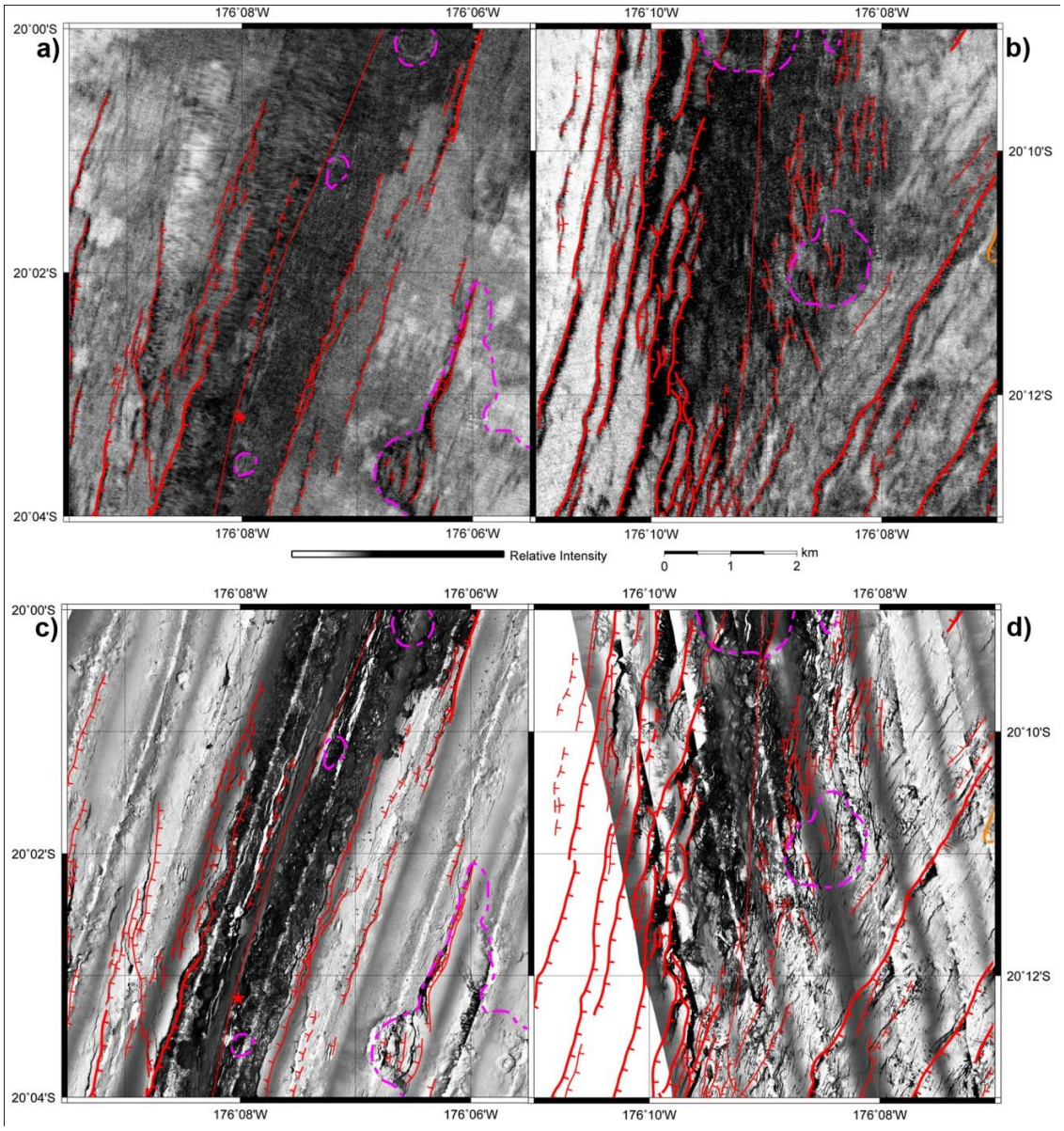

Figure 28: NELSC-N focus areas, sidescan images. a) and b) EM-120 (top, 20 m cell size); c) and d) IMI-120 (bottom, 2 m cell size) sidescan images from two portions of the NELSC-N, chosen to show two contrasting examples of axial morphology. The northern area (left side) is an example of the flat morphology that is typical of most of the length of the NELSC-N, while the southern area (right side) shows how the character of the axis changes as it propagates into thicker crust at the southern end of the segment. Spreading axis picks are shown as solid red lines and identified hydrothermal vent sites are shown as red stars. Mapped faults are indicated with red lines with tick marks pointing down-dip and dashed where approximate, constructional volcanic features are outlined with a dashed magenta line, recent mappable lava flows are outlined in solid purple, and mass wasting features are indicated with orange lines. [Data Sources: Martinez and Taylor, 2006, Martinez et al., 2008].

4.72 Variations in faulting and hydrothermal activity (NELSC-N)

There is not a discernable along-axis trend in fault abundance, length, and displacement along the NELSC-N. The majority of the axis is bounded by faults with throws up to a few 10's of m at most, increasing in apparent displacement where there are locally higher relief portions of the seafloor. These small faults typically contain the highly reflective recent volcanism within the neo-volcanic zone, creating a very abrupt boundary to the high backscatter zone, but some small flows breach these faults where throws are particularly small. The only region that varies significantly in this regard is the portion of the axis at the southern end that is propagating into thicker crust and shutting down the NELSC-S. Here we see a complex pattern of faulting that takes the typical "v" shape that is seen at propagating ridge tips elsewhere around the world. However, the "v" appears to be rotated clockwise relative to the orientation of the axis here, causing the faults and the overall fabric to be sub-parallel to the axis on the west side and at a higher angle to the axis on the east side. This effect could largely be due to the fact that the southern tip curves toward NELSC-S axis to the east, a common feature of overlapping ridge tips [*Sempere and Macdonald, 1986*]. If the axis followed it's orientation along the central portion of the segment, it would probably be centered within the "v". Hydrothermal activity is generally more abundant than along the NELSC-S, although it appears to be concentrated at one vent field at around 20^{o}03'-04' S, named Kilo Moana [*Baker et al., 2006, Baker et al., 2010*].

5. Discussion

5.1 Summary of Observations and Results

Systematic first-order along-axis geologic, geochemical, and geophysical variations have been documented in previous studies in the Lau basin [*Parson et al., 1990*, *Parson and Hawkins, 1994, Pearce et al., 1994, Taylor et al., 1996, Harding et al., 2000, Zellmer and Taylor, 2001, Martinez and Taylor, 2002, Taylor and Martinez, 2003, Martinez et al., 2006, Jacobs et al., 2007*], along-axis

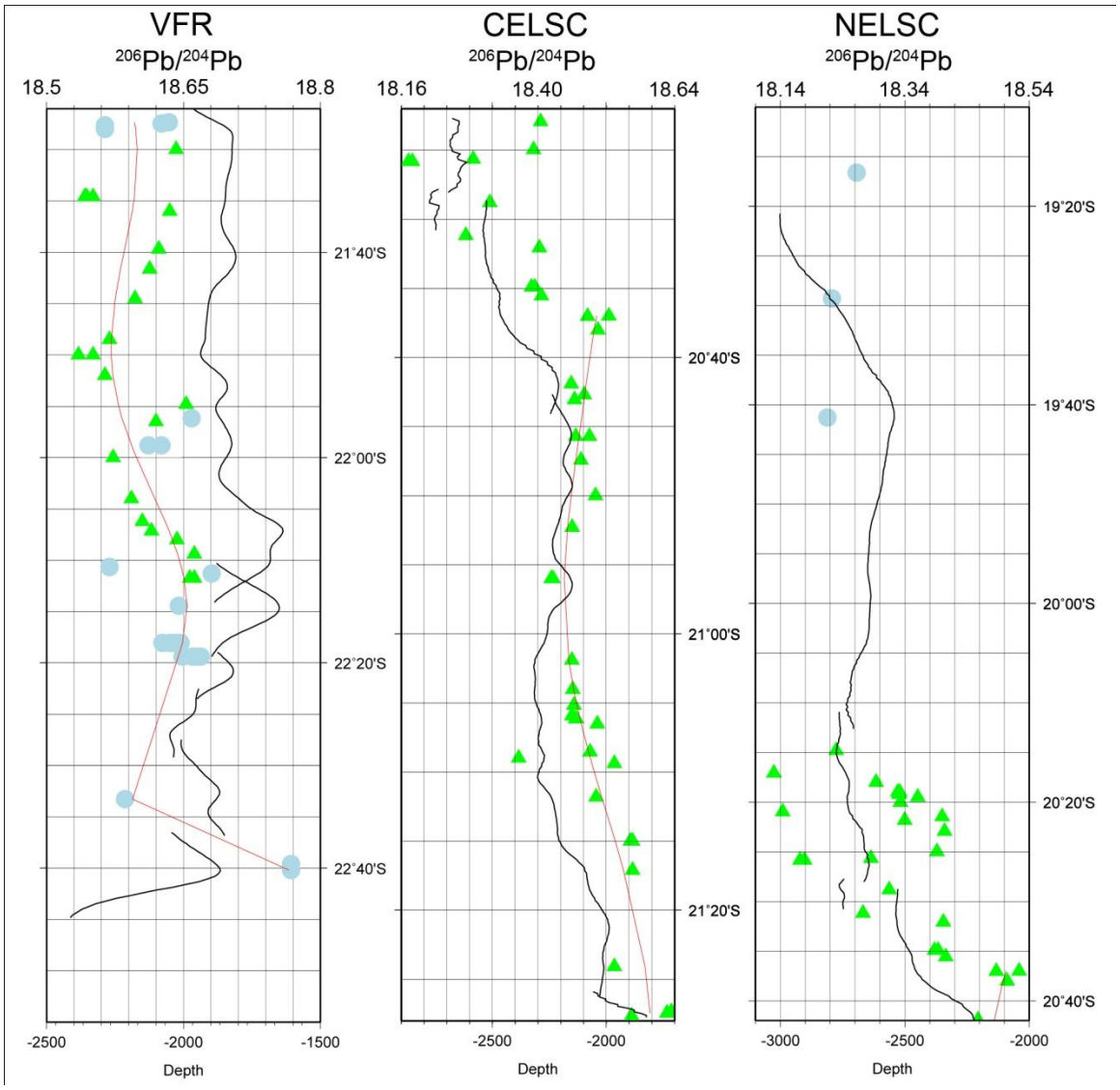

Figure 29: Smoothed profiles overlain with $^{206}Pb/^{204}Pb$ ratios. The smoothed profile removes the fine-scale variations in axial depth and emphasizes the overall intra-segment pattern, while the $^{206}Pb/^{204}Pb$ ratios [*Jenner et al., 1987, Vallier et al., 1991, Loock et al., 1992, Peate et al., 2001, Escrig et al., 2009*] show the correlation between subduction influence and axial depth.

variations in hydrothermal activity have been examined [*Baker et al., 2006, Martinez et al., 2008, Baker et al., 2010*] and very detailed studies of hydrothermal vent sites and sub-meter scale features have been performed [*Ferrini et al, 2008*]. The observations and interpretations presented in this study focus on intermediate-scale variations within second-order spreading segments in both geologic characteristics and subduction influence. Along the VFR and

CELSC-S, there is a consistent pattern of relatively shallower and higher relief segment ends compared to the segment centers (*Fig. 29*). With some local exceptions, this same pattern is reflected in the variation of $^{206}Pb/^{204}Pb$ ratios along the CELSC-S and VFR-N, where the overall variation takes on the shape of a sinusoidal curve with relative highs corresponding to the segment ends and relative lows corresponding to the centers of the segments (*Fig. 8*). This sinusoidal trend is superimposed on the larger first-order linear trend represented by the dashed blue line in *Fig. 8*, suggesting that the variation in subduction influence is more complex than a simple linear variation with arc proximity. Along the VFR-N, *Escrig et al.,* 2009 correlated the local highs in $^{206}Pb/^{204}Pb$ ratios along the VFR-N axis with arc volcanoes that project along the same slab flow lines, and it was noted in this study that these also project toward local morphologic highs along the axis as well. This suggests that these undulations in subduction influence may extend laterally toward the arc, similar to the geometry of "hot fingers" in the Northeast Japan arc [*Tamura et al., 2002*], arc and rift regimes and cross-arc chains in the Southern Havre Trough [*Wysoczanski et al., 2010*], and zones of enhanced magmatism that cross the backarc in the Mariana Trough [*Oakley et al., 2009*]. These studies and their connection to the observations in the Lau basin will be discussed in detail in section *5.2*.

The roughly sinusoidal pattern of intra-segment variation along the CELSC-S and VFR also has implications for controls on backarc ridge segmentation. The standard model of segmentation along MOR's predicts that magmatism should decrease toward segment ends and increase toward the center [*Macdonald et al., 1991a*], while the opposite pattern is observed along the CELSC-S and VFR. This observation indicates that the standard MOR segmentation model may not be applicable to backarc spreading centers. The consistent association of local highs in subduction influence and the ends of second-order segments may even suggest that overlapping segment ends preferentially form over these regions of enhance magmatism. See section *5.3* for a more detailed discussion of these implications.

North of the 20.6^{o} S transition along the CELSC-N, the morphology of the axis abruptly flattens and deepens, magmatism drops sharply, crustal thickness decreases while density increases, lavas become more basaltic, and there are no longer sinusoidal variations in axial depth or morphology [*Peate et al., 1994, Martinez et al., 2006, Dunn and Martinez, 2011*]. This abrupt change is also reflected in the $^{206}Pb/^{204}Pb$ ratios, which drop sharply across the 20.6^{o} S geochemical transition zone and show a scattered pattern at uniformly low values north of the transition (*Fig. 8*). Between the VFR-S and VFR-N, there is another abrupt change from sharply defined alternating zones of low backscatter and high backscatter volcanism along the VFR-S to more gradual and much more subtle changes in style of volcanism along the VFR-N. The pattern seen along the VFR-S could be explained by isolated diapirs of strongly subduction-influenced magma advecting directly under the axis of the VFR-S with relatively minimal mixing in the axial magma chamber before erupting on the seafloor, or possibly as an effect of third-order segmentation. *Haase, 2009* found that geochemical variations in the off-axis seamounts around the VFR-S support a model where each seamount is fed by a distinct diapir of melt, so it would not be hard to imagine how one of these diapirs could be assimilated into the sub-axial melting regime. This concept will be discussed in greater detail in Section *5.4*. These abrupt transitions in mantle properties and the geologic characteristics of the axis support a model of mantle wedge convection with sharp boundaries between multiple convection cells rather than a single convection cell through the entire wedge [*Dunn and Martinez, 2011*], although more work is needed to evaluate this model.

5.2 Geometry of Subduction-influenced Zones in the Mantle Wedge

In order to place these observations in a larger context, it's important to look at other backarc environments where geologic variations of a similar scale have been observed along the length of the backarc system. In the Northeast Japan arc, *Tamura et al., 2002* identified anomalous low seismic velocity zones with a transverse orientation relative to the trend of the arc, which they referred to

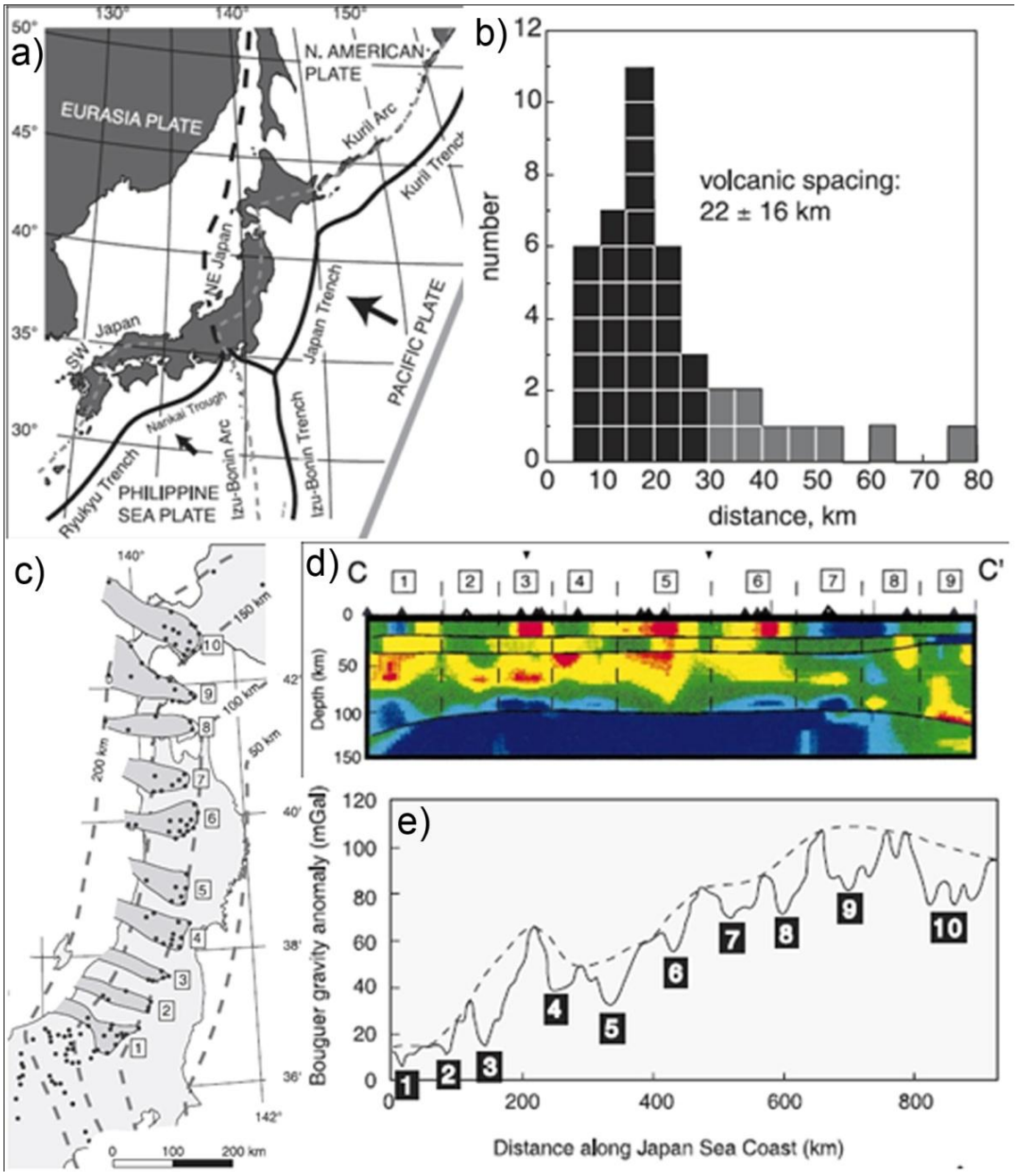

Figure 30: "Hot fingers" in the NE Japan arc. a) location/tectonic map; b) volcano spacing histogram; c) "hot fingers" interpretation, dots are quaternary volcanoes; d) along-axis seismic tomography; e) Bouguer gravity anomaly profile. [Taken from: *Tamura et al., 2002*]

as "hot fingers." (*Fig. 30*) These fingers were identified in seismic tomography and correspond well to negative Bouguer gravity anomalies. They were expressed within the backarc mantle as ten ~50 km wide zones distributed along the length of the arc, separated by gaps of ~30-75 km, and oriented parallel to

the convergence direction, nearly orthogonal to the trend of the arc. Quaternary volcanoes were largely clustered on the topographic swell in the basement rock overlying these hot fingers as well. These features were interpreted as anomalously hot regions of upwelling mantle arranged in a configuration which roughly resembled ten parallel fingers [*Tamura et al.,* 2002]. It should be mentioned that these hot fingers may actually be "wet fingers," caused by concentrated regions of high water content rather than thermal anomalies, an explanation that may be more likely considering the cold, water-rich slab underlying the mantle wedge. A similar pattern was identified in a more recent study by *Wysoczanski et al., 2010* in the Southern Havre Trough (SHT), south of the Lau basin behind the Tonga-Kermadec subduction zone from ~32^{o} to 36^{o} S, where the backarc is much narrower, opening is slower, and it has not yet matured into a focused, organized spreading system (*Fig. 31*). In the SHT, the hot (or wet) fingers are expressed on the seafloor as chains of recently active arc-like volcanoes constructed on top of elevated basement plateaus that are oriented parallel to the Pacific-Tonga convergence direction and extend across the backarc [*Wysoczanski et al., 2010*]. In the Lau basin itself, *Escrig et al., 2009* identified geochemical correlations between lavas erupted along the ELSC and VFR and arc volcanoes that lie along a line projected parallel to the convergence direction, similar to the geometry of the hot fingers of Northeast Japan and the cross-arc chains of the SHT [*Escrig et al., 2009, Tamura et al.,* 2002, *Wysoczanski et al., 2010*]. Among other correlations, three local highs in $^{206}Pb/^{204}Pb$ ratios along the VFR-N axis lined up with the locations of three arc volcanoes, suggesting that there may be a common explanation for the spacing of the volcanoes and the spacing of the relative Pb highs along the axis (*Fig. 33*) [*Escrig et al., 2009*]. They ascribed the sinusoidal trend along the VFR-N to diapirs of enriched material underlying each of the relative highs in $^{206}Pb/^{204}Pb$ ratios, and noted that the ~65 km wavelength of the sinusoid is strikingly similar to the worldwide average spacing between arc volcanoes [*Marsh, 1979, Escrig et al.,* 2009]. However, the Lau basin lacks the obvious topographic swells of the Northeast Japan arc or the cross-trending volcanic chains and basement swells

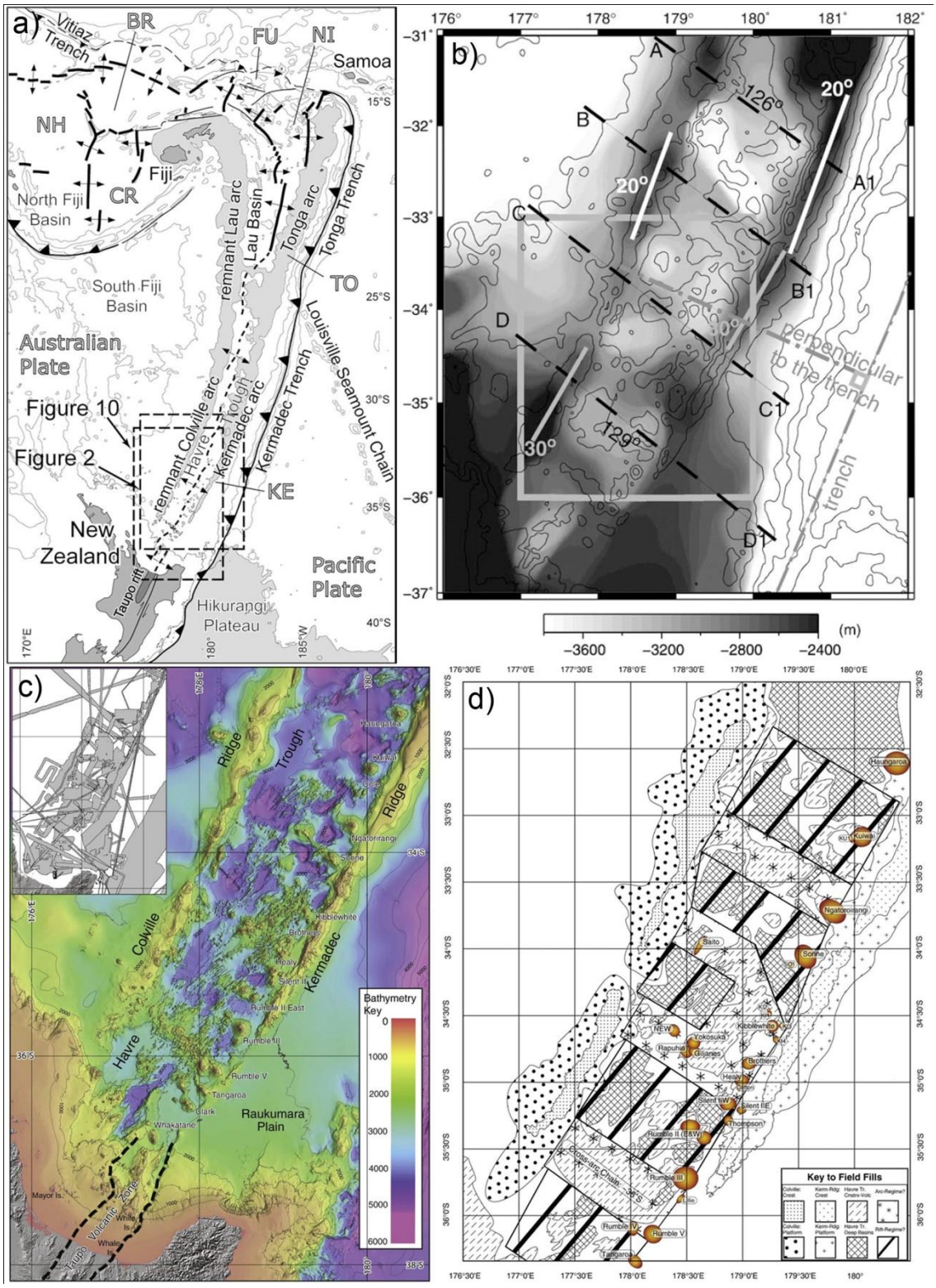

Figure 31: Arc vs. rift regime in the Southern Havre Trough. a) location map; b) long-wavelength depth anomaly; c) compiled bathymetry map; d) interpretive structural map showing arc regime as striped zones and rift regime as starred zones. [Taken from: *Wysoczanski et al., 2010*].

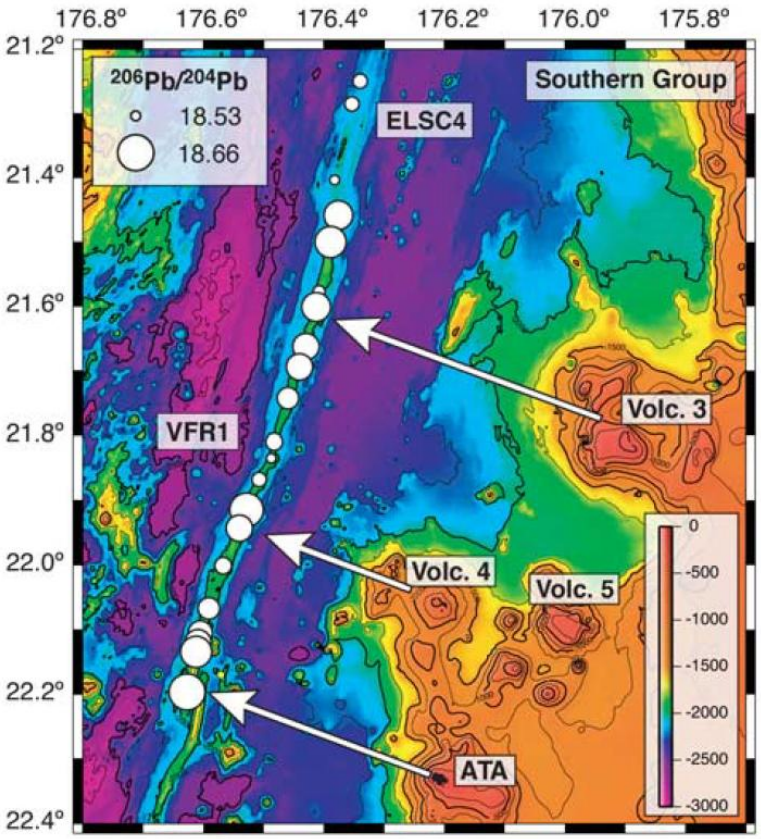

Figure 32: Geochemical connections between the arc and VFR-N. The arrows are aligned along the slab flow lines, showing the connection between the arc volcanoes and relative highs in 206Pb/204Pb ratios along the VFR-N. [Taken from: *Escrig et al., 2009*].

of the SHT; cross-arc chains of volcanic cones are not very well defined, especially north of the VFR. In a mature backarc spreading system like the Lau basin, the combination of increased horizontal distance from the arc and increased vertical distance from the slab likely cause the melt to be distributed in a more diffuse manner, diminishing and smearing out the expression on the seafloor. This effect may be exacerbated by the steeper dip of the slab under the Lau basin relative to Japan, ~45^{o} on average compared to ~30^{o}, respectively [*Lallemand et al., 2005*]. The steeper dip would cause the subduction-related effects to die out more quickly away from the arc. Unfortunately, limited seismic tomography data in the region between the Tofua arc and the spreading axis makes it impossible to directly observe the distribution of low-velocity zones in the mantle underlying the Lau basin. The Mariana Trough may provide a closer analogue to the Lau basin because it also has a well established organized spreading system. *Oakley et al., 2009* described zones of enhanced magmatism trailing across the backarc basin from sites of rifted arc volcanoes on the remnant

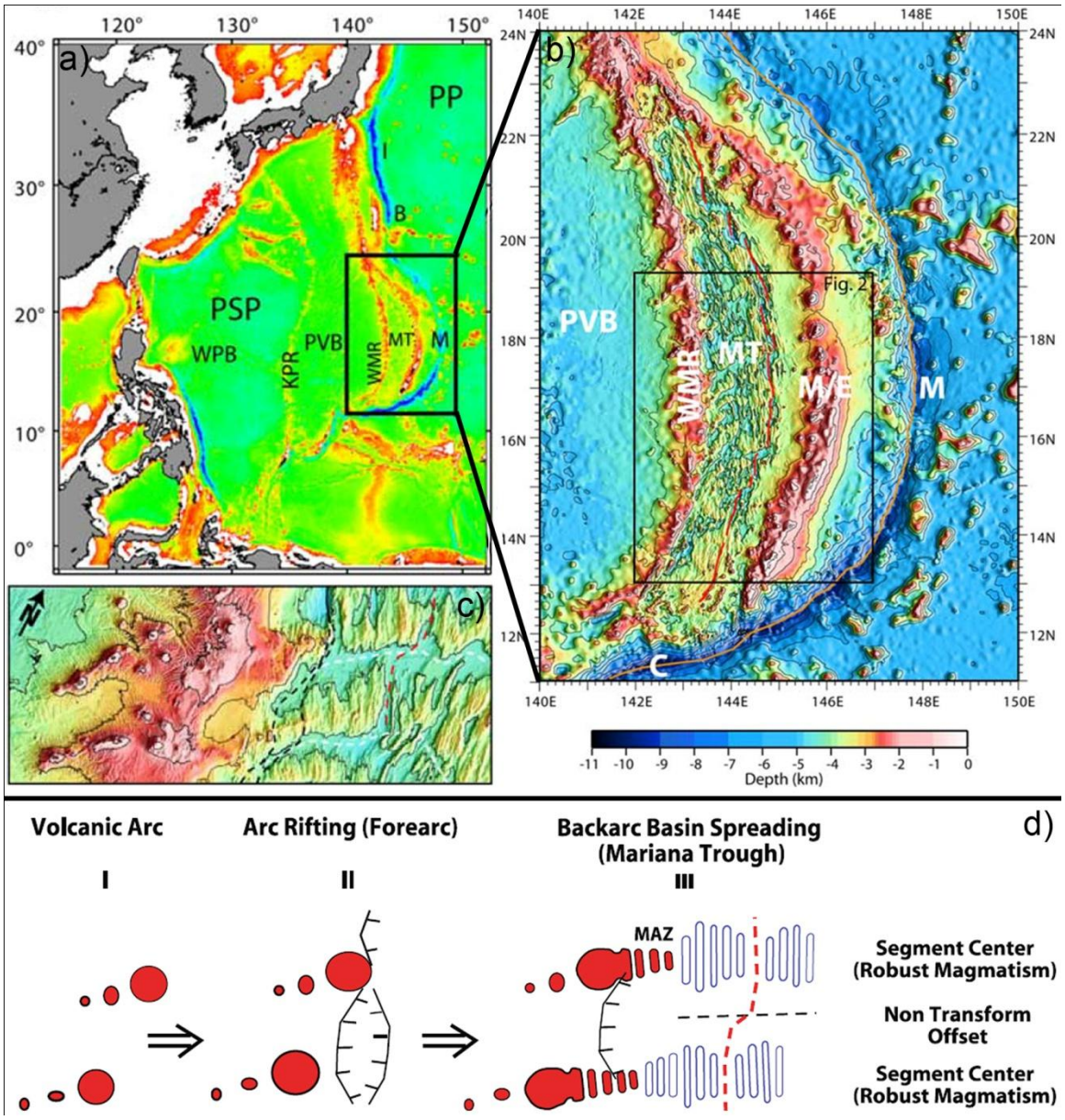

Figure 33: Zones of enhanced magmatism in Mariana trough. a) location map; b) Mariana trough bathymetry map; c) close-up of bathymetry showing zones of magmatically robust seafloor fabric trailing from West Mariana Ridge remnant across the backarc, spreading center drawn with dashed red line, arc/backarc transition drawn with dashed black line; d) interpretation of evolution of zones of enhanced magmatism. [Taken from: *Oakley et al., 2009*]

West Mariana Ridge. In this environment, where spreading is well organized, these sites of enhanced magmatism are expressed as magmatically robust seafloor spreading fabric rather than as chains of seamounts (*Fig. 33*). Thus, the expression of these hot (wet) fingers may vary from distinct volcanic edifices in

the case of Northeast Japan, where there is no backarc extension, to modulation of seafloor fabric where spreading is well organized (in the Mariana basin), and may be further attenuated where spreading is faster, as in the Lau basin. If a similar mechanism is operating in the Lau basin mantle wedge, it would provide at least a partial explanation for the pattern of alternating highs and lows in slab input along the length of the spreading system, as well as a plausible mantle origin for the pattern of intra-segment variation observed on the seafloor. The observation of similar patterns within these contrasting backarc environments suggest that hot (wet) fingers may be the preferred geometry for ascending bodies of subduction-influenced magma in other subduction zones around the world as well.

5.3 Backarc Segmentation

One alternative to a hot (or wet) fingers-based model would be one that attributes the patterns in morphology and volcanism primarily to segmentation effects such as those identified by *Macdonald et al., 1991a* along mid-ocean ridges. This type of model would attribute the majority of the intra-segment variations in morphology and volcanism as the natural results of second- and third-order segmentation. However, along mid-ocean ridges the morphologic pattern appears to be opposite of what is observed along the CELSC-S and VFR. *Macdonald et al., 1991a* noted that MOR segments tend to be relatively shallow near the center of the segment overlying the melt source, getting deeper toward the ends and showing signs of reduced melt supply. Along the CELSC-S and VFR, the segment ends are consistently shallower and have higher axial relief compared to the central portions. Magmatism in general also appears to be more robust near segment ends, especially along the VFR-N/S overlap zone. It appears that this model of segmentation may not be applicable to the arc-proximal backarc basin environment, where the effects of the nearby subduction zone outweigh the effects of spreading rate and decompression melting of low-water content mantle that govern the characteristics of MOR's. The correlation between local morphologic highs along the segment ends of the CELSC-S and

VFR and local highs in slab input (based on $^{206}Pb/^{204}Pb$ ratios) suggests that perhaps second-order segment ends along backarc spreading centers preferentially form over these regions of locally increased melting. This theory would explain the pattern of along-axis morphologic variation as well as how it is possible to have AMC reflectors and abundant magmatism under two adjacent segments in an overlap zone, where you might expect that they would be competing for the same melt supply [*Turner et al., 1999, Harding et al., 2000, Jacobs et al., 2007*]. Overlap zones may be overlying or adjacent to a diapir or body of melt with a high concentration of water and other slab-derived components, creating the local highs in morphology and $^{206}Pb/^{204}Pb$ ratios. The data is inadequate at this stage to establish a causal connection between local maxima in slab input and the locations of second-order segment ends, but the consistent correlation along the CELSC-S and VFR warrants further consideration.

5.4 Small-scale geometry of ascending magma in the mantle wedge

Another implication of the results of this study is that it helps constrain the possible mechanisms of small-scale melt transport to backarc spreading centers as well as the large scale geometry. On a large scale, based on the pattern of intra-segment variation seen along the ELSC and VFR, as well as patterns seen in the Northeast Japan arc, the SHT, and the Mariana Trough, it seems that the water-rich melt rising from the slab is not ascending in a uniform curtain of melt along the length of the subduction zone, but is spatially segregated along-strike in some manner, with a spacing on the order of ~50-60 km [*Tamura et al., 2002, Wysoczanski et al., 2010, Oakley et al., 2009*]. However, there must be a smaller scale level of spatial segregation to produce the individual volcanic cones that we see on the seafloor both in the arc and the backarc. *Haase et al., 2009* performed a detailed geochemical study of off-axis seamounts east, west, and south of the VFR which sheds some light on the smaller scale segregation of subduction-influenced magma bodies (*Fig. 34*). In general, lavas from the off-axis seamounts to the east and west are more primitive and basaltic than axial

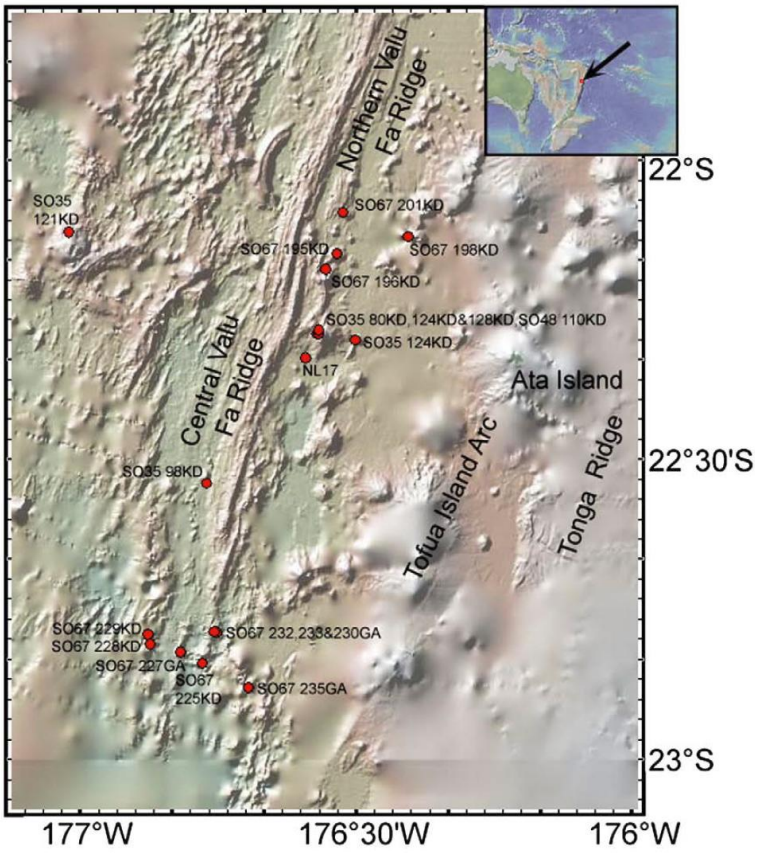

Figure 34: Bathymetry plot showing sample locations from off-axis seamounts west, east, and south of VFR [Taken from: *Haase et al., 2009*].

lavas, also showing evidence of higher sediment input than the arc lavas. Compositions are more heterogeneous than those along the arc or along the axis, consistent with reduced residence time, mixing, and fractionation in smaller melt batches under each volcanic edifice. The geochemical variations in these seamount lavas support the idea of smaller-scale diapiric ascent of hydrated or partially molten mantle relative to the volcanic front, creating separate magma supply systems for each off-axis seamount. The seamounts south of the VFR-S propagator are erupting more arc-like lavas, similar to those erupted along the VFR axis, indicative of increased magma production due to the influx of water into the underlying mantle [*Haase et al., 2009*]. This suggests that, at least within a certain distance of the arc, the bodies of hydrous melt ascending from the slab take the form of diapirs on the scale of a few km in size. This geometry may help in explaining why there are such abrupt changes in morphology and style of volcanism along the VFR-S. It could be that the locations where highly reflective sheet flows dominate the axis, such as from 22°17' S to 22°20' S (*Fig. 6*),

correspond to locations where the primitive, basaltic melt that feeds the off-axis seamounts is directly advected by the spreading axis. The locations where volcaniclastics dominate the axis could be erupting more fractionated lavas that have spent more time in the axial magma chamber and have exsolved greater quantities of water, although there may be at least a partial depth control on the distribution of explosive versus effusive volcanism as well [*Chadwick et al., 2005*]. Analysis of more samples along the rest of the VFR-S axis would help to evaluate this theory and see if there is a consistent compositional correlation between the off-axis seamounts and lavas from various portions of the VFR-S.

While isolated diapirs may help to explain some of the abrupt changes seen along the VFR-S, a different mechanism must be invoked to explain the more gradual changes seen on the VFR-N and the CELSC south of the 20.6^{o} S transition. It appears that there is a zone within ~50 km of the arc where the conical off-axis seamounts occur and beyond which they disappear, suggesting that there is a change in the geometry of bodies of hydrous melt and the mechanism for melt delivery to the axis. There are large uncertainties in the nature of mantle wedge circulation and very little is known about the mechanisms for delivering hydrous slab-derived melt to backarc spreading centers, so any theories on this are speculative at this stage in our knowledge of backarc systems. *Escrig et al., 2009* proposed that beyond a certain distance from the arc, the diapirs may become mixed into the sub-axial melting regime at depth, or the melt may find some other pathway through the mantle wedge, such as "high-porosity channels." Any proposed mechanism would have to explain at least two things. The first would be the question of why there are such abrupt changes along only the VFR-S, and what causes the changes to be more gradual along the segments to the north, whether it's deeper mixing in the axial magma chamber or some other process. Also, the mechanism would have to explain a way for the melt to physically travel to the spreading center, either a direct path through the mantle wedge in the form of high-porosity channels or something similar, or perhaps by travelling in channels along the base of the lithosphere to the axis rather than through the wedge. It's likely that a large scale change in the

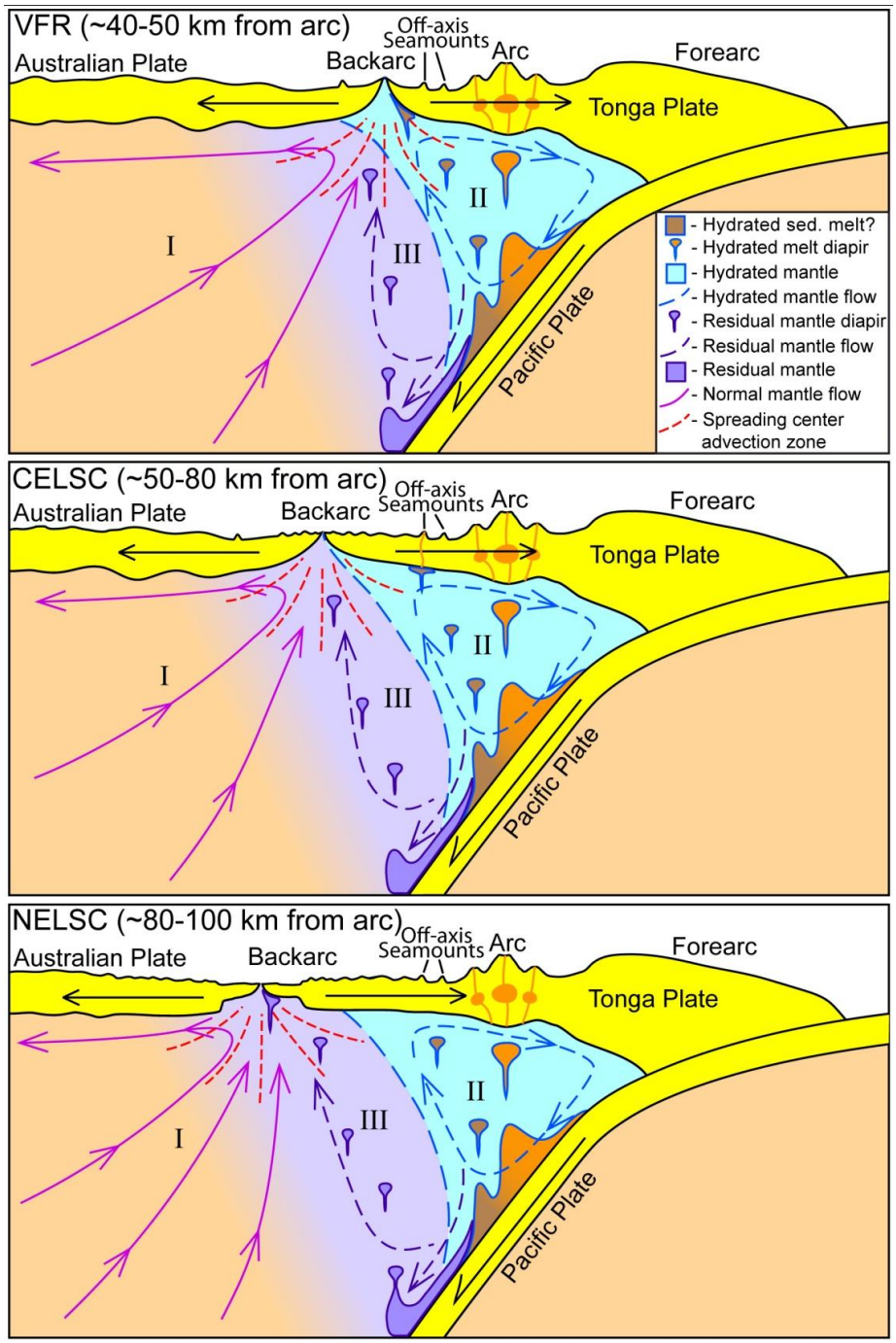

Figure 35: Schematic interpretive cross-sections through the VFR, CELSC, and NELSC. Sections are drawn through hypothesized "hot fingers" represented by the orange zone above the slab. Main concepts: 1) Distinct mantle domains (adapted from *Dunn and Martinez, 2011*): I: normal MORB mantle, II: Hydrated mantle underlying VFR and arc, III: Depleted, buoyant mantle underlying NELSC; 2) Recirculation of material under arc; 3) Increasing sediment contribution and smaller diapirs feeding off-axis seamounts; 4) Down-dragging and possible diapiric ascent of buoyant domain III material; 5) Schematic changes in crustal thickness and axial morphology.

nature of the mantle wedge and/or melt delivery mechanism occurs along the 20.6^{o} S transition as well, but the nature of this is only beginning to be understood [*Dunn and Martinez, 2011*]. For the time being, more data need to be collected to make any conclusions about melt delivery mechanisms to backarc spreading centers.

5.5 Insensitivity of faulting and hydrothermal activity to intra-segment variations

One interesting observation in this study is the apparent insensitivity of faulting and hydrothermal activity to the intra-segment variations in morphology and $^{206}Pb/^{204}Pb$ ratios. These characteristics appear to simply follow the overall first-order trend of decreasing subduction influence and increasing spreading rate toward the north, and don't show a consistent pattern at the intra-segment scale. This is likely due to the fact that morphology and axial depth are directly influenced by melt supply and would respond relatively quickly to local changes in melt supply, while faults may take some time to respond to short-term changes in melt supply. Another major factor that affects the ability to observe intra-segment patterns in faulting is that it is often difficult to map small faults and fissures near the axis due to burial by volcanism and difficulty identifying individual faults in the sidescan data within the highly reflective neo-volcanic zone. If the local variations in magmatism are primarily reflected in the small faults within the neo-volcanic zone, any patterns that do exist would be very difficult to discern.

Hydrothermal activity does appear to vary widely within individual segments, but there is not a consistent association with segment ends or regions of relatively increased magmatism or $^{206}Pb/^{204}Pb$ ratios. This may be because hydrothermal activity is strongly affected by the structure and permeability of the crust rather than melt supply alone. Hydrothermal systems are typically short-lived and shift locations based on small changes in crustal permeability and heat sources. These changes may affect hydrothermal activity without affecting anything that is observable on the seafloor at the scale of this study. This provides an explanation for why hydrothermal activity does not vary with the

same pattern as ridge morphology and $^{206}Pb/^{204}Pb$ ratios, and suggests that the controls on hydrothermal activity vary at an even smaller scale. It is interesting that although plume incidence overall increases with spreading rate toward the north, the single most hydrothermally active portion of the axis appears to be just south of the 20.6^{o} S transition zone [*Baker et al., 2006, Baker et al., 2010*]. This location also has the by far the highest temperature spike according to CTD measurements [*Baker et al., 2006*]. This suggests that there may be rapid cooling associated with this transition, possibly as the larger axis-bounding faults begin to develop around 20^{o}38'-40' S, providing a deeper, wider pathway for fluid circulation. The nature of hydrothermal activity is temporally variable and its controls are not necessarily evident in seafloor observations. Local changes in crustal permeability and heat sources may occur without affecting anything that is observable on the seafloor, which may explain why it does not seem to follow the pattern of second-order along-axis variations.

6. Conclusions

This study has discussed in detail a set of geologic variations within second-order ridge segments, primarily expressed in axial morphology and volcanism, which are superimposed on the overall trends that vary with arc proximity. Axial depth and relief along the VFR and CELSC-S vary in an almost cosine-like pattern, where the segment ends are relatively shallower and higher relief than the central portions. These relative high points also correlate with relative highs in $^{206}Pb/^{204}Pb$ ratios in lavas collected along the axis [*Escrig et al., 2009*]. Furthermore, the spacing of these relative highs is very similar to the spacing of arc volcanoes along much of the Tofua arc and other volcanic arcs around the world [*Marsh, 1979*]. These spatial and geochemical correlations point to a common, deep origin for the patterns seen along the spreading axis and the melt feeding the arc volcanoes. Although we currently lack the data to directly image the geometry of deep magma bodies in the Lau basin mantle wedge, the hot (or wet) fingers of the Northeast Japan arc, the cross-arc structures of the Southern Havre Trough, and the patterns identified in the

Mariana Trough [*Tamura et al., 2002, Wysoczanski et al., 2010, Oakley et al., 2009*] provide insights into a plausible mechanism for creating the observed patterns along the CELSC and VFR. It is possible that a mechanism similar to this is operating in many backarc basins around the world, but more data, especially seismic tomography, will be needed to evaluate this.

Another fundamental question that this study sheds some light on is the nature of circulation in the mantle wedge. The abrupt transitions seen along the axis, especially from the VFR-S to the VFR-N and the 20.6^{o} S transition, aren't explained well by mixing and circulation in a single corner flow convection cell. Instead, the abrupt transitions seem to suggest that there may be multiple convection cells or domains within the mantle wedge with abrupt compositional and rheological differences along the boundaries [*Dunn and Martinez, 2011*]. Even if this is not the answer, there has to be some sort of abrupt geochemical, rheological, and/or thermal boundaries in the mantle driving the abrupt changes that are seen along the ELSC and VFR. At this stage, our understanding of the underlying processes that shape the features of the backarc is still limited, but hopefully this study will open the door to answering these and other fundamental question about subduction zone systems.

APPENDIX

IMI-120 vs. EM-120 as a Mapping Data Set

The hull-mounted multibeam EM-120 sidescan data has some significant advantages as a synoptic mapping data set of the ELSC/VFR axial region compared to the deep-towed IMI-120 data. Because the KM0804 survey was designed to provide overlapping coverage with the much narrower (~1 km) IMI-120 swaths, the much broader swaths (~9 km) of the EM-120 have extensive overlap and multiple redundant data points over much of the survey area. This made it possible to almost entirely remove the nadir and swath edge distortions which are inherent to sidescan data. The GPS-based navigation provides much more reliable feature locations as well. Also, the increased width of the swaths provides broader areal coverage, showing off-axis features outside of the narrower IMI-120 survey. The greater elevation above the seafloor (~2 km) also decreases shadowing of features relative to the deep-towed sonar which is typically flown ~100 m above the seafloor. Furthermore, because of its lower frequency (12 kHz) the EM-120 penetrates through the upper meter or two of sediments, revealing underlying reflective material but also making it difficult to determine where the most recent volcanism has occurred. The primary advantage of the IMI-120 system is its higher resolution, which allows identification of features on the scale of a few meters and shows surficial textures and fine-scale feature geometry in much greater detail than the hull-mounted systems. Although it has not been quantified precisely, the surficial penetration of the IMI-120 system is minimal, and a relatively light sediment cover will obscure the underlying rock. This makes the IMI-120 a valuable tool to determine where the most recent volcanic activity has occurred, because only the most recent volcanism is still exposed and highly reflective in the IMI-120 data. Also, in cases where a faint lineation in the EM-120 sidescan is ambiguous in origin, the IMI-120 can be extremely helpful in distinguishing a linear fault from a linear volcanic feature. While both systems have their strengths and weaknesses, the combination of the two data types undoubtedly provides a

significant advantage over just one or the other, especially for a study such as this that examines features at a variety of scales.

KM0804 IMI-120 Positional Corrections

The deep-towed instrument's position can only be indirectly measured through the GPS position of the ship and the digitally-monitored length of the tow cable. Deviations from the ship track as large as 100's of m can occur during turns and smaller wander can occur due to deep ocean currents. Positional corrections to the IMI-120 data from the KM0804 survey were made manually using software from Hawaiian Mapping Research Group (HMRG) at the University of Hawaii at Manoa [*Roger Davis, personal communication*]. The software allowed the deep-towed sidescan or bathymetry data to be overlaid on lower resolution ship bathymetry with more reliable positions. The best data sets for this purpose proved to be the 2 m cell size bathymetry data overlain on a hull-mounted bathymetry grid, which at the time had a cell size of 30 m. The hull-mounted sidescan images presented in this study were not available at the time. The positions were corrected through feature matching between the two bathymetry data sets. Individual points were picked on the overlying deep-towed swath and matched to the same feature on the underlying hull-mounted data. The program interpolated the track between the corrected points then automatically edited the raw data with the new positional information. This process was repeated for each individual swath throughout the KM0804 survey area. This method provided an excellent means of correcting deviations in the deep-towed data, but there are limitations. The primary limitation stems from the poor quality and high noise level of the deep-towed bathymetry data. The narrow swaths, distortion along the nadir and swath edges, and stretches of data that are dominated by noise made it difficult to reliably identify the same features in both data sets, especially when the features are relatively small. Also, the difference in resolution means that features don't look exactly the same in both data sets. In the end, it was possible to significantly improve the navigation of the data, but small deviations on the order of <100 m are inevitable.

GEOLOGIC MAPS

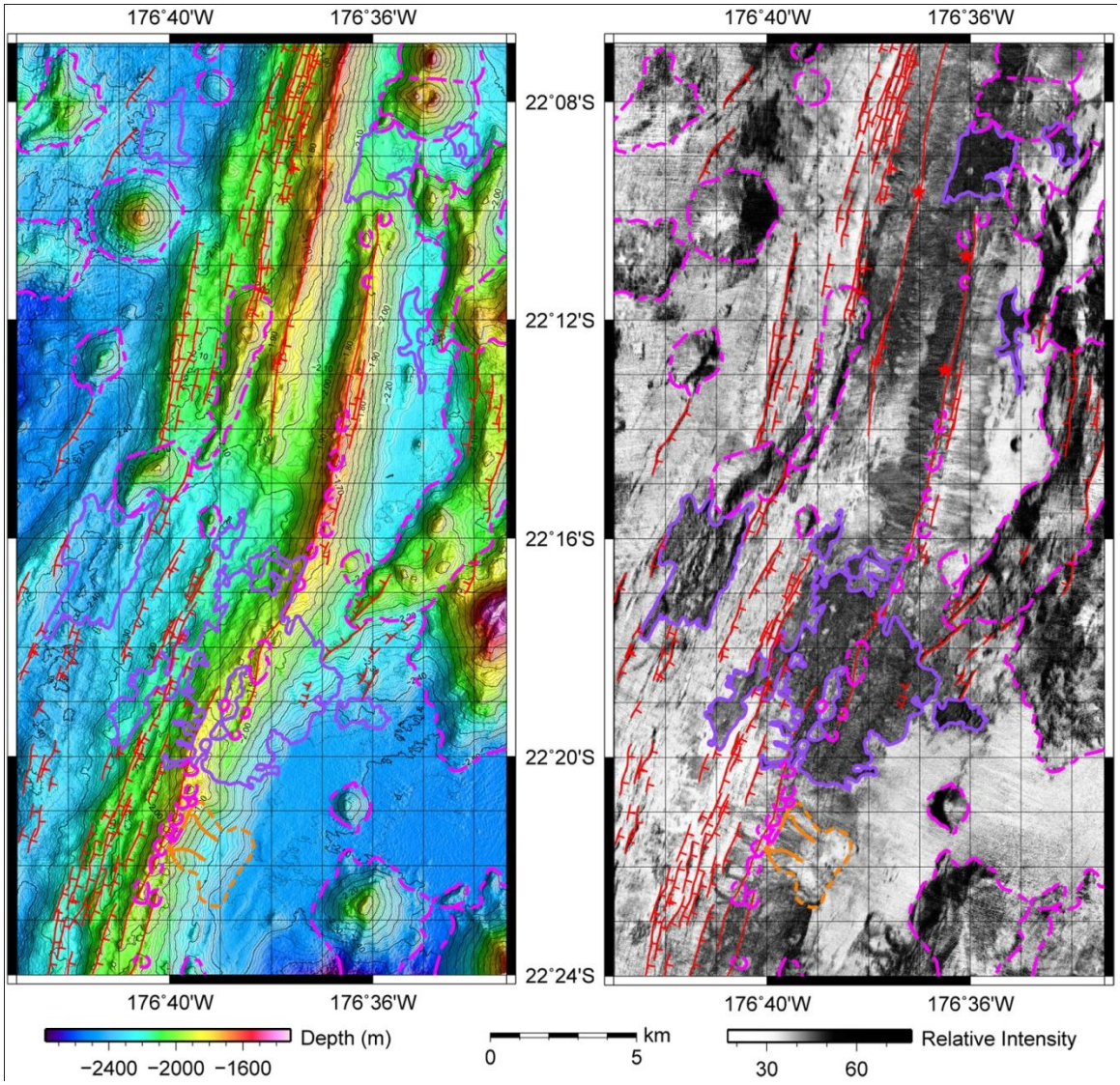

Figure A1: Geologic maps of VFR-S. EM-120 bathymetry (10 m cell size, left) and EM-120 sidescan (10 m cell size, right). Geologic mapping was limited to the portions of the segments covered by the KM0804 survey, where the deep-towed IMI-120 sidescan data was available as a reference tool. Spreading axis picks are shown as solid red lines, identified hydrothermal vent sites are shown as red stars, faults are mapped as red lines with tick marks pointing in the apparent dip direction and dashed where approximate, constructional volcanic features are outlined with dashed magenta lines, recent mappable lava flows are outlined with solid purple, and mass wasting features are indicated with orange lines. [Data sources: *Goodliffe, 1995, Martinez and Taylor, 2006, Martinez et al., 2008, Escrig et al., 2009*].

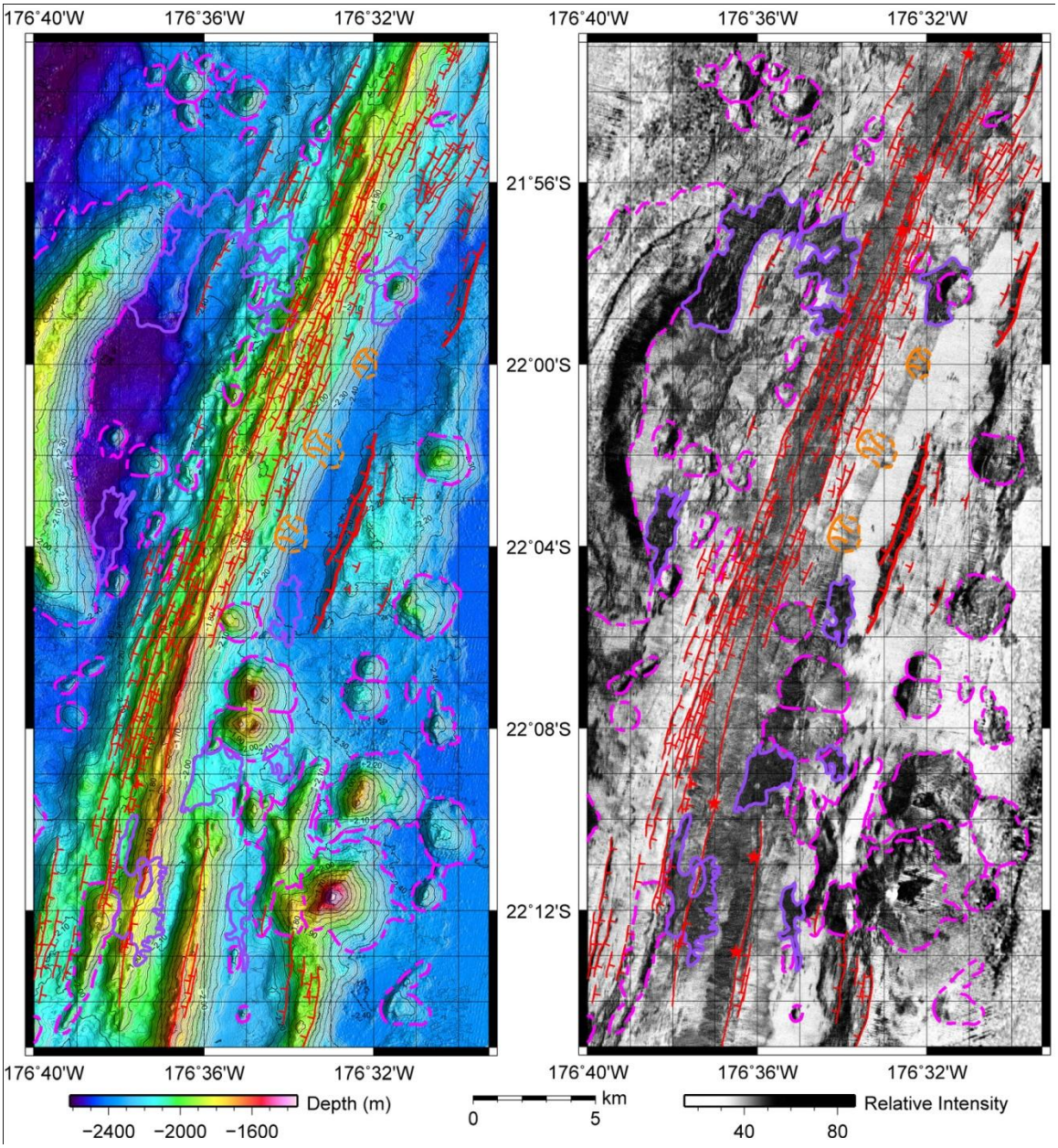

Figure A2: Geologic map of VFR-N. EM-120 bathymetry (10 m cell size, left) and EM-120 sidescan (10 m cell size, right). Geologic mapping was limited to the portions of the segments covered by the KM0804 survey, where the deep-towed IMI-120 sidescan data was available as a reference tool. Spreading axis picks are shown as solid red lines, identified hydrothermal vent sites are shown as red stars, faults are mapped as red lines with tick marks pointing in the apparent dip direction and dashed where approximate, constructional volcanic features are outlined with dashed magenta lines, recent mappable lava flows are outlined with solid purple, and mass wasting features are indicated with orange lines. [Data sources: *Goodliffe, 1995, Martinez and Taylor, 2006, Martinez et al., 2008, Escrig et al., 2009*].

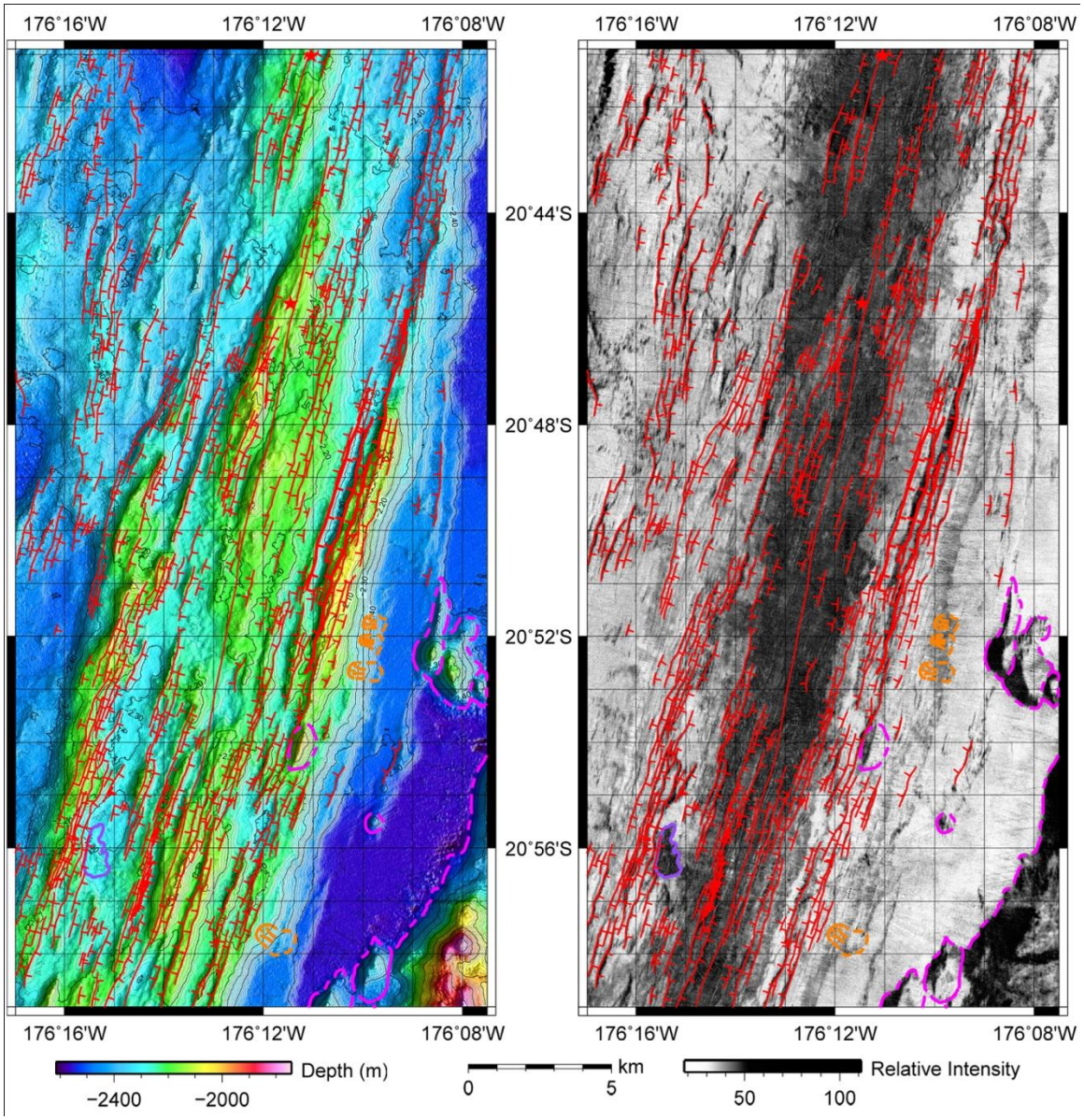

Figure A3: Geologic map of CELSC-S. EM-120 bathymetry (10 m cell size, left) and EM-120 sidescan (10 m cell size, right). Geologic mapping was limited to the portions of the segments covered by the KM0804 survey, where the deep-towed IMI-120 sidescan data was available as a reference tool. Spreading axis picks are shown as solid red lines, identified hydrothermal vent sites are shown as red stars, faults are mapped as red lines with tick marks pointing in the apparent dip direction and dashed where approximate, constructional volcanic features are outlined with dashed magenta lines, recent mappable lava flows are outlined with solid purple, and mass wasting features are indicated with orange lines. [Data sources: *Goodliffe, 1995, Martinez and Taylor, 2006, Martinez et al., 2008, Dunn et al., 2009, Escrig et al., 2009*].

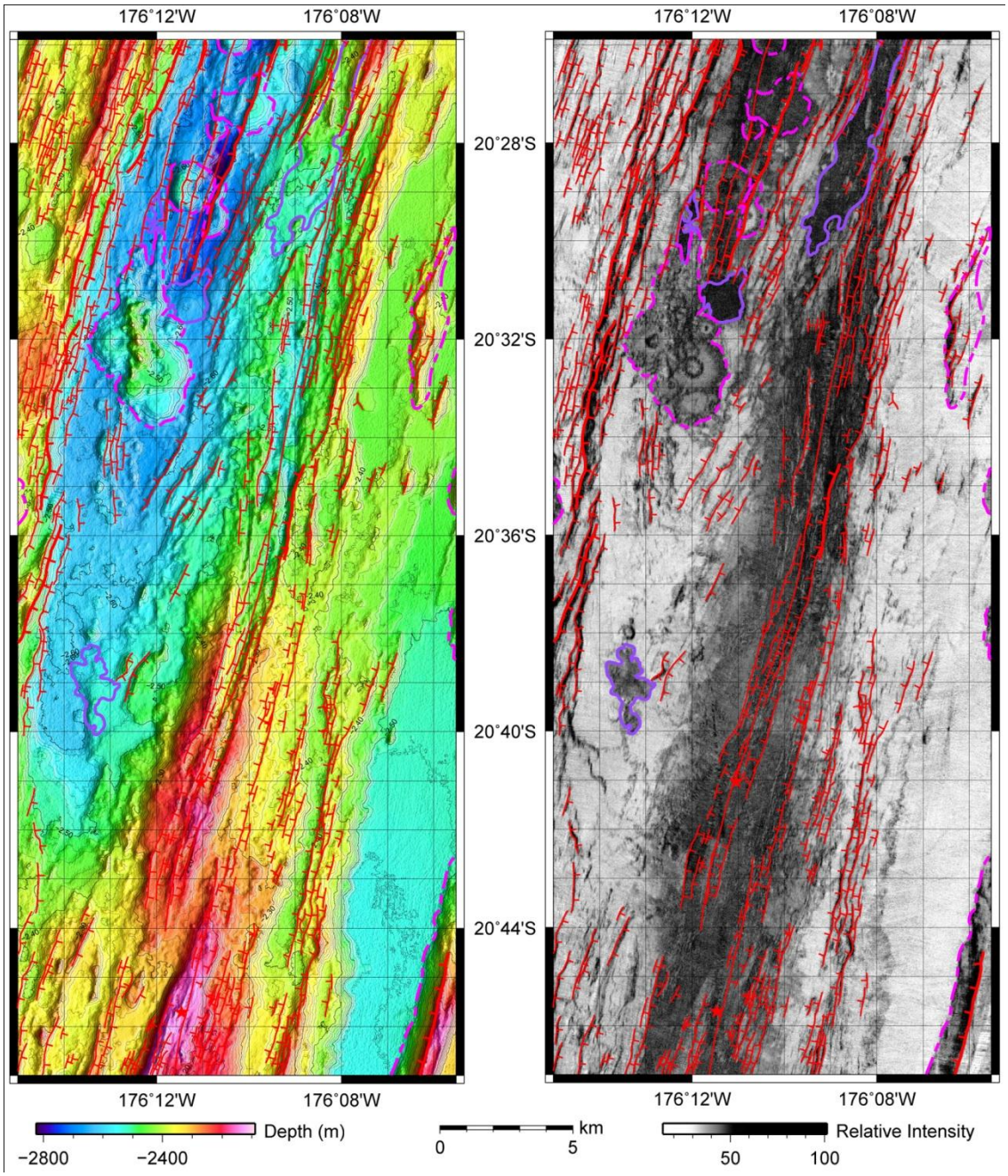

Figure A4: Geologic map of CELSC-N. EM-120 bathymetry (10 m cell size, left) and EM-120 sidescan (10 m cell size, right). Geologic mapping was limited to the portions of the segments covered by the KM0804 survey, where the deep-towed IMI-120 sidescan data was available as a reference tool. Spreading axis picks are shown as solid red lines, identified hydrothermal vent sites are shown as red stars, faults are mapped as red lines with tick marks pointing in the apparent dip direction and dashed where approximate, constructional volcanic features are outlined with dashed magenta lines, recent mappable lava flows are outlined with solid purple, and mass wasting features are indicated with orange lines. [Data sources: *Goodliffe, 1995, Martinez and Taylor, 2006, Martinez et al., 2008, Dunn et al., 2009, Escrig et al., 2009*].

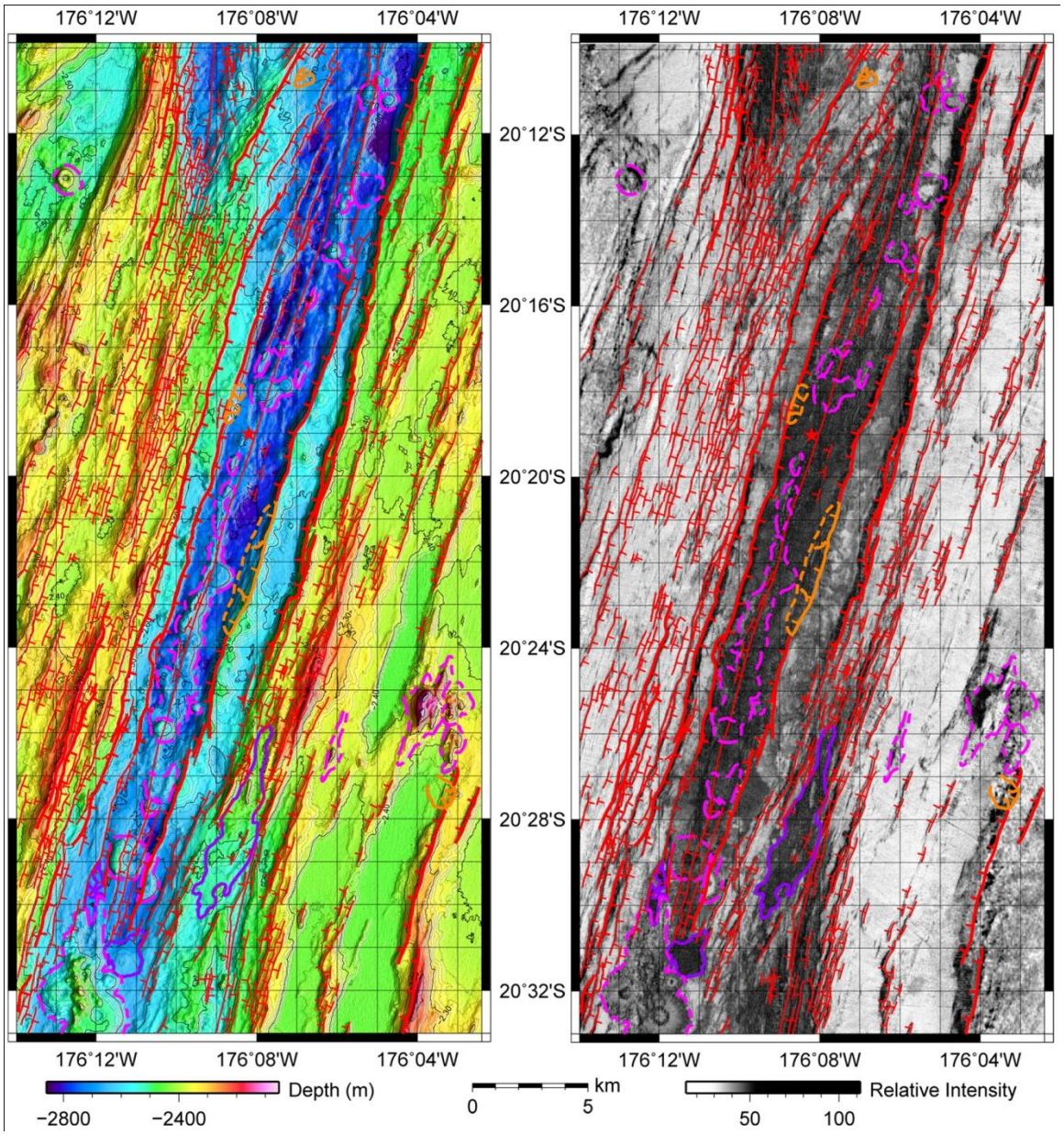

Figure A5: Geologic map of NELSC-S. EM-120 bathymetry (10 m cell size, left) and EM-120 sidescan (10 m cell size, right). Geologic mapping was limited to the portions of the segments covered by the KM0804 survey, where the deep-towed IMI-120 sidescan data was available as a reference tool. Spreading axis picks are shown as solid red lines, identified hydrothermal vent sites are shown as red stars, faults are mapped as red lines with tick marks pointing in the apparent dip direction and dashed where approximate, constructional volcanic features are outlined with dashed magenta lines, recent mappable lava flows are outlined with solid purple, and mass wasting features are indicated with orange lines. [Data sources: *Goodliffe, 1995, Martinez and Taylor, 2006, Martinez et al., 2008, Dunn et al., 2009, Escrig et al., 2009*].

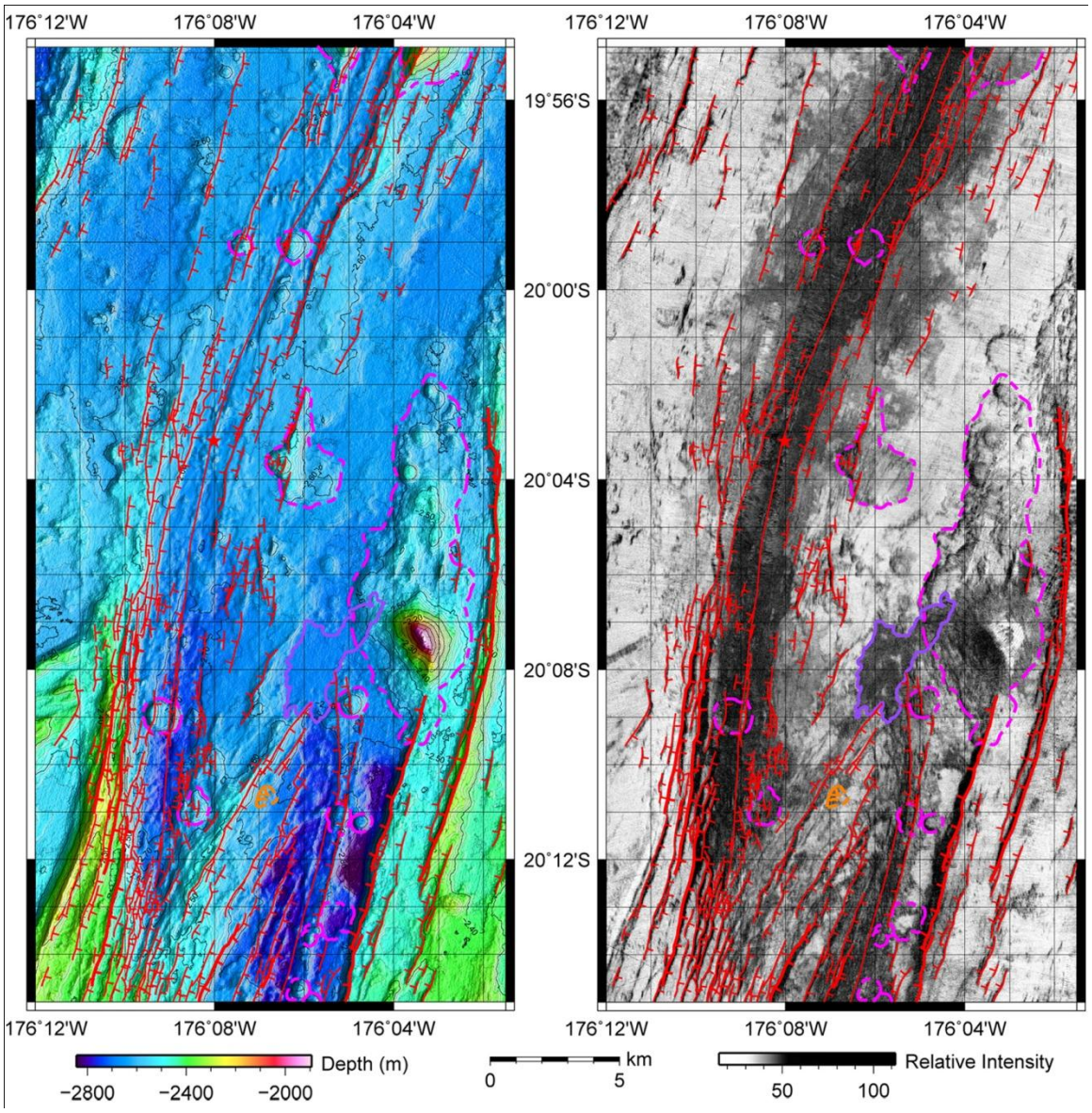

Figure A6: Geologic map of NELSC-N. EM-120 bathymetry (10 m cell size, left) and EM-120 sidescan (10 m cell size, right). Geologic mapping was limited to the portions of the segments covered by the KM0804 survey, where the deep-towed IMI-120 sidescan data was available as a reference tool. Spreading axis picks are shown as solid red lines, identified hydrothermal vent sites are shown as red stars, faults are mapped as red lines with tick marks pointing in the apparent dip direction and dashed where approximate, constructional volcanic features are outlined with dashed magenta lines, recent mappable lava flows are outlined with solid purple, and mass wasting features are indicated with orange lines. [Data sources: *Goodliffe, 1995, Martinez and Taylor, 2006, Martinez et al., 2008, Dunn et al., 2009, Escrig et al., 2009*].

EXAMPLES OF ANNOTATED SCRIPTS FOR PROCESSING AND PLOTTING BATHYMETRY AND SIDESCAN DATA

```
### ANNOTATED SCRIPT FOR DEEP-TOWED IMI-120 SIDESCAN AND BATHYMETRY DATA PROCESSING ###

# rtgrid is an HMRG program used to create grids that can be displayed in rtovl for navigational
corrections
rtgrid -ncs 1 -cs 1 -putm -ewgs84 -uz -1 -mca 0 -mftg 10 -acf -v 1

# rtovl is an HMRG program used to overlay and display IMI-120 sidescan and bathymetry data at multiple
scales
# rtovl was primarily used to make navigational corrections to the IMI-120 data, as well as deleting
portions containing bad data
rtovl -nrt -eab -nws 800 800 -sgcd -bsd ~/Lau/KM0804/SS/pfin -bgf ~/Lau/KM0804_dtbg_fin/south/nelsc20-
10r.grd -sgf ~/Lau/KM0804/ship_ss/south/KM0804_ssr.grd -v 1

# bsgrid is another HMRG gridding program used to create grids that can be converted into a GMT grid with
bsovl
bsgrid ~/Lau/KM0804/SS/mosaic/spool/km0804* -bty -cs 5 -putm -ewgs84 -uz -1 -mca 0 -mspd 200 -v 1

# bsovl is another swath display program similar to rtovl. It was only used to convert the data into a GMT
grid
bsovl ss.cf -gf celsc_s.grd -gmr -os -176.283 -20.9833 8325 16650 -v 1

# After converting to a GMT grid, the data was re-projected into geographic coordinates (originally in UTM)
grdproject celsc_s.grd -Gcelsc_sg.grd -Ju-1/1:1 -Mm -I -C

# Create a custom histogram-equalized cpt file with 256 gray levels for each sidescan grid
set name = "celsc_s"
grdhisteq celsc_sg.grd -C255 -D | \
awk 'BEGIN {nnn=255}{printf "%05.1f %03d %03d %03d %05.1f %03d %03d %03d\n",$1,nnn,nnn,nnn,$2,nnn-1,nnn-
1,nnn-1}{nnn-=1}' >! $name.cpt
echo "F 0 0 0" >> $name.cpt
echo "B 255 255 255" >> $name.cpt
echo "N 255 255 255" >> $name.cpt

# For the IMI-120 bathymetry, color cpt files were created using grd2cpt
grd2cpt -E20 $name.grd $R -Cwysiwyg -V -Z >! $name.cpt
```

```
# Apply a basic boxcar filter to bathymetry data to smooth out some of the noise
grdfilter $nameg.grd -D0 -Fb.00016 -G$filt.grd -V
# Plot 2 m sidescan image with GMT, contours are optional
set name = "celsc_s"
set nameg = "celsc_sg"
set cont = "nelsc_ng_mb"
set R = "-R183.8/183.975/-20.25/-19.9148 -JM20i"
gmtset PAPER_MEDIA Custom_22ix42i
gmtset HEADER_FONT_SIZE 14p ANNOT_FONT_SIZE 12p LABEL_FONT_SIZE 12p
grdimage $nameg.grd -C$name.cpt -P $R -V -K -Y1i -Xc -Ba2mg1m >! $name.ps
#grdcontour $cont.grd $R -C.01 -A.05f5to -Z-.001 -Wc.1p,green -Wa.3p,turquoise -Q20 -T.05i/.02i -O -K >>
$name.ps
psbasemap $R -Lfx40/-1/-20/5:km:r -O -K >> $name.ps
psscale -C$name.cpt -D10/-1/15/.3h -Ba200000f25000/:"Relative Intensity": -O -V >> $name.ps
ps2pdf $name.ps >$name.pdf

# Plot 2 m bathymetry image with GMT
set name = "celsc_sb"
set nameg = "celsc_sbf"
set R = "-R183.717/183.875/-20.9833/-20.6817 -JM19.75i"
gmtset PAPER_MEDIA Custom_22ix42i
gmtset HEADER_FONT_SIZE 14p ANNOT_FONT_SIZE 12p
grdgradient $nameg.grd -G$name.grad -A100 -Nt1 -V
grdimage $nameg.grd -I$name.grad -C$name.cpt -P $R -V -K -Y1i -Xc -Ba2mg1m >! $name.ps
grdcontour $nameg.grd $R -C.01 -A.05f5to -Z.001 -Wc.1p -Wa.3p -T.05i/.02i -O -K -Q20 >> $name.ps
psbasemap $R -Lfx40/-1/-21/5:km:r -O -K >> $name.ps
psscale -C$name.cpt -D10/-1/15/.3h -Ba200f50/:"Depth (m)": -O -V >> $name.ps
ps2pdf $name.ps >$name.pdf

## Alternating sidescan swaths for analysis and Adobe Photoshop blending
# First step is to determine the start/end times of each swath using an annotated track plot
# Then edit the ss.cf control file so that every other swath is removed and re-create GMT grid
bsovl ssnx.cf -gf nelsc_sx.grd -gmr -os -176.233 -20.55 10175 21275 -v 1
grdproject nelsc_sx.grd -Gnelsc_sxg.grd -Ju-1/1:1 -Mm -I -C
# Create a new customized cpt using the same code as above
# Then plot the alternating swaths with similar commands to those above
```

```
### EM-120 BATHYMETRY PLOTS OF ENTIRE VFR, CELSC, AND NELSC (~20 M CELL SIZE, OBLIQUE PROJECTION) ###
# Set variables for grid name, range, and raw bis file names
set name = "nelsc_mb"
set R = "-R-176:20/-20:45/-175:45/-19r"
set bis_files = "~/Lau/KM0804_dtbg_fin/km0804-em120-bat-raw_jd*.bis
~/Lau/KM0804_dtbg_fin/km0410_em120_bat.bis ~/Lau/KM0804_dtbg_fin/km0417_bat.bis
~/Lau/KM0804_dtbg_fin/hm9507.bis ~/Lau/MGL0903_EM122/MGL0903_MB_bat.bis"

# Combine .bis data from all 5 cruises with a grid spacing of .0005 degrees (~50 m)
blockmedian $bis_files $R -I.0005 -bis3 -bos3 -F -Q >! median.bis
blockmedian $bis_files $R -I.0005 -bis3 -bos3    -Q >> median.bis

# Nearest neighbor grid from median.bis with ~20 m grid spacing, apply boxcar filter of ~40 m to create
smooth reference grid.
nearneighbor median.bis $R -I.0002 -S.001 -N4 -F -Gref_1.grd  -bis3 -fg -V
grdfilter ref_1.grd -D0 -Fb.0004 -Gref_1.grd -V

# Plot reference grid to see if there are any gaps or major problems
set file = "ref_1"
gmtset PAPER_MEDIA Custom_8ix16i
grdgradient $file.grd -G$file.grad -A100 -Nt1 -V
gmtset D_FORMAT %lg
grdimage $file.grd -I$file.grad -CELSC.cpt -JM6.5i -P -V -Ba10mg5m -K >! $file.ps

# Remove spikes from .bis data using smooth reference grid with a window of +20 m to -5 m
gmtset D_FORMAT %.6f
cat $bis_files | grdtrack -Gref_1.grd -bis3 -S -Q -V -fg | \
awk '{if (($3-$4)<20)&&(($3-$4)>-5)) print $1,$2,$3}' | \
gmtconvert -bos3 >! "$name"_cull_1.bis
end

# Near neighbor grids from de-spiked data, ~20 m cell size, increasing search radii (~100, 200, 300, 400 m)
nearneighbor "$name"_cull_1.bis $R -I.0002 -S.001 -N4 -F -G"$name"_1.grd -bis3 -fg -V
nearneighbor "$name"_cull_1.bis $R -I.0002 -S.002 -N4 -F -G"$name"_2.grd -bis3 -fg -V
nearneighbor "$name"_cull_1.bis $R -I.0002 -S.003 -N4 -F -G"$name"_3.grd -bis3 -fg -V
nearneighbor "$name"_cull_1.bis $R -I.0002 -S.004 -N4 -F -G"$name"_4.grd -bis3 -fg -V

# Overlay grids with smallest search radius on top and largest search radius on bottom to fill gaps
```

```
grdmath "$name"_1.grd "$name"_2.grd AND = "$name".grd
grdmath "$name".grd   "$name"_3.grd AND = "$name".grd
grdmath "$name".grd   "$name"_4.grd AND = "$name".grd

# Filter grids with increasingly narrow boxcar filters (~220 m, 100 m, 60 m) and overlay so highest
resolution grid stays on top
grdfilter $name.grd -D0 -Fb.0022 -Gfilt.grd -V
grdmath $name.grd   filt.grd AND = $name.grd
grdfilter $name.grd -D0 -Fb.0010 -Gfilt.grd -V
grdmath $name.grd   filt.grd AND = $name.grd
grdfilter $name.grd -D0 -Fb.0006 -Gfilt.grd -V
grdmath $name.grd   filt.grd AND = $name.grd

## Bathymetry plots
# Oblique projection bathymetry plot (~20 m cell size) aligned with axial trend showing axis picks and vent
site locations
set name = "nelsc_mb"
set R = "-R-176:20/-20:42/-175:45/-19:10r"
set J = "-JOb-176:2.5/-19:52.5/100/1.2i"
gmtset D_FORMAT %.0f
gmtset PAPER_MEDIA Custom_2.5ix8.75i
gmtset HEADER_FONT_SIZE 14p ANNOT_FONT_SIZE 8p LABEL_FONT_SIZE 8p
grdgradient $name.grd -G$name.grad -A100 -Nt1 -V
grdimage $name.grd -I$name.grad -CELSC.cpt -P $R $J -V -Y1i -X.75i -Ba10mg5mWesN -K >! "$name"_pg.ps
psxy ELSC_VFR_axis.txt $R $J -W1p,red,solid -P -M -O -K >> "$name"_pg.ps
psxy ~/Lau/KM0804/SS/NELSCvents.xy $R $J -Gred -P -O -K -Sa.1i -K >> "$name"_pg.ps
psbasemap $R $J -Lfx0.6i/-.2i/-20/30:km:r -O -K >> "$name"_pg.ps
psscale -CELSC.cpt -D.25i/-.5i/1.5i/.1ih -Ba1000f200/:"Depth (m)": -O -V >> "$name"_pg.ps
ps2pdf "$name"_pg.ps >! "$name"_pg.pdf
# The same series of steps were run for the CELSC and VFR segments as well

# These grids were also used to create bathymetry plots for each of the 6 2nd order segments, example:
set name = "nelsc_mb"
set file = "nelsc_s_mb_obl"
set R = "-R-176:20/-20:42/-175:55/-20:00r"
set J = "-JOb-176:09/-20:21/103/1.2i"
gmtset D_FORMAT %.0f
gmtset PAPER_MEDIA Custom_2.5ix6i
```

```
gmtset HEADER_FONT_SIZE 14p ANNOT_FONT_SIZE 9p LABEL_FONT_SIZE 9p
grdgradient $name.grd -G$name.grad -A100 -Nt1 -V
grdimage $name.grd -I$name.grad -CELSC_axis.cpt -P $R $J -V -Y1i -X.75i -Ba10mg5mWesN -K >! $file.ps
psxy ELSC_VFR_axis.txt $R $J -W1p,red,solid -P -M -O -K >> $file.ps
psxy ~/Lau/KM0804/SS/NELSCvents.xy $R $J -Gred -P -O -K -Sa.1i -K >> $file.ps
psbasemap $R $J -Lfx0.6i/-.2i/-20/20:km:r -O -K >> $file.ps
psscale -CELSC_axis.cpt -D.26i/-.5i/1.69i/.1ih -Ba1000f200/:"Depth (m)": -O -V >> $file.ps
ps2pdf $file.ps >! $file.pdf

### EM-120 SIDESCAN IMAGES OF ENTIRE VFR, CELSC, AND NELSC (~20 M CELL SIZE, OBLIQUE PROJECTION) ###
# Set variable names and ranges for each segment, as well as raw .bis files
set name = (vfr celsc nelsc)
set R = ("-R-177/-23/-176:10/-21:21r" "-R-176:30/-21:30/-176/-20:20r" "-R-176:20/-20:45/-175:45/-19r")
set km0410 = "~/Lau/KM0804/SS/bis/km0410_ss_*.bis"
set km0804 = "~/Lau/KM0804/SS/bis/km0804_ss_*.bis"

# foreach-end loop to combine data from KM0410 and KM0804 cruises and grid at .0002 degrees (~ 20 m)
foreach i (1 2 3)
blockmedian $km0410 $km0804 $R[$i] -I.0002 -C -V -bis3 -bos3 | \
xyz2grd -bis3 $R[$i] -I.0002 -V -G"$name[$i]"_ss_raw.grd
grdfilter "$name[$i]"_ss_raw.grd -D0 -Fb.001 -V -Gclip.grd
grdmath clip.grd 10 - = clip.grd
grdmath "$name[$i]"_ss_raw.grd clip.grd GT = clip.grd
grdclip clip.grd -Sb.5/NaN -Gclip.grd
grdmath "$name[$i]"_ss_raw.grd clip.grd MUL =  "$name[$i]"_ss_raw.grd
# Apply 3 gaussian filters of decreasing width and overlay so that the narrow filter is on top and wider
filters simply fill gaps
grdfilter "$name[$i]"_ss_raw.grd -D0 -Fg.0010 -V -Gfilt.grd
grdmath "$name[$i]"_ss_raw.grd filt.grd AND = "$name[$i]"_ss.grd
grdfilter "$name[$i]"_ss.grd -D0 -Fg.0007 -V -Gfilt.grd
grdmath "$name[$i]"_ss_raw.grd filt.grd AND = "$name[$i]"_ss.grd
grdfilter "$name[$i]"_ss.grd -D0 -Fg.0003 -V -Gfilt.grd
grdmath "$name[$i]"_ss_raw.grd filt.grd AND = "$name[$i]"_ss.grd
# Create a histogram-equalized (equal number of z values for each bin) grayscale cpt file with 51 gray
values
grdhisteq "$name[$i]"_ss.grd -D -C51 | \
awk 'BEGIN {n=255;m=5}{print $1,n,n,n,$2,n-m,n-m,n-m}{n-=m}' >! "$name[$i]"_20ss.cpt
end
```

```
## Sidescan images
# Oblique projection sidescan image (~20 m cell size) aligned with axial trend showing axis picks and vent
site locations
set name = vfr
set R = "-R-177/-22:55/-176:15/-21:26r"
set J = "-JOb-176:35/-22:10/105/1.25i"
gmtset PAPER_MEDIA Custom_2.5ix8.75i
gmtset HEADER_FONT_SIZE 14p ANNOT_FONT_SIZE 8p LABEL_FONT_SIZE 8p
grdimage "$name"_ss.grd -C"$name"_20ss.cpt -P $R $J -V -Y1i -X0.5i -Ba10mg5mwEsN -K >! "$name"_ss_pg.ps
psxy ELSC_VFR_axis.txt $R $J -W1p,red,solid -P -M -O -K >> "$name"_ss_pg.ps
psxy ~/Lau/KM0804/SS/VFRvents.xy $R $J -Gred -P -O -K -Sa.1i -K >> "$name"_ss_pg.ps
psbasemap $R $J -Lfx0.6i/-.2i/-22/30:km:r -O -K >> "$name"_ss_pg.ps
psscale -C"$name"_20ss.cpt -D.25i/-.5i/1i/.1ih -Ba20f10/:"Relative Intensity": -O -V >> "$name"_ss_pg.ps
ps2pdf "$name"_ss_pg.ps >! "$name"_ss_pg.pdf
# The same series of steps were run for the CELSC and NELSC segments as well

# These grids were also used to create sidescan images for each of the 6 2nd order segments, here is an
example:
set name = vfr
set file = "vfr_n_ss_obl"
set R = "-R-176:44/-22:15/-176:17/-21:25r"
set J = "-JOb-176:31/-21:50/103/1.2i"
gmtset D_FORMAT %.0f
gmtset PAPER_MEDIA Custom_2.5ix7i
gmtset HEADER_FONT_SIZE 14p ANNOT_FONT_SIZE 9p LABEL_FONT_SIZE 9p
grdimage "$name"_ss.grd -C"$name"_20ss.cpt -P $R $J -V -Y1i -X.5i -Ba10mg5mwEsN -K >! $file.ps
psxy ELSC_VFR_axis.txt $R $J -W1p,red,solid -P -M -O -K >> $file.ps
psxy ~/Lau/KM0804/SS/VFRvents.xy $R $J -Gred -P -O -K -Sa.1i -K >> $file.ps
psbasemap $R $J -Lfx0.6i/-.2i/-21.75/20:km:r -O -K >> $file.ps
psscale -C"$name"_20ss.cpt -D.25i/-.5i/1i/.1ih -Ba40f10/:"Relative Intensity": -O -V >> $file.ps
ps2pdf $file.ps >! $file.pdf

### BATHYMETRY PLOTS FOR ALL 6 2ND ORDER SEGMENTS (~10 M CELL SIZE) ###
# Steps for creating 10 m grids are very similar to those for the oblique 20 m grids
set R = "-R-176.25/-176.092/-20.7833/-20.4315"
```

```
set bis_files = "~/Lau/KM0804_dtbg_fin/km0804-em120-bat-raw_jd*.bis
~/Lau/KM0804_dtbg_fin/km0410_em120_bat.bis ~/Lau/KM0804_dtbg_fin/km0417_bat.bis
~/Lau/KM0804_dtbg_fin/hm9507.bis ~/Lau/MGL0903_EM122/MGL0903_MB_bat.bis"
blockmedian $bis_files $R -I.0005 -bis3 -bos3 -F -Q -V >! median.bis
blockmedian $bis_files $R -I.0005 -bis3 -bos3    -Q -V >> median.bis

nearneighbor median.bis $R -I.0001 -S.001 -N4 -F -Gref_1.grd  -bis3 -fg -V
grdfilter ref_1.grd -D0 -Fb.0002 -Gref_1.grd -V

set file = "ref_1"
gmtset PAPER_MEDIA Custom_8ix16i
grdgradient $file.grd -G$file.grad -A100 -Nt1 -V
gmtset D_FORMAT %lg
grdimage $file.grd -I$file.grad -Cn_elsc_em120_bathy.cpt -JM6i -P -V -Ba2mg1m -K >! $file.ps
gv $file.ps

gmtset D_FORMAT %.6f
cat $bis_files | grdtrack -Gref_1.grd -bis3 -S -Q -V -fg | \
awk '{if (((($3-$4)<20)&&(($3-$4)>-5)) print $1,$2,$3}' | \
gmtconvert -bos3 -V >! celsc_ng_mb_cull_1.bis
end

nearneighbor celsc_ng_mb_cull_1.bis $R -I.0001 -S.001 -N4 -F -Gcelsc_ng_mb_1.grd -bis3 -fg -V
nearneighbor celsc_ng_mb_cull_1.bis $R -I.0001 -S.002 -N4 -F -Gcelsc_ng_mb_2.grd -bis3 -fg -V
nearneighbor celsc_ng_mb_cull_1.bis $R -I.0001 -S.003 -N4 -F -Gcelsc_ng_mb_3.grd -bis3 -fg -V
nearneighbor celsc_ng_mb_cull_1.bis $R -I.0001 -S.004 -N4 -F -Gcelsc_ng_mb_4.grd -bis3 -fg -V

grdmath celsc_ng_mb_1.grd celsc_ng_mb_2.grd AND = celsc_ng_mb.grd
grdmath celsc_ng_mb.grd   celsc_ng_mb_3.grd AND = celsc_ng_mb.grd
grdmath celsc_ng_mb.grd   celsc_ng_mb_4.grd AND = celsc_ng_mb.grd
grdfilter celsc_ng_mb.grd -D0 -Fb.0005 -Gcelsc_ng_mb.grd -V

grd2cpt -E20 celsc_ng_mb.grd $R -Cwysiwyg -V -Z >! celsc_ng_mb.cpt

## Bathymetry plot (~10 m cell size), large format for mapping and analysis
gmtset D_FORMAT %lg
set file = "celsc_ng_mb"
set R = "-R183.75/183.908/-20.7833/-20.4315 -JM17i"
```

```
gmtset PAPER_MEDIA Custom_19ix42i
gmtset HEADER_FONT_SIZE 14p ANNOT_FONT_SIZE 12p LABEL_FONT_SIZE 12p
grdgradient $file.grd -G$file.grad -A100 -Nt1 -V
grdimage $file.grd -I$file.grad -C$file.cpt -Ba2mg1m $R -P -Xc -V -K >! $file.ps
grdcontour $file.grd $R -C.01 -A.05f5to -Z.001 -Wc.1p -Wa.3p -Q20 -T.05i/.02i -O -K >> $file.ps
psscale -C$file.cpt -D10/-1/15/.3h -Ba200f50/:"Depth (m)": -O -K >> $file.ps
psbasemap $R -Lfx36/-1/-20/5:km:r -O >> $file.ps
ps2pdf $file.ps >! $file.pdf

### EM-120 SIDESCAN IMAGES FOR ALL 6 2ND ORDER SEGMENTS (~10 M CELL SIZE) ###
# Create .0001 degree (~10 m) sidescan grids, very similar to code for ~20 m oblique grids
set name = (nelsc_n nelsc_s celsc_n celsc_s vfr_n vfr_s)
set R = ("-R-176.2/-176.025/-20.25/-19.9148" "-R-176.233/-176.04/-20.55/-20.1646" "-R-176.25/-176.092/-
20.7833/-20.4315" "-R-176.283/-176.125/-20.9833/-20.6817" "-R-176.667/-176.488/-22.25/-21.8818" "-R-
176.717/-176.556/-22.4/-22.1155")
set km0410 = "/home/tofua/martinez/PROJECTS/LAU/KM0410/EM120/km0410_ss_*.bis"
set km0804 = "/home/tofua/martinez/PROJECTS/LAU/KM0804/EM120/RAW/BIS_FILES/km0804_ss_*.bis"
set cpt = ss_pos.cpt
foreach i (1 2 3 4 5 6)
blockmedian $km0410 $km0804 $R[$i] -I.0001 -C -V -bis3 -bos3 | \
xyz2grd -bis3 $R[$i] -I.0001 -V -G"$name[$i]"_ss_raw.grd
grdfilter "$name[$i]"_ss_raw.grd -D0 -Fb.001 -V -Gclip.grd
grdmath clip.grd 10 - = clip.grd
grdmath "$name[$i]"_ss_raw.grd clip.grd GT = clip.grd
grdclip clip.grd -Sb.5/NaN -Gclip.grd
grdmath "$name[$i]"_ss_raw.grd clip.grd MUL =  "$name[$i]"_ss_raw.grd
grdfilter "$name[$i]"_ss_raw.grd -D0 -Fg.0010 -V -Gfilt.grd
grdmath "$name[$i]"_ss_raw.grd filt.grd AND = "$name[$i]"_ss.grd
grdfilter "$name[$i]"_ss.grd -D0 -Fg.0007 -V -Gfilt.grd
grdmath "$name[$i]"_ss_raw.grd filt.grd AND = "$name[$i]"_ss.grd
grdfilter "$name[$i]"_ss.grd -D0 -Fg.0003 -V -Gfilt.grd
grdmath "$name[$i]"_ss_raw.grd filt.grd AND = "$name[$i]"_ss.grd
grdhisteq "$name[$i]"_ss.grd -D -C51 | \
awk 'BEGIN {n=255;m=5}{print $1,n,n,n,$2,n-m,n-m,n-m}{n-=m}' >! "$name[$i]"_10ss.cpt
end

## Sidescan image (~10 m cell size), large format for mapping and analysis, contours optional
set name = "celsc_n_10ss"
```

```
set nameg = "celsc_n_ss"
#set cont = "celsc_ng_mb"
set R = "-R-176.25/-176.092/-20.7833/-20.4315 -JM17i"
gmtset PAPER_MEDIA Custom_19ix42i
gmtset HEADER_FONT_SIZE 14p ANNOT_FONT_SIZE 12p LABEL_FONT_SIZE 12p
grdimage $nameg.grd -C$name.cpt -P $R -V -K -Y1i -Xc -Ba2mg1m >! $name.ps
#grdcontour $cont.grd $R -C.01 -A.05f5to+kturquoise+s6 -Z.001 -Wc.25p,green -Wa.5p,turquoise -Q50 -
T.05i/.02i -O -K >> $name.ps
psxy ELSC_VFR_axis.txt $R -W3p,red,solid -P -M -K -O >> $name.ps
psxy ~/Lau/KM0804/SS/NELSCvents.xy $R -Gred -P -O -Sa.3i -K >> $name.ps
psbasemap $R -Lfx36c/-1c/-20/5:km:r -O -K >> $name.ps
psscale -C$name.cpt -D10c/-1c/15c/.3ch -Ba200000f25000/:"Relative Intensity": -O -V >> $name.ps
ps2pdf $name.ps >! $name.pdf

### EXAMPLE SCRIPTS FOR DETAIL PLOTS ALONG CELSC-N (10 m bty, 10 m ss, 2 m bty, 2 m ss) ###
## 10 m BTY 4'x4' plots of detail areas
#set name = "celsc_n_detail_10mb"
set name = "celsc_n_sdetail_10mb"
set grid = "celsc_ng_mb"
set cpt = "celsc_ng_mb.cpt"
#set R = "-R-176:11/-176:7/-20:33/-20:29 -JM6i"
set R = "-R-176:13/-176:9/-20:42/-20:38 -JM6i"
gmtset D_FORMAT %.0f
gmtset PAPER_MEDIA Custom_8ix10i
gmtset HEADER_FONT_SIZE 14p ANNOT_FONT_SIZE 12p LABEL_FONT_SIZE 12p
grdgradient $grid.grd -G$grid.grad -A100 -Nt1 -V
grdimage $grid.grd -I$grid.grad -C$cpt -P $R -Y2i -Xc -Ba2mg1m -V -K >! $name.ps
grdcontour $grid.grd $R -C.01 -A.05f5to -Z.001 -Wc.1p -Wa.3p -Q20 -T.03i/.01i -O -K >> $name.ps
psxy ELSC_VFR_axis.txt $R -Wthick,red,solid -P -M -O -K >> $name.ps
psxy NELSCvents.xy $R -Gred -P -O -K -Sa.2i -K >> $name.ps
psbasemap $R -Lfx13c/-1i/-20.5/2:km:r -O -K >> $name.ps
psscale -C$cpt -D3c/-1i/8c/.2ch -Ba200f50/:"Depth (m)": -O -V >> $name.ps
ps2pdf $name.ps >! $name.pdf

## 10 m SS: 4'x4' plots of detail areas
#set name = "celsc_n_detail_10mss"
set name = "celsc_n_sdetail_10mss"
set grid = "celsc_ss"
```

```
set cpt = "celsc_n_10ss.cpt"
#set R = "-R-176:11/-176:7/-20:33/-20:29 -JM6i"
set R = "-R-176:13/-176:9/-20:42/-20:38 -JM6i"
gmtset PAPER_MEDIA Custom_8ix10i
gmtset HEADER_FONT_SIZE 14p ANNOT_FONT_SIZE 12p LABEL_FONT_SIZE 12p
grdimage $grid.grd -C$cpt -P $R -Y2i -Xc -Ba2mg1m -V -K >! $name.ps
psxy ELSC_VFR_axis.txt $R -Wthick,red,solid -P -M -O -K >> $name.ps
psxy NELSCvents.xy $R -Gred -P -O -K -Sa.2i -K >> $name.ps
psbasemap $R -Lfx13c/-1i/-20.5/2:km:r -O -K >> $name.ps
psscale -C$cpt -D2c/-1i/7c/.2ch -Ba200000f50000/:"Relative Intensity": -O -V >> $name.ps
ps2pdf $name.ps >! $name.pdf

## 2 m SS: 4'x4' plots of detail areas
#set name = "celsc_n_detail_2mss"
set name = "celsc_n_sdetail_2mss"
set grid = "~/Lau/KM0804/SS/mosaic/2-ss/segments/celsc_ng.grd"
set cpt = "celsc_n.cpt"
#set R = "-R-176:11/-176:7/-20:33/-20:29 -JM6i"
set R = "-R-176:13/-176:9/-20:42/-20:38 -JM6i"
gmtset PAPER_MEDIA Custom_8ix10i
gmtset HEADER_FONT_SIZE 14p ANNOT_FONT_SIZE 12p LABEL_FONT_SIZE 12p
grdimage $grid -C$cpt -P $R -Y2i -Xc -Ba2mg1m -V -K >! $name.ps
psxy ELSC_VFR_axis.txt $R -Wthick,red,solid -P -M -O -K >> $name.ps
psxy NELSCvents.xy $R -Gred -P -O -K -Sa.2i -K >> $name.ps
psbasemap $R -Lfx13c/-1i/-20.5/2:km:r -O -K >> $name.ps
psscale -C$cpt -D2c/-1i/7c/.2ch -Ba200000f25000/:"Relative Intensity": -O -V >> $name.ps
ps2pdf $name.ps >! $name.pdf

## Alternating swaths (outside)
#set name = "celsc_n_detail_2mss_altx"
set name = "celsc_n_sdetail_2mss_altx"
set grid = "~/Lau/KM0804/SS/mosaic/2-ss/alt_segments/celsc_nxg.grd"
set cpt = "celsc_n.cpt"
#set R = "-R-176:11/-176:7/-20:33/-20:29 -JM6i"
set R = "-R-176:13/-176:9/-20:42/-20:38 -JM6i"
gmtset PAPER_MEDIA Custom_8ix10i
gmtset HEADER_FONT_SIZE 14p ANNOT_FONT_SIZE 12p LABEL_FONT_SIZE 12p
grdimage $grid -C$cpt -P $R -Y2i -Xc -Ba2mg1m -V -K >! $name.ps
```

```
psxy ELSC_VFR_axis.txt $R -Wthick,red,solid -P -M -O -K >> $name.ps
psxy NELSCvents.xy $R -Gred -P -O -K -Sa.2i -K >> $name.ps
psbasemap $R -Lfx13c/-1i/-20.5/2:km:r -O -K >> $name.ps
psscale -C$cpt -D2c/-1i/7c/.2ch -Ba200000f25000/:"Relative Intensity": -O -V >> $name.ps
ps2pdf $name.ps >! $name.pdf

## Alternating swaths (inside)
#set name = "celsc_n_detail_2mss_alty"
set name = "celsc_n_sdetail_2mss_alty"
set grid = "~/Lau/KM0804/SS/mosaic/2-ss/alt_segments/celsc_nyg.grd"
set cpt = "celsc_n.cpt"
#set R = "-R-176:11/-176:7/-20:33/-20:29 -JM6i"
set R = "-R-176:13/-176:9/-20:42/-20:38 -JM6i"
gmtset PAPER_MEDIA Custom_8ix10i
gmtset HEADER_FONT_SIZE 14p ANNOT_FONT_SIZE 12p LABEL_FONT_SIZE 12p
grdimage $grid -C$cpt -P $R -Y2i -Xc -Ba2mg1m -V -K >! $name.ps
psxy ELSC_VFR_axis.txt $R -Wthick,red,solid -P -M -O -K >> $name.ps
psxy NELSCvents.xy $R -Gred -P -O -K -Sa.2i -K >> $name.ps
psbasemap $R -Lfx13c/-1i/-20.5/2:km:r -O -K >> $name.ps
psscale -C$cpt -D2c/-1i/7c/.2ch -Ba200000f25000/:"Relative Intensity": -O -V >> $name.ps
ps2pdf $name.ps >! $name.pdf

## 2 m BTY plots of detail areas
set name = "celsc_n_detail_2mb"
#set name = "celsc_n_sdetail_2mb"
set cpt = "celsc_ng_mb.cpt"
set grid = "~/Lau/KM0804/SS/mosaic/2-bty/celsc_nb/celsc_nbf.grd"
set grad = "celsc_nb.grad"
set R = "-R-176:11/-176:7/-20:33/-20:29 -JM6i"
#set R = "-R-176:13/-176:9/-20:42/-20:38 -JM6i"
gmtset PAPER_MEDIA Custom_8ix10i
gmtset HEADER_FONT_SIZE 14p ANNOT_FONT_SIZE 12p LABEL_FONT_SIZE 12p
grdimage $grid -I$grad -C$cpt -P $R -Y2i -Xc -Ba2mg1m -V -K >! $name.ps
grdcontour $grid $R -C.01 -A.05f5to -Z.001 -Wc.1p -Wa.3p -Q20 -T.03i/.01i -O -K >> $name.ps
psxy ELSC_VFR_axis.txt $R -Wthick,red,solid -P -M -O -K >> $name.ps
psxy NELSCvents.xy $R -Gred -P -O -K -Sa.2i -K >> $name.ps
psbasemap $R -Lfx13c/-1i/-20.5/2:km:r -O -K >> $name.ps
psscale -C$cpt -D3c/-1i/8c/.2ch -Ba200f50/:"Depth (m)": -O -V >> $name.ps
```

```
ps2pdf $name.ps >! $name.pdf

### SUMMARY PLOT SHOWING 206Pb/204Pb RATIOS, WITH LINEAR AND POLYNOMIAL TRENDS, ENTIRE ELSC/VFR ###
# Values north of 20.6 S have been removed since they don't follow the same trend
sort -n elsc_vfr_pb_inch1.xy >! elsc_vfr_pb_inch_sort.xy
gmtset D_FORMAT %.8f
# 10th order robust polynomial fit
trend1d -Fxm -N10r elsc_vfr_pb_inch_sort.xy -V >! elsc_vfr_pb_trend.xy
# 2nd order (linear) best fit
trend1d -Fxm -N2 elsc_vfr_pb_inch_sort.xy -V >! elsc_vfr_pb_trend1.xy
awk '{print $2, $1}' elsc_vfr_pb_trend.xy >! elsc_vfr_pb_trend.txt
awk '{print $2, $1}' elsc_vfr_pb_trend1.xy >! elsc_vfr_pb_trend1.txt
# Split up elsc_vfr_pb_inch.xy into separate files for Escrig samples and Jenner/Vallier/Peate samples
*_esc.xy and *_oth.xy

# Plot Pb ratios at same scale to overlay onto smoothed profile
set J = "-JX6i/10i"
gmtset D_FORMAT %.1f
gmtset PAPER_MEDIA Custom_8ix12i
psbasemap -R18.0/18.8/-22:55/-19:10 $J -Ba.1f.1g.1:"206Pb/204Pb Ratios":/a30mg10mwESn -Y1i -P -K >!
elsc_vfr_axis_profile_filt_pb.ps
psxy elsc_vfr_pb_inch_esc.xy -R18.1/18.8/0/10 $J -Ggreen -St.2i -O -K >> elsc_vfr_axis_profile_filt_pb.ps
psxy elsc_vfr_pb_inch_oth.xy -R18.1/18.8/0/10 $J -Glightblue -Sc.15i -O -K >>
elsc_vfr_axis_profile_filt_pb.ps
psxy elsc_vfr_pb_trend.txt -R18.1/18.8/0/10 $J -W1p,red,solid -O -K >> elsc_vfr_axis_profile_filt_pb.ps
psxy elsc_vfr_pb_trend1.txt -R18.1/18.8/0/10 $J -W1p,blue,- -O >> elsc_vfr_axis_profile_filt_pb.ps
ps2pdf elsc_vfr_axis_profile_filt_pb.ps >! elsc_vfr_axis_profile_filt_pb.pdf

### ALONG-AXIS PROFILE AND 206Pb/204Pb PLOTS, EXAMPLE FROM VFR ###
## The first step is to pick evenly spaced (~50 m) points along the spreading axis
gmtset D_FORMAT %.8f
sample1d ELSC_VFR_axis.txt -Fa -T1 -M -I.0005 -S-19.36666666 -fg -V >! elsc_vfr_axis_pts.txt
# Divide into _pts files for each of six segments

## VFR-N along-axis profile
set R = "-R-176:44/-22:15/-176:17/-21:25r"
set J = "-JX3i/10i"
gmtset D_FORMAT %.8f
```

```
# grdtrack picks depths from the bty grid at each point along the axis
grdtrack vfr_n_pts.txt -Gvfr_mb.grd $R -M -fg -V >! vfr_n_axis_prof.xyz
# project latitude values to inches for plotting
mapproject vfr_n_axis_prof.xyz $R $J -Di -M -V >! vfr_n_axis_prof_inch.xy
awk '{print $3, $2}' vfr_n_axis_prof_inch.xy >! vfr_n_depth_lat.xy
# Make sure to add > separators after the awk step
# Plot along-axis profile
set name = "vfr_n_axis_profile"
set R = "-R-176:44/-22:15/-176:17/-21:25r"
set J = "-JX3i/10i"
gmtset D_FORMAT %.0f
gmtset PAPER_MEDIA Custom_5ix12i
psbasemap -R-2100/-1500/-22:15/-21:25 $J -Ba500f50g50:Depth:/a10mg5mwESn -P -K >! $name.ps
psxy vfr_n_depth_lat.xy -R-2100/-1500/0/10 $J -W1p,black,solid -M -V -P -O >> $name.ps
ps2pdf $name.ps >! $name.pdf
# The color gradients seen on some of these profiles was create with Adobe Photoshop

## Smoothed profile of entire VFR
# Make lat values positive temporarily in vfr_depth_lat.xy so filter1d can read it
# Change latitude to first column so it can be sorted and filter1d can handle it
gmtset D_FORMAT %.8f
awk '{print $2, $1}' vfr_depth_lat_100.xy >! vfr_lat_depth_100.xy
# Fix > separators and split into files for each segment

# Sort so latitude inches are descending
sort -n vfr_s5_lat_depth_100.xy >! vfr_s5_inch_depth_100.txt
sort -n vfr_s4_lat_depth_100.xy >! vfr_s4_inch_depth_100.txt
sort -n vfr_s3_lat_depth_100.xy >! vfr_s3_inch_depth_100.txt
sort -n vfr_s2_lat_depth_100.xy >! vfr_s2_inch_depth_100.txt
sort -n vfr_s1_lat_depth_100.xy >! vfr_s1_inch_depth_100.txt
sort -n vfr_n_lat_depth_100.xy >! vfr_n_inch_depth_100.txt

# Break down vfr_lat_depth_100.xy into individual segments so lat values constantly decrease, filter
separately and recombine
gmtset D_FORMAT %.8f
filter1d vfr_s5_inch_depth_100.txt -Fg.6 -E -N2/0 -T1.14601157/2.07640454/.03 -V >!
vfr_axis_inch_filt_100.xy
printf ">" >> vfr_axis_inch_filt_100.xy
```

```
filter1d vfr_s4_inch_depth_100.txt -Fg.6 -E -N2/0 -T2.04269667/3.10786521/.03 -V >>
vfr_axis_inch_filt_100.xy
printf ">" >> vfr_axis_inch_filt_100.xy
filter1d vfr_s3_inch_depth_100.txt -Fg.6 -E -N2/0 -T2.89887645/3.65393263/.03 -V >>
vfr_axis_inch_filt_100.xy
printf ">" >> vfr_axis_inch_filt_100.xy
filter1d vfr_s2_inch_depth_100.txt -Fg.5 -E -N2/0 -T3.53932589/4.07191016/.03 -V >>
vfr_axis_inch_filt_100.xy
printf ">" >> vfr_axis_inch_filt_100.xy
filter1d vfr_s1_inch_depth_100.txt -Fg.6 -E -N2/0 -T4.00449443/5.04943825/.03 -V >>
vfr_axis_inch_filt_100.xy
printf ">" >> vfr_axis_inch_filt_100.xy
filter1d vfr_n_inch_depth_100.txt -Fg.6 -E -N2/0 -T4.59775285/9.99775285/.03 -V >>
vfr_axis_inch_filt_100.xy

# Switch the order of the columns back to depth/inch for plotting
awk '{print $2, $1}' vfr_axis_inch_filt_100.xy >! vfr_axis_inch_filt_100.txt
# Fix > separators

# Plot filtered axial profile
set J = "-JX3i/10i"
gmtset D_FORMAT %.0f
gmtset PAPER_MEDIA Custom_5ix12i
psbasemap -R-2500/-1500/-22:55/-21:26 $J -Ba500f100g100:Depth:/a20mg5mwESn -Y1i -P -K >!
vfr_axis_profile_filt_100.ps
psxy vfr_axis_inch_filt_100.txt -R-2500/-1500/0/10 $J -W1p,black,solid -M -V -P -O -K >>
vfr_axis_profile_filt_100.ps
ps2pdf vfr_axis_profile_filt_100.ps >! vfr_axis_profile_filt_100.pdf

## Plot 206Pb/204Pb values and trend lines to overlay on profiles
# Project Pb sample latitudes to inches
set R = "-R-177/-22:55/-176:15/-21:26r"
set J = "-JX1i/10i"
gmtset D_FORMAT %.8f
mapproject Pb206_pts.txt $R $J -S -Di -V >! vfr_pb_inch.txt
awk '{print $2, $3}' vfr_pb_inch.txt >! vfr_pb_inch.xy
awk '{print $3, $2}' vfr_pb_inch.txt >! vfr_pb_inch1.xy
```

```
# Re-scale Pb trend along entire VFR axis for just the VFR-N
# Find inch values that correspond to ends of VFR-N
gmtset D_FORMAT %.8f
set R = "-R-177/-22:55/-176:15/-21:26r"
set J = "-JX3i/10i"
mapproject $J $R
-22:15 = 4.49438202
-21:25 = 10.11235955
# Re-project VFR-N ends to 0 and 10 inches
gmtset D_FORMAT %.8f
mapproject vfr_pb_trend_final.txt -R18.5/18.8/4.49438202/10.11235955 $J -Di -S -V >!
vfr_n_pb_trend_final.txt

# Re-project Pb points to same scales as above
set J = "-JX3i/10i"
gmtset D_FORMAT %.8f
mapproject vfr_pb_inch1.xy -R18.5/18.8/4.49438202/10.11235955 $J -Di -S -V >! vfr_n_pb_inch.txt
mapproject vfr_pb_inch_oth.xy -R18.5/18.8/4.49438202/10.11235955 $J -Di -S -V >! vfr_n_pb_inch_oth.txt
# Manually combine appropriate Pb values (1st col) and inches (2nd col) to make _pb_inch_(oth)_final.txt

# Plot Pb ratios at same scale to overlay onto smoothed profile (VFR-N)
set J = "-JX3i/10i"
set name = "vfr_n_pb_trend"
gmtset D_FORMAT %.0f
gmtset PAPER_MEDIA Custom_5ix12i
gmtset D_FORMAT %.2f
psbasemap -R18.51/18.69/-22:15/-21:25 $J -Ba.06f.015:Pb206/204:/a10mg5mwESn -Y1i -P -K >! $name.ps
gmtset D_FORMAT %.0f
psxy vfr_n_pb_inch_final.txt -R18.51/18.69/0/10 $J -Ggreen -St.2i -O -K >> $name.ps
psxy vfr_n_pb_inch_oth_final.txt -R18.51/18.69/0/10 $J -Glightblue -Sc.15i -O -K >> $name.ps
psxy vfr_n_pb_trend_final.txt -R18.51/18.69/0/10 $J -W1p,red,solid -O >> $name.ps
ps2pdf $name.ps >! $name.pdf

## Example of close-up along-axis profile for vfr_s abrupt morphologic transition zone
set R = "-R-176:42/-176:35/-22:22/-22:14"
set J = "-JX2i/10i"
gmtset D_FORMAT %.8f
# Sample axis at .0002 degrees (~20 m) for higher resolution on profile
```

```
sample1d vfr_s_axis_final.txt -Fa -T1 -M -I.0002 -S-22.23333333 -fg -V >! vfr_s_abrupt_pts.txt
grdtrack vfr_s_abrupt_pts.txt -Gvfr_mb.grd $R -fg -V >! vfr_s_abrupt_prof.xyz
mapproject vfr_s_abrupt_prof.xyz $R $J -Di -M -V >! vfr_s_abrupt_inch.xy
awk '{print $3, $2}' vfr_s_abrupt_inch.xy >! vfr_s_abrupt_dep_lat.xy
# Make sure to add > separators after the awk step
gmtset D_FORMAT %.0f
gmtset PAPER_MEDIA Custom_4ix12i
psbasemap -R-2000/-1500/-22:22/-22:14 $J -Ba500f50g50:Depth:/a5mg1mwESn -P -K >! vfr_s_abrupt_profile.ps
psxy vfr_s_abrupt_dep_lat.xy -R-2000/-1500/0/10 $J -W1p,black,solid -M -V -P -O >> vfr_s_abrupt_profile.ps
ps2pdf vfr_s_abrupt_profile.ps >! vfr_s_abrupt_profile.pdf

### ACROSS-AXIS PROFILES FOR EACH 2ND ORDER SEGMENT, EXAMPLE FROM CELSC-S ###
# CELSC-S
gmtset D_FORMAT %4.8f
# sample1d is picking points every .0333 degrees (2 minutes) along the axis
sample1d celsc_s_axis_fin.txt -Fa -T1 -M -I.033333333 -S-20.71666666 -fg -V >! celsc_s_pts.txt
# Create profile lines centered on axis using sample1d points as center points (-C)
# Profiles are perpendicular to axis (-A), extend 4 km off-axis (-L), point spacing is 20 m (-G)
project -C183.81375979/-20.75000000 -A103 -Q -G.02 -L-4/4 >! celsc_s_profiles.xy
project -C183.80617914/-20.78333333 -A104 -Q -G.02 -L-4/4 >> celsc_s_profiles.xy
project -C183.79833704/-20.81666666 -A104 -Q -G.02 -L-4/4 >> celsc_s_profiles.xy
project -C183.79095549/-20.85000000 -A104 -Q -G.02 -L-4/4 >> celsc_s_profiles.xy
project -C183.78397182/-20.88333333 -A105 -Q -G.02 -L-4/4 >> celsc_s_profiles.xy
project -C183.77589748/-20.91666666 -A105 -Q -G.02 -L-4/4 >> celsc_s_profiles.xy
project -C183.76599494/-20.95000000 -A105 -Q -G.02 -L-4/4 >> celsc_s_profiles.xy
project -C183.75333525/-20.98333333 -A105 -Q -G.02 -L-4/4 >> celsc_s_profiles.xy
project -C183.74068451/-21.01666666 -A105 -Q -G.02 -L-4/4 >> celsc_s_profiles.xy
project -C183.72869968/-21.05000000 -A105 -Q -G.02 -L-4/4 >> celsc_s_profiles.xy
project -C183.71640241/-21.08333333 -A105 -Q -G.02 -L-4/4 >> celsc_s_profiles.xy
project -C183.70211673/-21.11666666 -A105 -Q -G.02 -L-4/4 >> celsc_s_profiles.xy
project -C183.68954937/-21.15000000 -A105 -Q -G.02 -L-4/4 >> celsc_s_profiles.xy
project -C183.67821882/-21.18333333 -A105 -Q -G.02 -L-4/4 >> celsc_s_profiles.xy
project -C183.66755343/-21.21666666 -A105 -Q -G.02 -L-4/4 >> celsc_s_profiles.xy
project -C183.65671868/-21.25000000 -A104 -Q -G.02 -L-4/4 >> celsc_s_profiles.xy
project -C183.64889550/-21.28333333 -A104 -Q -G.02 -L-4/4 >> celsc_s_profiles.xy
project -C183.63991606/-21.31666666 -A104 -Q -G.02 -L-4/4 >> celsc_s_profiles.xy
project -C183.63197859/-21.35000000 -A103 -Q -G.02 -L-4/4 >> celsc_s_profiles.xy
project -C183.62247324/-21.38333333 -A103 -Q -G.02 -L-4/4 >> celsc_s_profiles.xy
```

```
project -C183.61697811/-21.41666666 -A101 -Q -G.02 -L-4/4 >> celsc_s_profiles.xy
# Pick depths from the bathymetry grid along each of the above profiles
grdtrack celsc_s_profiles.xy -Gcelsc_mb.grd -R-176.5/-176/-21.53333333/-20.3 -M -fg -V >!
celsc_s_profiles.txt
# Add separators (>) between each profile in .txt file and rename as .xyz file

# PLOT profile lines on celsc_mb oblique bathymetry plot
set name = "celsc_mb"
set R = "-R-176:30/-21:28/-176/-20:22r"
set J = "-JOb-176:15/-20:55/100/1.35i"
gmtset D_FORMAT %.0f
gmtset PAPER_MEDIA Custom_2.5ix7.75i
gmtset HEADER_FONT_SIZE 14p ANNOT_FONT_SIZE 8p LABEL_FONT_SIZE 8p
grdimage $name.grd -I$name.grad -CELSC_axis.cpt -P $R $J -V -Y1i -X.75i -Ba10mg5mWesN -K >!
"$name"_obl_prof.ps
psxy ELSC_VFR_axis.txt $R $J -W0.5p,red,solid -P -m -O -K >> "$name"_obl_prof.ps
psxy ~/Lau/KM0804/SS/VFRvents.xy $R $J -Gred -P -O -Sa.1i -K >> "$name"_obl_prof.ps
psxy ~/Lau/KM0804/SS/NELSCvents.xy $R $J -Gred -P -O -Sa.1i -K >> "$name"_obl_prof.ps
psxy celsc_n_profiles_alt_fin.xyz $R $J -W0.5p,magenta,solid -P -M -O -K >> "$name"_obl_prof.ps
psxy celsc_s_profiles_fin.xyz $R $J -W0.5p,magenta,solid -P -M -O -K >> "$name"_obl_prof.ps
psbasemap $R $J -Lfx0.6i/-.2i/-21/30+lkm+jr -O -K >> "$name"_obl_prof.ps
psscale -CELSC_axis.cpt -D.25i/-.5i/1.5i/.1ih -O -V -Ba1000f200:Depth: >> "$name"_obl_prof.ps
ps2pdf "$name"_obl_prof.ps >! "$name"_obl_prof.pdf

# Use awk to create 2-column text file with distance from axis (x) and depth (y)
awk '{print $3, $4}' celsc_s_profiles.xyz >! celsc_dist_depth.xy
# Then split the "_dist_depth" file into individual profile ".xy" files

# PLOT individual profiles with psxy (CELSC-S)
foreach i (1 2 3 4 5 6 7 8 9 10 11 12 13 14 15 16 17 18 19 20 21)
set name = (celsc_s_20.75 celsc_s_20.78 celsc_s_20.81 celsc_s_20.85 celsc_s_20.88 celsc_s_20.91
celsc_s_20.95 celsc_s_20.98 celsc_s_21.01 celsc_s_21.05 celsc_s_21.08 celsc_s_21.11 celsc_s_21.15
celsc_s_21.18 celsc_s_21.21 celsc_s_21.25 celsc_s_21.28 celsc_s_21.31 celsc_s_21.35 celsc_s_21.38
celsc_s_21.41)
set J = "-JX8i/3i"
set R = "-R-4/4/-3000/-1500"
gmtset D_FORMAT %.0f
gmtset PAPER_MEDIA Custom_10ix5i
```

```
gmtset PAGE_ORIENTATION portrait
psxy "$name[$i]".xy $R $J -Ba2f0.5:"km":/a500f100:"Depth (m)":WESn -M -W1p,black,solid -V >!
"$name[$i]"_ng.ps
ps2pdf "$name[$i]"_ng.ps >! "$name[$i]"_ng.pdf
end
# Profiles were then imported into photoshop for stacking and creating gradients for final figures

### COMPILED BATHYMETRY PLOTS FOR ELSC/VFR AND ENTIRE LAU BASIN ###
# Both of these are using a compiled bathymetry grid from all cruises in the Lau basin
# ELSC/VFR bathymetry plot
set name = "ELSC_01_10_mb"
set file = "Lau_bathymetry_01_11"
set R = "-R-177/-175/-23/-19 -JM6i"
gmtset PAPER_MEDIA Custom_8ix15i
gmtset HEADER_FONT_SIZE 14p ANNOT_FONT_SIZE 12p LABEL_FONT_SIZE 12p
grdimage $file.grd -I$name.grad -CELSC.cpt -Ba30mg10m $R -P -Xc -Y1.5i -V -K >! $name.ps
grdcontour $file.grd $R -C.1 -A.5f5to -Z.001 -Wc.1p -Wa.3p -Q50 -O -K >> $name.ps
psxy ELSC_VFR_axis.txt $R -Wthickest,red,solid -P -M -O -K >> $name.ps
psxy ILSC_CLSC.xy $R -Wthickest,red,solid -P -M -O -K >> $name.ps
psxy ~/Lau/KM0804/SS/NELSCvents.xy $R -Gred -P -Sa.3i -O -K >> $name.ps
psxy ~/Lau/KM0804/SS/VFRvents.xy $R -Gred -P -Sa.3i -O -K >> $name.ps
psscale -CELSC.cpt -D1.5i/-.6i/3i/.1ih -Ba1000f200/:"Depth (m)": -O -K >> $name.ps
pscoast $R -Df -Gblack -P -O -K >> $name.ps
psbasemap $R -Lfx5i/-.6i/-21/50:km:r -O >> $name.ps
ps2pdf $name.ps >! $name.pdf

# Entire Lau basin
set name = "Lau_bathymetry_01_11"
set R = "-R180/188/-25/-14 -JM6i"
gmtset HEADER_FONT_SIZE 20p ANNOT_FONT_SIZE 12p LABEL_FONT_SIZE 12p
gmtset PAPER_MEDIA Custom_8ix11i
grdgradient $name.grd -G$name.grad -A100 -Nt1 -V
grdimage $name.grd -I$name.grad -CELSC.cpt -JM6i -P -Xc -Y1.5i -Ba2dg1d -V -K >! $name.ps
psscale -CELSC.cpt -D1.5i/-.6i/3i/.1ih -Ba1000f200/:"Depth (m)": -O -K >> $name.ps
psbasemap $R -Lfx5i/-.6i/-20/200:km:r -O -K >> $name.ps
pscoast $R -Df -Gblack -P -O -K >> $name.ps
psxy ~/Lau/KM0804/SS/neovolcanic.xyz $R -Wthicker,red,solid -P -M -O >> $name.ps
ps2pdf $name.ps >! $name.pdf
```

```
### TRACK PLOT WITH ALL CRUISES USED IN THE STUDY ###
set name = "all_cruise_tracks"
set R = "-JM6i -R-177/-175/-23:00/-19:00 -JM6i"
gmtset PAPER_MEDIA Custom_8ix15i
gmtset HEADER_FONT_SIZE 14p ANNOT_FONT_SIZE 12p LABEL_FONT_SIZE 12p
gmttrack mgl0903 $R -Ma5000ht5000h -V -K -P -W1p,blue,solid >! $name.ps
psbasemap -Lfx3i/-.5i/-21/100:km:r $R -P -O -K >> $name.ps
pscoast $R -Df -G0 -Ba30mg10m:."Ship Tracks from all Cruises": -O -P -V -K >> $name.ps
psxy km0410_track.txt $R -W1p,green,solid -P -O -K >> $name.ps
psxy km0417_track.txt $R -W1p,magenta,solid -P -O -K >> $name.ps
psxy hm9507_track.txt $R -W1p,orange,solid -P -O -K >> $name.ps
gmttrack km0804 $R -Ma5000ht5000h -V -K -O -P -W1p,black,solid >> $name.ps
psxy ELSC_VFR_axis.txt $R -W1p,red,solid -P -M -O -K >> $name.ps
psxy ILSC_CLSC.xy $R -W1p,red,solid -P -M -O >> $name.ps
ps2pdf $name.ps >! $name.pdf
```

REFERENCES

Austin, R., F. Martinez, R. Dunn, and B. Taylor (2009), Geophysical mapping in the western Lau basin reveals possible early seafloor spreading, arc volcanism, and remnant rifted arc crust, *Eos Trans. AGU, 90(50),* Fall Meet. Suppl., Abstract OS13A-1159

Baker, E.T., J.A. Resing, S.L. Walker, F. Martinez, B. Taylor, and K. Nakamura (2006), Abundant hydrothermal venting along melt-rich and melt-free ridge segments in the Lau backarc basin, *Geophys. Res. Lett.*, 33(7), doi: 10.1029/2005 GL025283.

Baker, E.T., F. Martinez, J.A. Resing, S.L. Walker, N.J. Buck, and M.H. Edwards (2010) Hydrothermal cooling along the Eastern Lau Spreading Center: No evidence for discharge beyond the neo-volcanic zone, *Geochem. Geophys. Geosyst.,11(8), Q08004.*

Carbotte, S.M., R. Arko, D.N. Chayes, W. Haxby, K. Lehnert, S. O'Hara, W.B.F. Ryan, R.A. Weissel, T. Shipley, L. Gahagan, K. Johnson, T. Shank (2004), New Integrated Data Management System for Ridge2000 and MARGINS Research, *Eos Trans. AGU*, 85(51), 553, doi:10.1029/2004EO510002.

Chadwick, W.W., R.W. Embley, P.D. Johnson, S.G. Merle, S. Ristau, and A. Bobbitt (2005), The submarine flanks of Anatahan Volcano, commonwealth of the Northern Mariana Islands, *J. Volcanol. Geotherm. Res., 146,* pp. 8-25.

Dunn, R. (2009), Crustal Accretion and Mantle Processes Along the Subduction-Influenced Eastern Lau Spreading Center: Project: L-SCAN (Lau Spreading Center Active-Source Investigation), Cruise Report MGL0903, University of Hawaii, Honolulu, HI.

Dunn, R., and F. Martinez (2011), Contrasting crustal production and rapid mantle transitions beneath backarc ridges, *Nature, 469,* pp. 198-202, doi:10.1038/nature09690.

Escrig, S., A. Bezos, S. L. Goldstein, C. H. Langmuir, and P. J. Michael (2009), Mantle source variations beneath the Eastern Lau Spreading Center and the nature of subduction components in the Lau basin Tonga arc system, *Geochem. Geophys. Geosyst., 10*, doi: 10.1029/2008GC002281. (KM0417 CRUISE)

Ferrini, V.L., M.K. Tivey, S.M. Carbotte, F. Martinez, C. Roman (2008), Variable morphologic expression of volcanic, tectonic, and hydrothermal processes at six hydrothermal vent fields in the Lau backarc basin, *Geochem., Geophys., Geosyst.,* 9(7), doi: 10.1029/2008GC002047.

Garfunkel, Z., C. A. Anderson, and G. Schubert (1986), Mantle circulation and the lateral migration of subducted slabs, *J. Geophys. Res*, *91*(B7), 7205-7223.

Gill, J. B. (1976), Composition and age of Lau Basin and Ridge volcanic rocks: Implications for evolution of an interarc basin and remnant arc, *Geol. Soc. Am. Bull.*, *87*(10), p. 1384.

Goodliffe, A.M. (1995), Preliminary Cruise Report Hakurei Maru No. 2, Lau Basin, Leg 1, SOPAC Cruise Report 144, Suva, Fiji, 12 pp. (HM9507 CRUISE)

Harding, A.J., G.M. Kent, and J.A. Collins (2000), Initial results from a multichannel seismic survey of the Lau backarc basin, *Eos, Trans. AGU, 81,* abstract T61C-16.

Harmon, N., and D. K. Blackman (2010), Effects of plate boundary geometry and kinematics on mantle melting beneath the backarc spreading centers along the Lau Basin, *Earth Planet. Sci. Lett., doi:10.1016/j.epsl.2010.08.004.*

Hirth, G. and D.L. Kohlstedt (2003) Rheology of the upper mantle and the mantle wedge: A view from the experimentalists, in *Inside the Subduction Factory*, ed. J. Eiler, Geophysical Monograph, American Geophysical Union, Washington, D.C., vol. 138, pp. 83-105.

Jacobs, A.M., A.J. Harding, and G.M. Kent (2007), Axial crustal structure of the Lau backarc basin from velocity modeling of multichannel seismic data, *Earth Planet. Sci. Lett., 259*, pp. 239-255.

Jenner, G.A., P.A. Cawood, M. Rautenschlein, and W.M. White (1987), Composition of backarc basin volcanics, Valu Fa Ridge, Lau basin: Evidence for a slab-derived component in their mantle source, *J. Volcanol. Geotherm. Res., 32, pp. 209-222.*

Karato, S.-I., M. Paterson, and J. Fitzgerald (1986), Rheology of Synthetic Olivine Aggregates: Influence of Grain Size and Water, *J. Geophys. Res., 91,* pp. 8151-8176.

Karig, D.E. (1970), Ridges and Basins of the Tonga-Kermadec Island Arc System, *J. Geophys. Res., 75(2),* pp. 239-254.

Lallemand, S., A. Heuret, and D. Boutelier (2005), On the relationships between slab dip, backarc stress, upper plate absolute motion, and crustal nature in subduction, *Geochem., Geophys., Geosyst., 6(9),* doi: 10.1029/2005GC000917

Loock, G. (1992), Character and distribution of the Indian Ocean domain: A study of the mantle source compositions of Lau basin volcanics (SW Pacific) and the Indian Ocean mid-oceanic ridge basalts, Ph.D. thesis, Univ. zu Koln, Cologne, Germany.

Ma, Y., and J.R. Cochran (1996), Transitions in axial morphology along the Southeast Indian Ridge, *J. Geophys. Res., 101,* pp. 15,849-15,866

Ma, L.Y., and J.R. Cochran (1997), Bathymetric roughness of the Southeast Indian Ridge: Implications for crustal accretion at intermediate spreading rate mid-ocean ridges, *J. Geophys. Res., 102,* pp. 17,697-17,711.

Macdonald, K. C. (1982), Mid-ocean ridges: Fine scale tectonic, volcanic and hydrothermal processes within the plate boundary zone, *Annual Review of Earth and Planetary Science*, *10*, 155-190.

Macdonald, K.C. and P.J. Fox (1983), Overlapping spreading centers: new accretion geometry on the East Pacific Rise, *Nature*, *302*, pp. 55-58.

Macdonald, K.C. and P.J. Fox (1990), The mid-ocean ridge, *Scientific American*, 262:72-79.

Macdonald, K.C., D.S. Scheirer, and S.M. Carbotte (1991a), Mid-Ocean Ridges: Discontinuities, Segments, and Giant Cracks, *Science*, *v. 253*, pp. 986-994.

Macdonald, K.C., P.J. Fox, R.T. Alexander, R. Pockalny, and P. Gente (1996), Volcanic growth faults and the origin of Pacific abyssal hills, *Nature*, *380*, pp. 125-129.

Marsh, B.D. (1979), Island-arc volcanism, *Am. Sci., 67,* pp. 161-172.

Martinez, F., and B. Taylor (2002), Mantle wedge control on backarc crustal accretion, *Nature*, *416,* pp. 417-420.

Martinez, F., and B. Taylor (2003), Controls on backarc crustal accretion: insights from the Lau, Manus, and Mariana basins in: R.D. Larter, P.T. Leat (Eds.), *Intra-Oceanic Subduction Systems: Tectonic and Magmatic Processes*, Special Publications, Geological Society, London, vol. 219, pp. 19-54.

Martinez, F., and B. Taylor (2006), Modes of Crustal Accretion in Back arc Basins: Inferences from the Lau Basin, in *Back arc Spreading Systems:*

Geological, Biological, Chemical, and Physical Interactions, American Geophysical Union, pp. 5-30. (KM0410 CRUISE)

Martinez, F., B. Taylor, E.T. Baker, J.A. Resing, and S.L. Walker (2006), Opposing trends in crustal thickness and spreading rate along the back-arc Eastern Lau Spreading Center: Implications for controls on ridge morphology, faulting, and hydrothermal activity, *Earth Planet. Sci. Lett., 245,* pp. 655-672*.*

Martinez, F., E. T. Baker, J. A. Resing, M. H. Edwards, S. L. Walker, and N. Buck (2008), Distribution of Hydrothermal Activity at the Lau ISS: Possible Controlling Parameters, in *AGU Fall Meeting*, edited, American Geophysical Union, San Francisco, CA. (KM0804 CRUISE)

Millen, D.W., and M. W. Hamburger (1998), Seismological evidence for tearing of the Pacific plate at the northern termination of the Tonga subduction zone, *Geology*, *26*(7), pp. 659-662.

Nautilus Minerals, Inc. (2009), Exploration success continues for Nautilus Minerals in Tonga, News Release Number 2009-03, http://www.nautilusminerals.com/s/ Media-NewsReleases.asp? ReportID=338585.

Parson, L.M., J.A Pearce, B.J. Murton, and R.A. Hodkinson (1990), Role of ridge jumps and ridge propagation in the tectonic evolution of the Lau back arc basin, south- west Pacific, *Geology*, *18*, pp. 470-473.

Parson, L.M., and J.W. Hawkins (1994) Two-stage propagation and the geological history of the Lau backarc basin, in *Proceedings of the Ocean Drilling Program, Scientific Results*, edited by J. W. Hawkins, L. M. Parson and J. F. Allan, pp. 819-828.

Pearce, J.A., M. Ernewein, S.H. Bloomer, L.M. Parson, B.J. Murton, and L.E. Johnson (1994), Geochemistry of Lau basin volcanic rocks: Influence of

ridge segmentation and arc proximity, *Geol. Soc. Spec. Publ., 81,* pp. 53-75. doi: 10.1144/GSL.SP.1994.081.01.04

Peate, D.W., Kokfelt, T.F., Hawkesworth, C.J., van Calsteren, P.W., Hergt, J.M., and Pearce, J.A. (2001), U-series isotope data on Lau Basin glasses: The role of subduction-related fluids during melt generation in backarc basins, *Journal of Petrology, vol. 42,* pp. 1449-1470.

Pelletier, B., Y. Lagabrielle, M. Benoit, G. Cabioch, S. Calmant, E. Garel, and C. Guivel (2001), Newly identified segments of the Pacific-Australia plate boundary along the North Fiji transform zone, *Earth Planet. Sci. Lett.*, *193*, 347-358.

Schmidt, M. W., and S. Poli (1998), Experimentally based water budgets for dehydrating slabs and consequences for arc magma generation, *Earth Planet. Sci. Lett., 163*(1-4), pp. 361-379.

Sempere, J.C., and K.C. Macdonald (1986), Overlapping spreading centers: Implications from crack growth simulation by the displacement discontinuity method, *Tectonics, 5(1),* pp. 151-163.

Small, Christopher (1998), Global Systematics of Mid-Ocean Ridge Morphology, *Faulting and Magmatism at Mid-Ocean Ridges*, Geophysical Monograph 106, American Geophysical Union, pp. 1-22.

Smith, W. H. F., and D. T. Sandwell (1997), Global seafloor topography from satellite altimetry and ship depth soundings, *Science*, *277*, p. 1957-1962, 26 Sept., 1997.

Stolper, E., and S. Newman (1994), The role of water in the petrogenesis of Mariana trough magmas, *Earth Planet. Sci. Lett., 121,* pp. 293-325.

Tamura, Y., Y. Tatsumi, D. Zhao, Y. Kido, and H. Shukuno. (2002) Hot fingers in the mantle wedge: new insights into magma genesis in subduction zones, *Earth Planet. Sci. Lett.,197,* pp. 105-116.

Taylor, B., K. Zellmer, F. Martinez, and A. Goodliffe (1996) Sea-floor spreading in the Lau backarc basin, *Earth Planet. Sci Lett., 144,* pp. 35-40.

Taylor, B., et al. (2001), A Proposal for a RIDGE Integrated Studies Site in the Lau Backarc Basin, downloaded from the Ridge 2000 website: http://www.ridge2000.org/science/downloads/lau/Lau_SiteProposal.pdf

Taylor, B., and F. Martinez (2003), Backarc basin basalt systematics, *Earth Planet. Sci. Lett., 210,* pp. 481-497.

Turner, I. M., C. Pierce, and M.C. Sinha (1999), Seismic imaging of the axial region of the Valu Fa Ridge, Lau Basin- the accretionary processes of an intermediate backarc spreading ridge, *Geophys. J. Int., 138,* pp. 495-519.

Vallier, T.L., G.A. Jenner, F.A. Frey, J.B. Gill, A.S. Davis, A.M. Volpe, J.W. Hawkins, J.D. Morris, P.A. Cawood, J.L. Morton, D.W. Scholl, M. Rautenschlein, W.M. White, R.W. Williams, A.J. Stevenson, and L.D. White (1991) Subalkaline andesite from Valu Fa Ridge, a backarc spreading center in southern Lau Basin: petrogenesis, comparative chemistry, and tectonic implications, *Chem. Geol.*, *91*(3), pp. 227-256.

Watanabe, M., K. Okino, and T. Kodera (2010), Rifting to spreading in the southern Lau Basin: Variations within the transition zone, *Tectonophysics, 494*(3-4), pp. 226-234.

Wessel, P., and W. H. F. Smith (1998), New, improved version of Generic Mapping Tools released, *Eos, Trans. AGU*, *79* (47 (November 24)), p. 579.

Wiens, D., G. Wheat, F. Martinez, and C. Langmuir (2005), Status report on the Lau Basin ISS, *Ridge 2000 Events*, 3 (Spring 2005), pp. 11-13.

Wiedicke, M. and J. Collier (1993) Morphology of the Valu Fa Spreading Ridge in the Southern Lau Basin, *J. Geophys Res., 98,* pp. 11,769-11,782.

Wiens, D., F. Martinez, C. Langmuir, M. Tivey, J. Childress, C. Fisher, G. Wheat, M. Perfit, D. Blackman, and S. Kim (2004) The Eastern Lau Basin Integrated Studies Site (ISS): Recent Progress and Future Plans, *Eos Trans. AGU*, *85* (47, Fall Meeting Suppl.), abstract B13A-0187 invited.

Wiens, D., G. Wheat, F. Martinez, and C. Langmuir (2005), Status report on the Lau Basin ISS, *Ridge 2000 Events*, 3 (Spring 2005), pp. 11-13.

Wysoczanski, R.J., E. Todd, I.C. Wright, M.I. Leybourne, J.M. Hergt, C. Adam, K. Mackay (2010) Backarc rifting, constructional volcanism, and nascent disorganized spreading in the southern Havre Trough backarc rifts (SW Pacific), *J. Volcanol. Geotherm. Res., 190,* pp. 39-57.

Zellmer, K.E. and B. Taylor (2001), A three-plate kinematic model for Lau Basin opening, *Geochem., Geophys., Geosyst., 2,* Paper number: 2000GC000106